

# Aeroradiometric Measurements in the Framework of the Swiss Exercise ARM23

Gernot Butterweck, Alberto Stabilini, Benno Bucher, David Breitenmoser,  
Ladislav Rybach, Cristina Poretti, Stéphane Maillard, Adrian Hess,  
Fabian Hauenstein, Ulisse Gendotti, Malgorzata Kasprzak,  
Gerald Scharding, Sabine Mayer

PSI Bericht Nr. 24-02  
March 2024  
ISSN 1019-0643

DOI: <https://doi.org/10.55402/psi:60054>

This work is distributed under the Creative Commons Attribution 4.0 License



# Aeroradiometric Measurements in the Framework of the Swiss Exercise ARM23

Gernot Butterweck<sup>1</sup>, Alberto Stabilini<sup>1</sup>, Benno Bucher<sup>2</sup>, David Breitenmoser<sup>1</sup>,  
Ladislaus Rybach<sup>3</sup>, Cristina Poretti<sup>4</sup>, Stéphane Maillard<sup>5</sup>, Adrian Hess<sup>4</sup>,  
Fabian Hauenstein<sup>6</sup>, Ulisse Gendotti<sup>7</sup>, Malgorzata Kasprzak<sup>1</sup>,  
Gerald Scharding<sup>4</sup>, Sabine Mayer<sup>1</sup>

- 1 Department of Radiation Safety and Security, Logistics Division, Paul Scherrer Institute (PSI),  
Forschungsstrasse 111, 5232 Villigen PSI, Switzerland
- 2 Swiss Federal Nuclear Safety Inspectorate (ENSI),  
Industriestrasse 19, 5201 Brugg, Switzerland
- 3 Institute of Geophysics, Swiss Federal Institute of Technology Zürich (ETHZ),  
8092 Zürich, Switzerland
- 4 Swiss National Emergency Operations Center (NEOC),  
3003 Bern, Switzerland
- 5 NBC-EOD Centre of Competence (Nuclear Biological Chemical Defense and Explosive Ordnance Disposal),  
3700 Spiez, Switzerland
- 6 Spiez Laboratory, Austrasse,  
3700 Spiez, Switzerland
- 7 Arktis Radiation Detectors, Räffelstrasse 11,  
8045 Zürich, Switzerland

Paul Scherrer Institut (PSI)  
5232 Villigen PSI, Switzerland  
Tel. +41 56 310 21 11  
Fax +41 56 310 21 99  
[www.psi.ch](http://www.psi.ch)

PSI Bericht Nr. 24-02  
March 2024  
ISSN 1019-0643



## Abstract

The flights of the civil (ARM23c) and military (ARM23m) parts of the exercise were performed between June 19<sup>th</sup> and 23<sup>rd</sup> and between September 11<sup>th</sup> and September 15<sup>th</sup>, respectively. The measuring system RLL001 was employed for all measurements.

As usual, during the civil exercise the environs of some of the Swiss nuclear power plants were screened, on behalf of the Swiss Nuclear Safety Inspectorate (ENSI). At the site of the nuclear power plant Gösgen (KKG) with its pressurized water reactor, the activation products of the primary coolant loop are kept in the well shielded reactor building, thus generating no elevated readings neither on the premises nor in the vicinity of the power plant. The nuclear power plant of Mühleberg (KKM) is now being decommissioned. During this phase, activated components are temporarily stored and processed on the plant premises. The dose rate produced by these components, easily detected and identified with the Swiss airborne gamma spectrometry system, is nevertheless very modest and closely monitored by the Swiss Nuclear Safety Inspectorate (ENSI).

Search exercises for radionuclide sources were performed in both parts of ARM23. The operational software of the RLL systems was able to detect the radionuclide sources placed in military training areas. The Man-Made Gross-Count (MMGC) ratio demonstrated a good sensitivity for the identification of radionuclide sources. Nevertheless, a weak radionuclide source placed in the field of view of the helicopter (300 m x 300 m at a ground clearance of 100 m) together with a much stronger radionuclide source emitting higher energy photons was obscured due to Compton scattered photons and therefore could not be detected. Measurements of two teams using drones equipped with radiation monitors demonstrated that low flying drones (ground clearance below 10 m) can be a valuable and complementary tool to identify sources and to further reduce the target area to be searched with ground teams.

An altitude profile over Lake Constance confirmed the already observed influence of airborne radon progeny on the determination of cosmic and background corrections.

Background flights were performed over several Swiss regions. Besides attenuation effects of water bodies, variations of natural radionuclide content could be observed. A new flight strategy in alpine topography was tested near the Swiss mountain Chrüz. Following contour lines of the topography reduces the necessity for drastic flight altitude changes compared to the parallel line pattern normally used, but is much more challenging for the pilots.

# Contents

<b>1</b>	<b>Introduction</b>	<b>1</b>
1.1	Measuring system RLL . . . . .	2
1.2	Measuring flights . . . . .	4
1.3	Data evaluation . . . . .	4
1.3.1	Background and cosmic correction . . . . .	4
1.4	Data presentation . . . . .	6
<b>2</b>	<b>Results of the exercise ARM23</b>	<b>9</b>
2.1	Source search exercises . . . . .	12
2.1.1	Wangen an der Aare . . . . .	12
2.1.2	Spiez . . . . .	21
2.2	Recurrent measurements over Swiss nuclear installations . . . . .	26
2.2.1	KKG . . . . .	26
2.2.2	KKM . . . . .	29
2.3	Background measurements over Swiss cities and regions . . . . .	33
2.3.1	Bercher . . . . .	33
2.3.2	Chrüz . . . . .	42
2.3.3	Estavayer-le-Lac . . . . .	48
2.3.4	Klosters . . . . .	51
2.3.5	Landquart . . . . .	54
2.3.6	Monthey . . . . .	58
2.3.7	Noréaz . . . . .	61
2.3.8	Rapperswil . . . . .	64
<b>3</b>	<b>Conclusions</b>	<b>67</b>
<b>4</b>	<b>Literature</b>	<b>67</b>
<b>5</b>	<b>Previous reports</b>	<b>68</b>
<b>6</b>	<b>Evaluation parameters</b>	<b>72</b>
6.1	Detector RLL001 . . . . .	72

## List of Figures

1	Components of the RLL system . . . . .	2
2	Operator console of the RLL system . . . . .	3
3	RLL detector mounted in the cargo bay of a Super Puma helicopter . . . . .	3
4	Low energy count rate over Lake Constance . . . . .	6
5	Overview of the measurement areas of ARM23. . . . .	11
6	Screenshot of the Mirion software during source search . . . . .	13
7	Dose rate over the source search area . . . . .	13
8	MMGC-ratio over the source search area . . . . .	14
9	MMGC-ratio map of the Mirion software during source search . . . . .	14
10	Gamma ray spectrum measured over the exercise area with the helicopter . . . . .	15
11	Drones used in the source search . . . . .	16
12	Dose rate over the source search area . . . . .	17
13	Total count rate over the source search area . . . . .	17
14	Dose rate over the potential source locations . . . . .	18
15	Dose rate over the potential source locations . . . . .	18
16	Gamma ray spectrum measured over the $^{137}\text{Cs}$ source with Spiez drone . . . . .	19
17	Gamma ray spectrum measured over the $^{137}\text{Cs}$ source with Arktis drone . . . . .	19
18	Gamma ray spectrum measured over the $^{133}\text{Ba}$ source with Spiez drone . . . . .	20
19	Gamma ray spectrum measured over the $^{133}\text{Ba}$ source with Arktis drone . . . . .	20
20	Dose rate of the source search exercise near Spiez . . . . .	22
21	MMGC-ratio of the source search exercise near Spiez . . . . .	23
22	MMGC-ratio of the source search exercise near Spiez . . . . .	24
23	Exposure location of the source search exercise near Spiez . . . . .	24
24	Picture of the exposure location of the source search exercise near Spiez . . . . .	25
25	Gamma ray spectrum measured over the source location . . . . .	25
26	Dose rate in the vicinity and to the south of KKG . . . . .	26
27	MMGC-ratio in the vicinity and to the south of KKG . . . . .	27
28	$^{232}\text{Th}$ activity concentration in the vicinity and to the south of KKG . . . . .	28
29	Photon spectrum over KKM premises compared to background . . . . .	29
30	Dose rate in the vicinity of KKM . . . . .	30
31	MMGC-ratio in the vicinity of KKM . . . . .	31
32	$^{232}\text{Th}$ activity concentration in the vicinity of KKM . . . . .	32
33	Photon spectra near Bercher . . . . .	34
34	Dose rate near Bercher . . . . .	35
35	MMGC-ratio near Bercher . . . . .	36
36	$^{232}\text{Th}$ activity concentration near Bercher . . . . .	37
37	Terrestrial dose rate near Bercher measured on September 11 <sup>th</sup> . . . . .	38
38	Terrestrial dose rate near Bercher measured on September 13 <sup>th</sup> . . . . .	39
39	$^{238}\text{U}$ activity concentration near Bercher measured on September 11 <sup>th</sup> . . . . .	40
40	$^{238}\text{U}$ activity concentration near Bercher measured on September 13 <sup>th</sup> . . . . .	41
41	Color scale altitude map superposed over a relief of the Chrüz region . . . . .	42
42	Dose rate near the Chrüz . . . . .	43
43	Terrestrial dose rate near the Chrüz . . . . .	44
44	MMGC-ratio near the Chrüz . . . . .	45
45	$^{232}\text{Th}$ activity concentration near the Chrüz . . . . .	46
46	$^{40}\text{K}$ activity concentration near the Chrüz . . . . .	47
47	Dose rate near Estavayer-le-Lac . . . . .	48

48	MMGC-ratio near Estavayer-le-Lac . . . . .	49
49	<sup>232</sup> Th activity concentration near Estavayer-le-Lac . . . . .	50
50	Dose rate near Klosters . . . . .	51
51	MMGC-ratio near Klosters . . . . .	52
52	<sup>232</sup> Th activity concentration near Klosters . . . . .	53
53	Dose rate near Landquart . . . . .	55
54	MMGC-ratio near Landquart . . . . .	56
55	<sup>232</sup> Th activity concentration near Landquart . . . . .	57
56	Dose rate near Monthey . . . . .	58
57	MMGC-ratio near Monthey . . . . .	59
58	<sup>232</sup> Th activity concentration near Monthey . . . . .	60
59	Dose rate near Noréaz . . . . .	61
60	MMGC-ratio near Noréaz . . . . .	62
61	<sup>232</sup> Th activity concentration near Noréaz . . . . .	63
62	Dose rate near Rapperswil . . . . .	64
63	MMGC-ratio near Rapperswil . . . . .	65
64	<sup>232</sup> Th activity concentration near Rapperswil . . . . .	66

# List of Tables

1	Determination of the slope for cosmic correction . . . . .	5
2	Determination of the background count rate . . . . .	5
3	Quantification of the colour scale . . . . .	8
4	Flight data of ARM23 . . . . .	10
5	Results of the source search . . . . .	16

# 1 Introduction

Swiss airborne gamma-ray spectrometry measurements started in 1986. The methodology and software for calibration, data acquisition and mapping were developed at the Institute of Geophysics of the Swiss Federal Institute of Technology Zurich (ETHZ). Between 1989 and 1993 the environs of Swiss nuclear installations were measured annually on behalf of the Swiss Federal Nuclear Safety Inspectorate (ENSI) during exercises performed as system check and drill for the operators. This schedule was changed to biennial inspections in 1994, together with an organizational inclusion of the airborne gamma-spectrometric system (ARM) into the Emergency Organization Radioactivity (EOR) of the Federal Office for Civil Protection (FOCP). The deployment of the airborne gamma-spectrometric system is organized by the National Emergency Operations Centre (NEOC). NEOC is also responsible for the recruitment and instruction of the measurement team and for the operational readiness of the system. Aerial operations are coordinated and performed by the Swiss Air Force with Super Puma helicopters. Identical gamma-spectrometric pieces of equipment are stationed at the military airfields of Dübendorf and Payerne and can be fully operative and airborne within four hours. Responsibility for scientific support, development and maintenance of the aeroradiometric measurement equipment passed from ETHZ to the Radiation Metrology Section of the Paul Scherrer Institute (PSI) in 2003, in cooperation with ENSI. General scientific coordination and planning of the annual measuring flights is provided by the Expert Group for Aeroradiometrics (FAR) which consists of experts from all Swiss institutions concerned with aeroradiometry. FAR, formerly a working group of the Swiss Federal Commission for NBC protection (ComNBC), was re-organized as an expert group of NEOC in 2008. Additional information can be found at <https://far.ensi.ch/>. In 2018, the ARM measuring system used by NEOC in past exercises was replaced with the RLL (Radiometrie Land-Luft) system owned by the Swiss armed forces. The maintenance of the RLL systems is performed by the manufacturer according to a service agreement with the Swiss armed forces. Of the four systems available, under normal circumstances two systems are operated by the staff of the NBC-EOD Centre of Competence (NBC-EOD) for measurement tasks with military character and two systems are assigned to NEOC for the deployment in case of civil emergencies with a radiological component. Since 2018, the scientific report includes, in addition to the measuring flights of NEOC (ARM23c), flights performed by NBC-EOD (ARM23m).

This report focuses on methodological aspects and thus complements the respective short reports available at [vtg.admin.ch/de/gruppe-verteidigung/organisation/kdo-ausb/lvb-g-rttg-abc/komp-zen-abc-kamir.html](http://vtg.admin.ch/de/gruppe-verteidigung/organisation/kdo-ausb/lvb-g-rttg-abc/komp-zen-abc-kamir.html) for ARM23m and <https://www.naz.ch> for ARM23c.



## 1.1 Measuring system RLL

The measuring system RLL (Radiometrie Land-Luft) used both for civil and military measurements consists of a radiation detector featuring four NaI(Tl) scintillation crystals having a total volume of 16.8 litres with their associated photo-multipliers and multichannel analysers (MCA) for low level measurements, and one Geiger-Müller tube and associated electronics for high dose-rate measurements. The spectroscopic measuring chain provides a linear energy calibration of the MCA up to 3 MeV divided into 1024 channels. NaI detectors, Geiger-Müller tube and associated electronics are installed in an aluminium case with thermal insulation foam. The detection container is mounted in the cargo bay below the centre of the helicopter. The RLL system uses position, air pressure, air temperature and radar altitude data provided by the helicopter via the internal ARINC bus. Figure 1 shows the complete system packaged for storage. The equipment control, data acquisition and storage are performed with a rugged computer working as a data server. Two further rugged redundant client computers are used as operator interface for real-time evaluation, data mapping and communication. All computers are installed in an equipment rack, including an additional battery as power supply back-up. Both operators can operate the system with their associated client computer, display, keyboard and trackball. The additional third central display of the operator's console is mirrored on a screen in the cockpit located between both pilots and is used for information exchange with the pilots and general radiological situation awareness (Figure 2). The measuring system RLL is mounted in an Aerospatiale AS 332 Super Puma helicopter (TH 06) of the Swiss Air Forces (Figure 3). This helicopter has excellent navigation properties and allows emergency operations during bad weather conditions and night time.



Figure 1: Components of the RLL system. 1. Lifting platform for the installation of the detection container. 2. Floor plates and accessories case. 3. Monitors and operator console. 4. Detection container. 5. Operator seats and equipment rack.

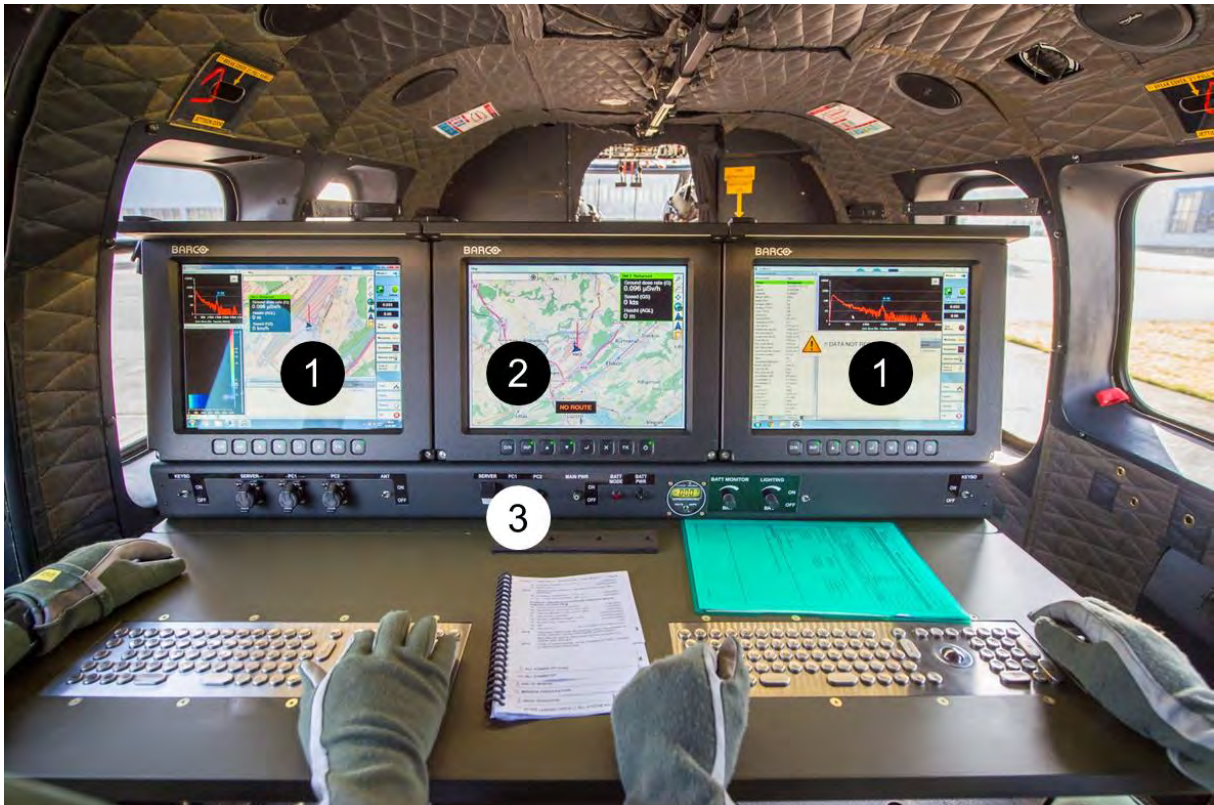


Figure 2: Operator console of the RLL system. 1. Displays of the client computers. 2. Common display (mirrored in the cockpit). 3. Control panel with switches for power, lighting and communication and USB ports for file exchange.

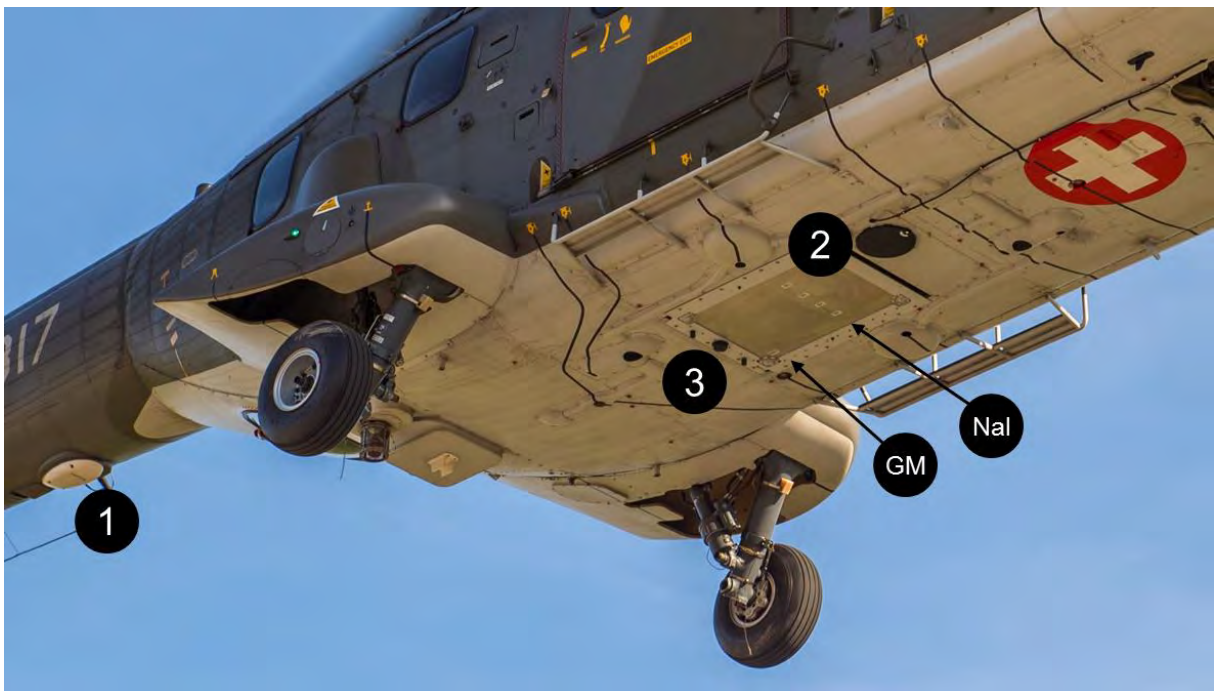


Figure 3: RLL detector mounted in the cargo bay of a Super Puma helicopter. 1. Radar altimeter. 2. Detection container marked with detector reference points. 3. UMTS antenna for data upload.

## 1.2 Measuring flights

The advantage of aeroradiometric measurements lies in the high velocity of measurements in a large area, even over rough terrain. Uniform radiological information of an area is obtained from a regular grid of measuring points. This grid is composed from parallel flight lines, 250 m apart in the standard case. The flight altitude above ground is aspired to be constant during the measuring flight, with typical values lying between 50 m and 150 m above ground. Line spacing and altitude can be adjusted depending on the scope of the measurements: larger line spacing and higher altitude can be adopted for wider area screenings (though increasing the detection limits), whereas a thicker line spacing pattern at reduced altitudes is adopted for confirmation flights or to increase the location accuracy of confined sources of radiation. The spectra are recorded in regular time intervals of typically one second, yielding an integration over 28 m of the flight line considering a speed of 100 km/h.

## 1.3 Data evaluation

The proprietary software for data acquisition and evaluation provided by the manufacturer of the RLL system was tested sufficient for supplying data to support decisions in radiological emergencies. An outline of the algorithms used can be found in Butterweck et al. (2018). An additional independent off-line data evaluation software (named AGS\_CH) following the methodology developed at ETHZ described in Schwarz (1991) and Bucher (2001) is used to produce the results presented throughout the PSI reports since 2020. The measured spectra are evaluated using energy windows for relevant radionuclides and the spectrum dose index (SDI) to determine dose rates.

### 1.3.1 Background and cosmic correction

The civil part of the exercise (ARM23c) included an altitude profile over Lake Constance. The slopes of the Deming regression (Butterweck et al.,2021) are lower compared to the seven altitude profiles used to calculate an average slope for cosmic correction (Table 1). As already observed in 2022 over Lake Neuchâtel (Butterweck et al.,2022), the low values can be attributed to the interference of airborne radon progeny. The count rate in the low energy window deviates clearly from the expected exponential increase with altitude (Figure 4). The results from Lake Constance do not include negative values, which led to the exclusion of the values over Lake Neuchâtel in 2022 in the calculation of an average slope for cosmic correction. Table 1 shows the average slope calculated from eight altitude profiles, including the values of Lake Constance. With the revised average slope, new intercepts of the linear model for cosmic correction can be calculated, representing the constant background of the measuring system. Table 2 shows the revised backgrounds based on the average slopes listed in Table 1. Being the estimated cosmic background the result of a process including averaging procedures, negative values may occur, when values are particularly close to zero.

The background and slope used for the data evaluation of the current exercise are stored under identifiers ISWB\_winname and ISWC\_winname in the header section of all ERS 2.0 files (Section 6) generated for ARM23 data evaluation.

Energy Window	Slope of cosmic correction [ ]						
	Total	Potassium	Uranium	Thorium	Caesium	Cobalt	SDI
Lake Constance 2023c	4.11	0.23	0.13	0.30	0.17	0.36	3.15
Lake Geneva 2018c	5.20	0.28	0.21	0.29	0.45	0.60	3.96
Lake Neuchâtel 2019c	5.48	0.31	0.23	0.26	0.60	0.66	4.09
Lake Neuchâtel 2021c	5.68	0.33	0.23	0.29	0.57	0.72	4.28
Lake Neuchâtel 2021m	6.32	0.35	0.27	0.30	0.75	0.76	4.70
Lake Thun A 2022c	6.32	0.48	0.30	0.33	0.91	1.09	4.66
Lake Thun B 2022c	7.17	0.41	0.32	0.31	0.92	0.80	5.21
Lake Zug 2017c	5.96	0.31	0.25	0.29	0.69	0.70	4.51
Average	5.78	0.34	0.24	0.30	0.63	0.71	4.32
Standard deviation	0.91	0.08	0.06	0.02	0.25	0.21	0.62

Table 1: Determination of the average slope for cosmic correction from seven altitude profiles with sufficient altitude range.

Energy Window	Background count rate [cps]						
	Total	Potassium	Uranium	Thorium	Caesium	Cobalt	SDI
Lake Constance 2023c	124	8	6	0.3	20	12	85
Lake Geneva 2018c	147	10	7	0.3	23	15	101
Lake Neuchâtel 2016c	129	7	6	1.2	21	10	88
Lake Neuchâtel 2019c	104	8	5	-1.0	16	10	70
Lake Neuchâtel 2021c	121	8	5	0.0	18	11	84
Lake Neuchâtel 2021m	145	9	7	0.4	23	14	98
Lake Neuchâtel 2022m	111	7	6	-0.8	19	10	74
North Sea 2018c	34	4	0	-0.1	5	1	22
Lake Thun A 2020c	73	6	3	-0.4	11	6	48
Lake Thun B 2020c	73	5	3	-0.4	11	6	48
Lake Thun A 2022c	134	9	6	-0.1	22	13	91
Lake Thun B 2022c	157	9	8	0.6	25	15	109
Lake Zug 2017c	56	5	2	-0.2	8	3	38

Table 2: Determination of the background count rate using the average slope of cosmic stripping from Table 1.

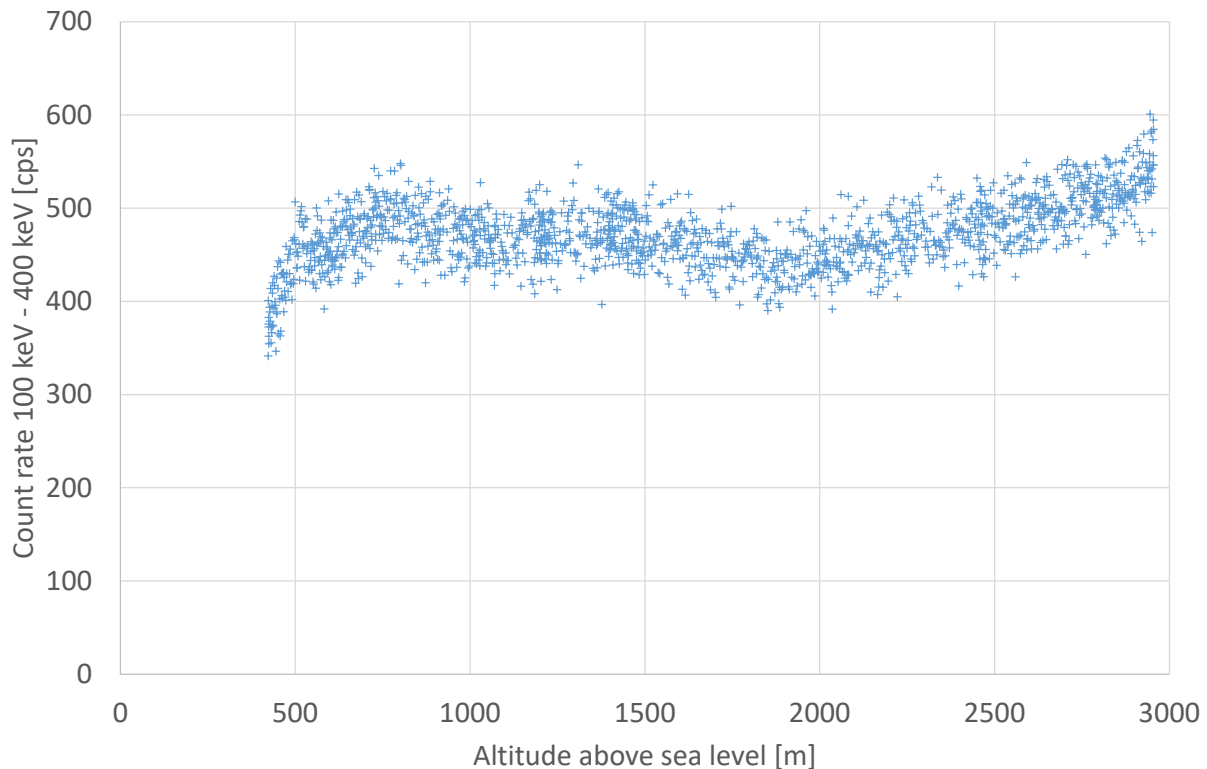


Figure 4: Low energy count rate over Lake Constance in dependence on flight altitude.

## 1.4 Data presentation

Brief reports of the measurement results are compiled by the respective measurement teams and published immediately after the end of the exercise on the homepage of NEOC and the homepage of NBC-EOD Centre of Competence. These reports are archived at <https://far.ensi.ch> under Publications (each year as Short Reports - NEOC). A combined detailed analysis of both parts of the exercise is published in the form of a PSI-report within the responsibility of the FAR. These reports are archived at <https://far.ensi.ch> (as Scientific Reports) and at Paul Scherrer Institute Digital Object Repository (DORA PSI) <https://www.dora.lib4ri.ch/psi>.

For all measuring areas, a map of the total dose rate (ambient dose equivalent rate  $dH^*(10)/dt$  extrapolated to 1 m above ground) and the flight lines is presented together with a map of the Man-Made-Gross-Count (MMGC) ratio. The MMGC-ratio is the quotient between the count rate summed over the energy window (MMGC1) between 400 keV and 1400 keV and the count rate summed over the energy window between 1400 keV and 3000 keV (MMGC2). As most anthropogenic radionuclides emit photons below 1400 keV, the ratio will rise due to these additional photons, whereas natural radionuclides are registered in both energy windows, keeping the ratio relatively constant. Unusual low counts in the MMGC2 energy window due to limited counting statistics can also lead to increased MMGC-ratios. A map of the  $^{232}\text{Th}$  activity concentration (measuring quantity activity per wet mass) provides information on the quality of the measurements, as it can be expected that this quantity is constant over time. As an additional quality measure, an appendix with the basic parameters of the data evaluation is added to simplify a re-evaluation of the data in the future. If the dose rate or the MMGC-ratio indicates elevated values, maps of individual radionuclides (like e.g.  $^{40}\text{K}$  or  $^{137}\text{Cs}$  activity concentrations) are added based on the average photon spectrum over the affected area. In the case of large changes of topography in the

measured area, a map of the terrestrial dose rate consisting of the total dose rate reduced by the altitude dependent cosmic component is included. In the case of measuring flights with the main purpose of mapping natural radionuclide concentrations, a supplementary map of the  $^{40}\text{K}$  activity concentration (measuring quantity activity per wet mass) may also be presented.  $^{238}\text{U}$  concentration maps are usually not presented, as they are affected by the variable concentration of radon and its progeny in the atmosphere at the time of measurement. This year, the region described in section 2.3.1 was overflown in both dry and rainy weather, and extracts of  $^{238}\text{U}$  concentration maps are exceptionally presented to compare the influence of the weather on  $^{238}\text{U}$  measurements.

A discrete colour scale was defined by the Swiss Expert Group for Aeroradiometrics (FAR) in 2019. The colours and their representation as red, green and blue (RGB) values are listed in Table 3 together with the represented ranges of measured values. The unit of ambient dose-equivalent rates used in previous reports, [nSv/h], was changed with the new representation to [ $\mu\text{Sv/h}$ ], the unit used to store ambient dose-equivalent rate values in the ERS 2.0 format (Butterweck et al. (2018)).













Colour	Red	Green	Blue	Dose rate [ $\mu\text{Sv/h}$ ]	MMGC-ratio [ ]	Activity per mass $^{40}\text{K}$	Activity per mass [Bq/kg] $^{238}\text{U}$ , $^{232}\text{Th}$ , $^{137}\text{Cs}$	Activity per area [kBq/m <sup>2</sup> ] $^{137}\text{Cs}$ ( $\beta=9.5 \text{ g/cm}^2$ )
	153	0	153	> 10	> 100	> 10000	> 5000	> 1000
	204	0	102	5 - 10	50 - 100	5000 - 10000	1000 - 5000	200 - 1000
	204	0	0	2 - 5	15 - 50	2000 - 5000	500 - 1000	100 - 200
	255	0	0	0.5 - 2	9 - 15	1500 - 2000	250 - 500	50 - 100
	255	176	51	0.3 - 0.5	8 - 9	1000 - 1500	200 - 250	40 - 50
	255	235	51	0.2 - 0.3	7 - 8	800 - 1000	150 - 200	30 - 40
	230	255	128	0.15 - 0.2	unused	600 - 800	100 - 150	20 - 30
	173	255	153	0.1 - 0.15	unused	400 - 600	75 - 100	15 - 20
	073	255	106	0.08 - 0.1	6 - 7	200 - 400	50 - 75	10 - 15
	102	255	255	0.06 - 0.08	5 - 6	100 - 200	25 - 50	5 - 10
	77	148	255	0.04 - 0.06	unused	50 - 100	12.5 - 25	2.5 - 5
	51	102	179	< 0.04	< 5	< 50	< 12.5	< 2.5

Table 3: Quantification of the colour scale.

## **2 Results of the exercise ARM23**

The flights of the civil (ARM23c) and military (ARM23m) parts of the exercise were performed between June 19<sup>th</sup> and 23<sup>rd</sup> and between September 11<sup>th</sup> and September 15<sup>th</sup>, respectively.

Flight velocity of the Super Puma helicopters of the Swiss Air Force was around 30 m/s with a target ground clearance of 90 m for all measuring flights. The sampling interval of the spectra was one second. Both parts of ARM23 used the detector system RLL001. The evaluation parameters used for this system are listed in section 6.

Personnel of the military units Stab BR NAZ and NBC-EOD Centre of Competence performed the measurements supported by experts from ENSI, PSI, ETHZ, NBC-EOD Centre of Competence and NEOC.

Flight parameters of the measuring flights are listed in Table 4 and an overview of the according flight lines is shown in Figure 5.



Location	Flight identification	Measuring time [s]	Length of run [km]	Area [km <sup>2</sup> ]
Altitude profile				
Lake Constance	Heli 1_20230620 1246	1654		
Search for radionuclide sources				
Wangen an der Aare	Heli 1_20230620 0928	2076	78	1.6
	Heli 1_20230620 1206	317	11	0.1
Spiez	Heli 1_20230913 0910	2104	87	1.4
Recurrent measuring areas over nuclear installations				
KKG	Heli 1_20230622 0845	8131	363	88
Region south of KKG	Heli 1_20230621 0850	18855	953	872
	Heli 1_20230621 0905			
	Heli 1_20230621 goesgen 2			
	Heli 1_20230622 1115			
KKM	Heli 1_20230619 1311	8434	391	93
Background measurements over cities, towns and regions				
Bercher	Heli 1_20230911 1340	23746	1114	229
	Heli 1_20230913 1015			
	Heli 1_20230913 1325			
	Heli 1_20230914 1330			
Chruez	Heli 1_20230622 chruez	2542	94	43
Estavayer-le-Lac	Heli 1_20230914 1440	3811	167	163
Klosters	Heli 1_20230622 klosters	675	27	6
Landquart	Heli 1_20230622 1526	2449	121	29
Monthey	Heli 1_20230914 0900	8861	347	163
Noréaz	Heli 1_20230914 1600	19823	849	163
	Heli 1_20230915 0900			
	Heli 1_20230915 1345			
	Heli 1_20230915 1445			
Rapperswil	Heli 1_20230619 0950	4667	198	47

Table 4: Flight data of ARM23.

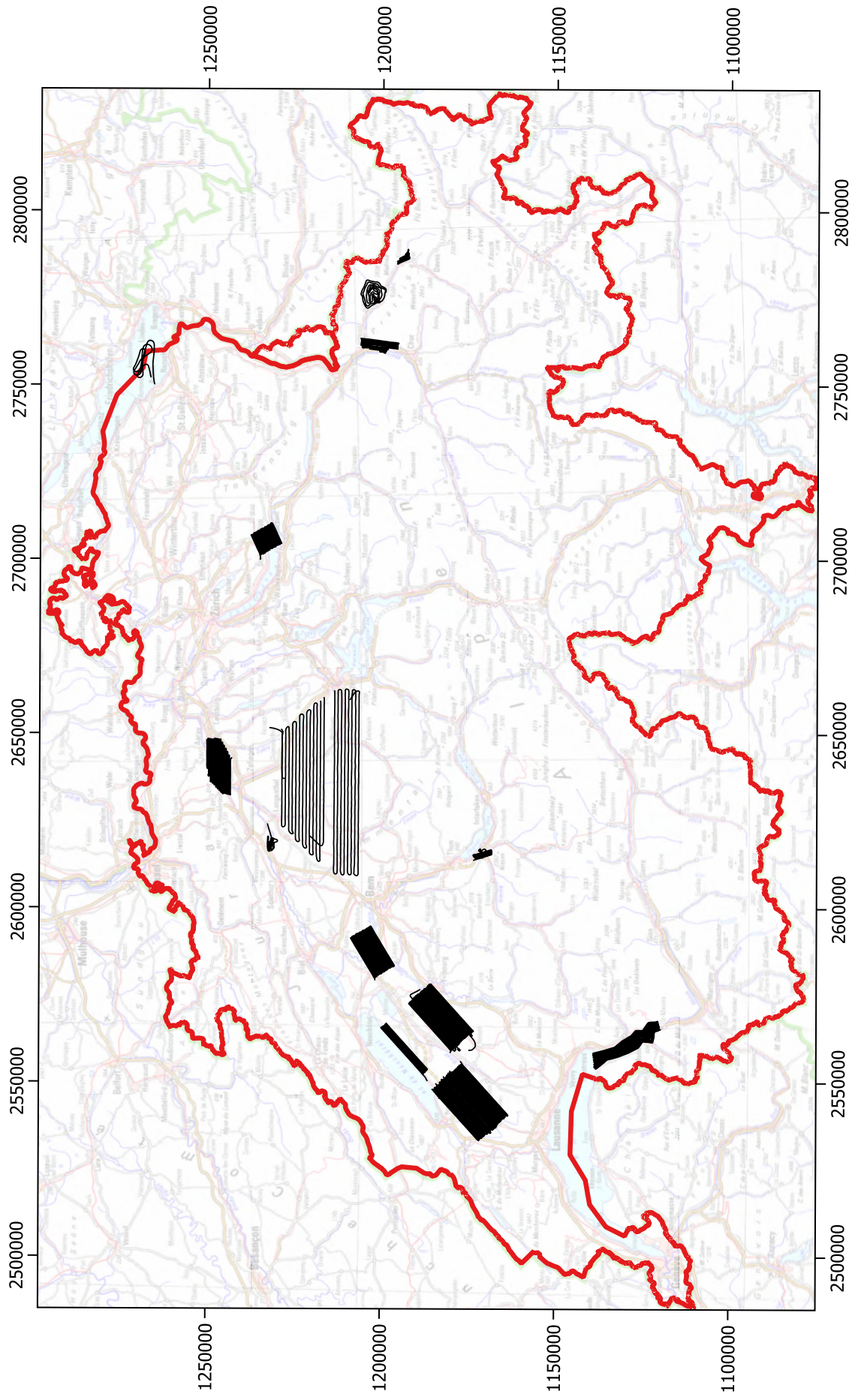


Figure 5: Overview of the measurement areas of ARM23. Geodaten©swisstopo.

## 2.1 Source search exercises

A main scenario for the deployment of Airborne Gamma-Ray Spectrometry (AGRS) systems is the location of lost, stolen or illegally transported radionuclide sources. Both parts of the ARM23 exercise included a search training for radionuclide sources.

### 2.1.1 Wangen an der Aare

A search for radionuclide sources was practised during ARM23c with radionuclide sources placed in a military training area with restricted access located near Wangen an der Aare. The source search exercise was designed to test and train NEOC's procedures and the coordination with partner organisations. The exercise scenario was based on a theft of radionuclide sources. In such an event, three subsequent and complementary levels of screening would be deployed: AGRS helicopter, AGRS drones and ground team measurements. The helicopter based system, best suited for rapidly mapping extensive areas, was used to find the source and to define an area, in which a detailed source search should be performed. In the past, this area identified with the helicopter measurements was directly inspected by ground measuring teams. However, due to the field of view of the helicopter system (300 m) flying with a ground clearance of about 100 m, the detailed search could take hours. During ARM23c, an additional layer, using drones flying with a ground clearance of about 10 m, was introduced prior to the deployment of a ground-based search foreseen in a real event, dramatically reducing the area to be searched by ground teams. Drones were supplied and operated by the teams of Spiez Laboratory and Arktis Radiation Detectors Ltd.

The exercise started with the notification to the NEOC of stolen sources. After the evaluation of the situation, the helicopter was deployed to track and locate the stolen sources. The AGRS-team constantly received updates (as it would be done in a real situation by the police) on the presumed location of the sources, so that they could progressively restrict the screening area embedding the military training area where sources were placed. A  $^{137}\text{Cs}$  source with an activity of 751 MBq was placed in one location (Northern hotspot, closer to the river) and a  $^{137}\text{Cs}$ -source with 16.2 MBq was placed at a second location (South-Western hotspot) (Hotspot locations depicted for example in Figure 14).

The source search with the helicopter uses the operational software provided by the manufacturer of the RLL system (Mirion Technologies). Figure 6 shows the MMGC-ratio along the flight line of the last part of the search over the military training area together with radiation alarms and the information displayed for one of the alarm locations.

The radionuclide sources generate only a slight increase of the dose rate (Figure 7). A much clearer indication of the source position is obtained using the map of the Man-Made-Gross-Count (MMGC)-ratio (Figure 8). The online map of the MMGC-ratio provided by the Mirion software including isolines promptly yields areas marked for a detailed inspection. Figure 9 shows a screen shot of the map taken during the exercise.

As both source locations were only about 60 m apart, the helicopter measured a superposition of both sources. The according spectrum (Figure 10) displays clearly the photon peak of  $^{137}\text{Cs}$  at 662 keV together with photon peaks of natural radionuclides.

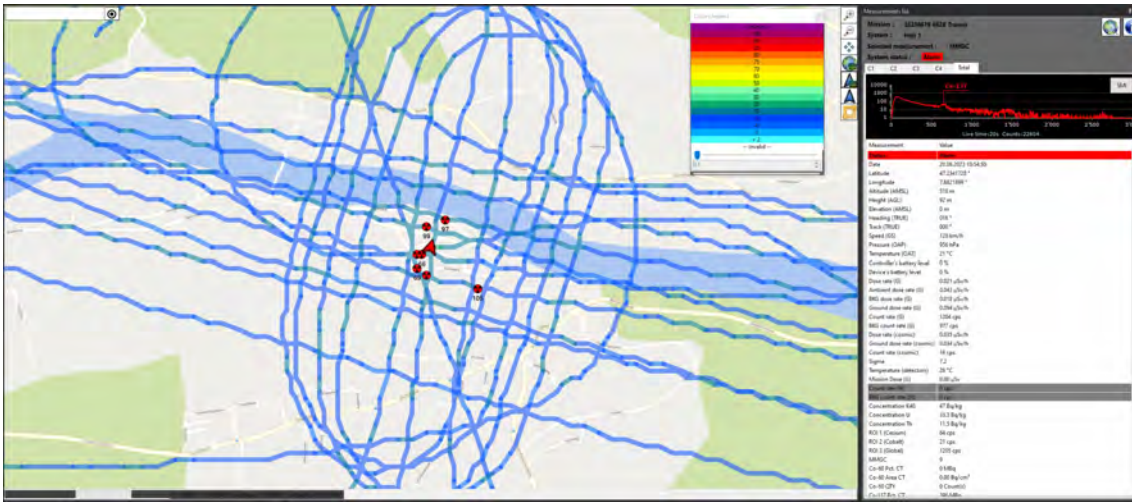


Figure 6: Screenshot of the Mirion software during the source search exercise displaying the MMGC-ratio along the flight line.

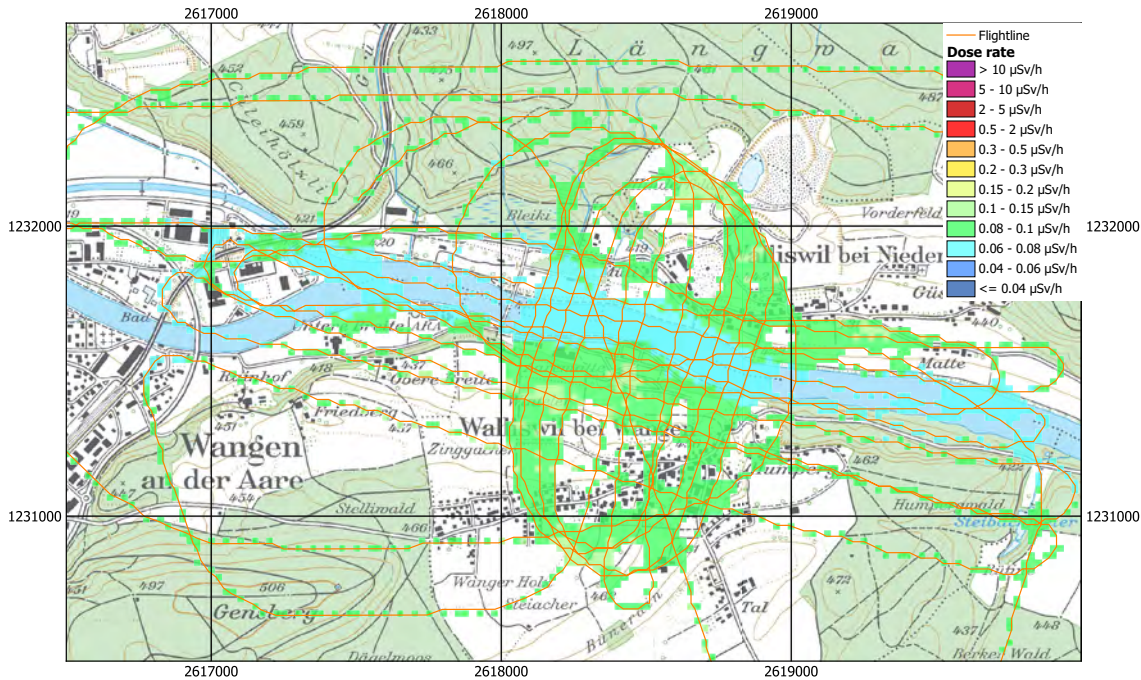


Figure 7: Dose rate over the source search area. Geodaten@swisstopo.

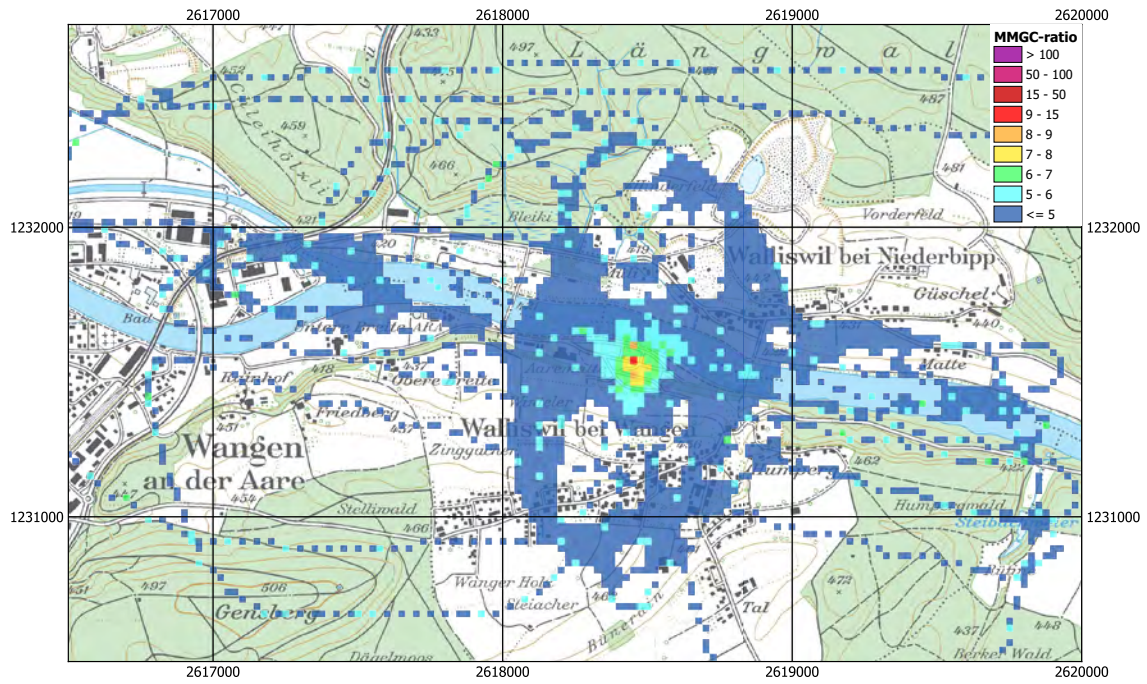


Figure 8: MMGC-ratio over the source search area. Geodaten©swisstopo.

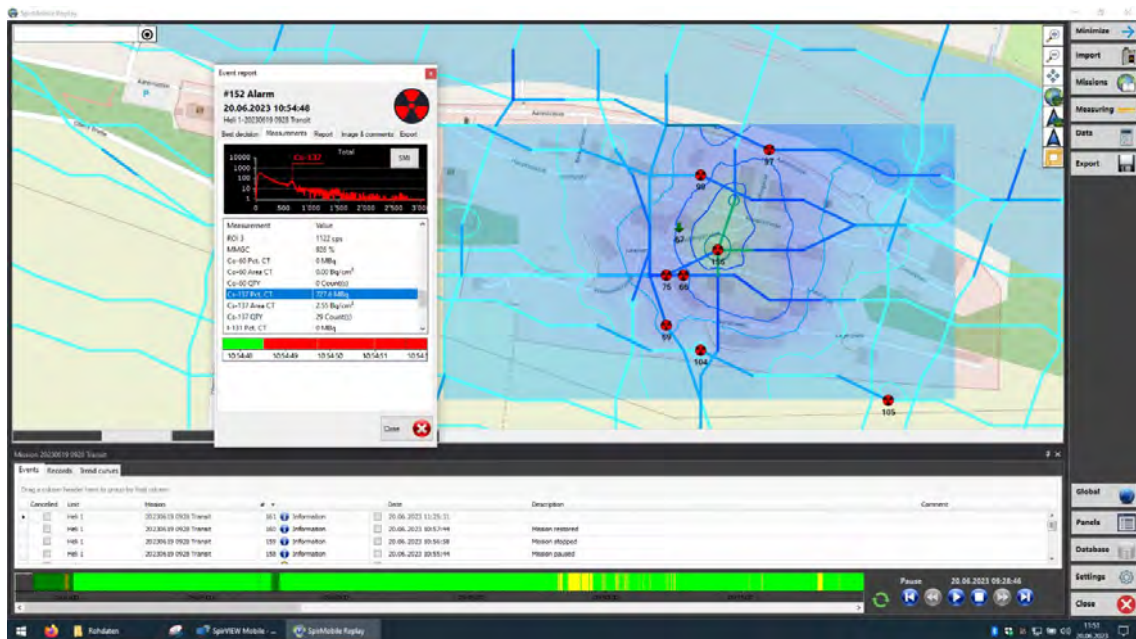


Figure 9: Screenshot of the MMGC-ratio map provided by the Mirion software during the source search exercise.

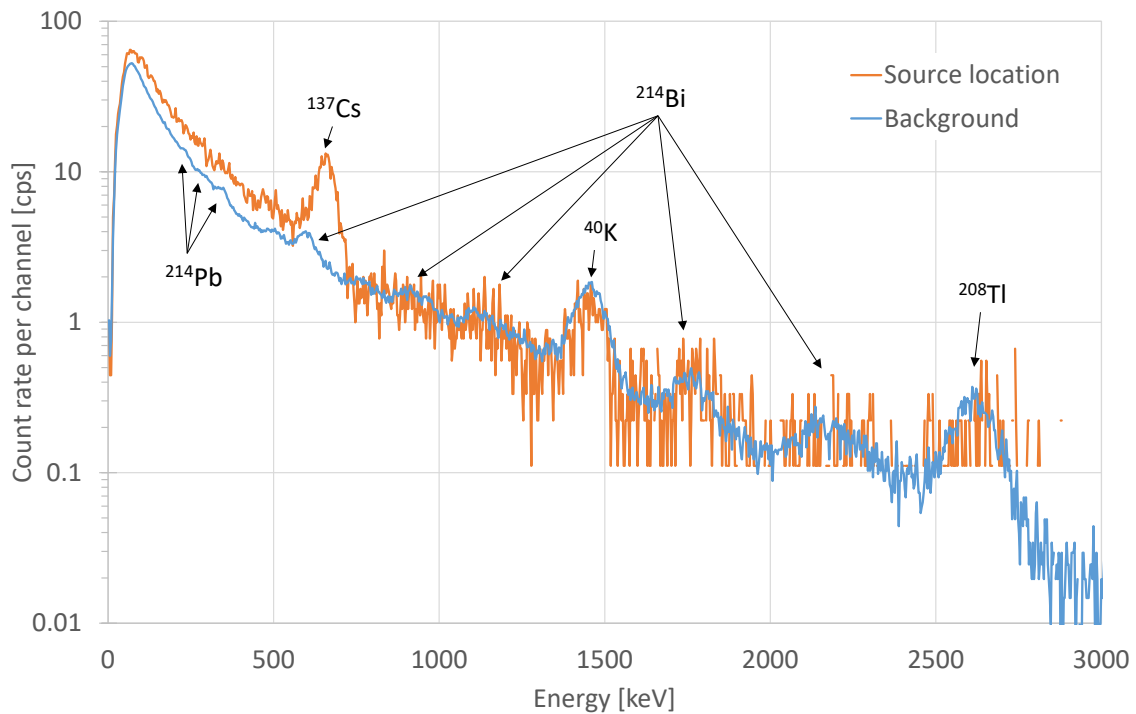


Figure 10: Gamma ray spectrum measured over the exercise area with the helicopter.

After the localisation of the radionuclide source by the helicopter-based system, two drone teams inspected the targeted area. For this part of the exercise, an additional  $^{133}\text{Ba}$  source of 442 MBq was placed at the location of the weak  $^{137}\text{Cs}$ -source.

The team of Spiez laboratory used a drone provided by the Swiss Drone and Robotics Centre (SDRC) in combination with a commercially available measuring system (NuEM Drones G) purchased from NuviaTech Instruments using a 3 x 3 inch NaI crystal as detector. The team of Arktis Radiation Detectors Ltd used their product called Arktis Airborne. The Arktis Airborne uses a flat panel plastic scintillation detector with a volume of 0.44 litres, a proprietary development of Arktis. Figure 11 shows both drones used in ARM23c. Both teams adopted the same search strategy, performing a first flight with a coarse raster pattern to further reduce the search area. Figure 12 shows a screenshot of the applied software with a map of dose rate measured with the Spiez drone. Figure 13 shows a screenshot of the Arktis user interface displaying a map of total count rate. Both maps indicate clearly two areas of interest, which were then inspected with a second flight with finer line spacing. Figures 14 and 15 show dose rate maps derived from the detailed scans of the potential source locations of both drone teams presented during the exercise. Both teams identified the source nuclides ( $^{137}\text{Cs}$  and  $^{133}\text{Ba}$ ) and determined an estimate of the activity of associated point sources. No system identified the weaker  $^{137}\text{Cs}$  source in the radiation field of the much stronger  $^{133}\text{Ba}$  source.

Due to the much better spatial resolution of the drones measuring with a ground clearance below 10 m, the spectral signature of the two source locations is well separated and the two radionuclides could be clearly identified both with the NaI detector of team Spiez (Figures 16 and 18) and the plastic scintillator used by team Arktis (Figures 17 and 19). It is worth to note the absence of photo peaks in the spectra acquired by the Arktis RDD (Figures 17 and 19), since the detection unit is a plastic scintillator. The nuclide identification and estimation of the activity has been accomplished by a proprietary analysis and deconvolution of the Compton continuum, developed by Arktis. Table 5 summarises the source activities derived from the measurements in comparison to the certified activities of the sources. The activ-

ity of the stronger  $^{137}\text{Cs}$  source was derived from the helicopter measurement on-line with the operational Mirion software and during post-processing with the independent software AGS\_CH based on the methodology published by Schwarz (1991) and Bucher (2001). All results show reasonable agreement with the certified activities.

	Activity [MBq]	
	$^{137}\text{Cs}$ source	$^{133}\text{Ba}$ source
Source activity	751	442
Helicopter (Mirion)	727	-
Helicopter (AGS_CH)	762	-
Spiez drone	670	425
Arktis drone	590-800	530-780

Table 5: Results of the source search.



Figure 11: Drones used in the source search exercise. Front: Drone of team Arktis, Rear: Drone of team Spiez.

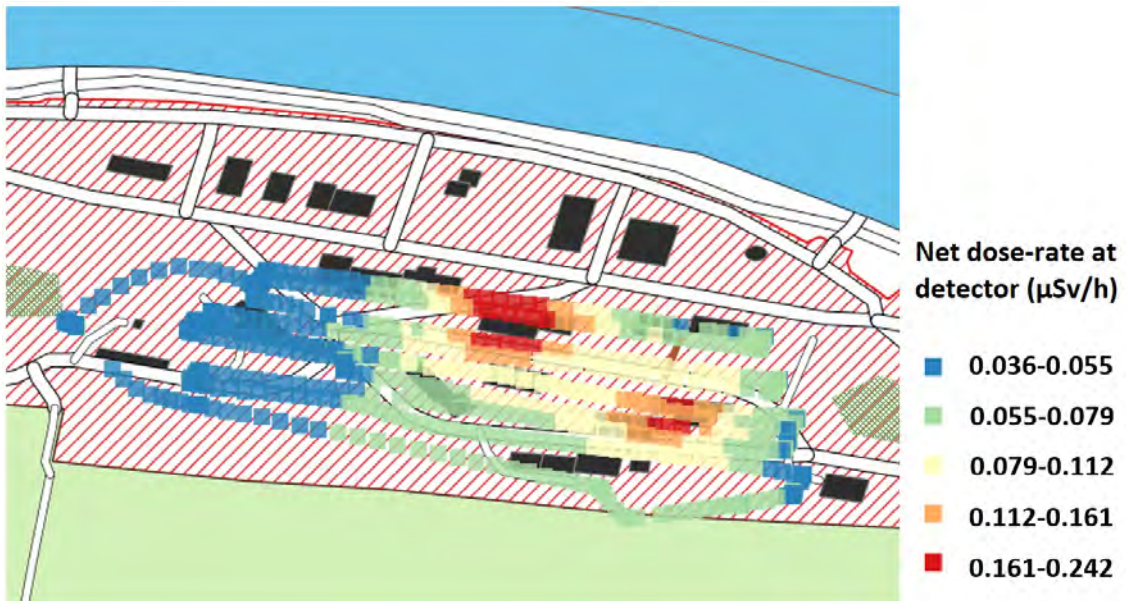


Figure 12: Dose rate over the source search area measured by drone team Spiez.

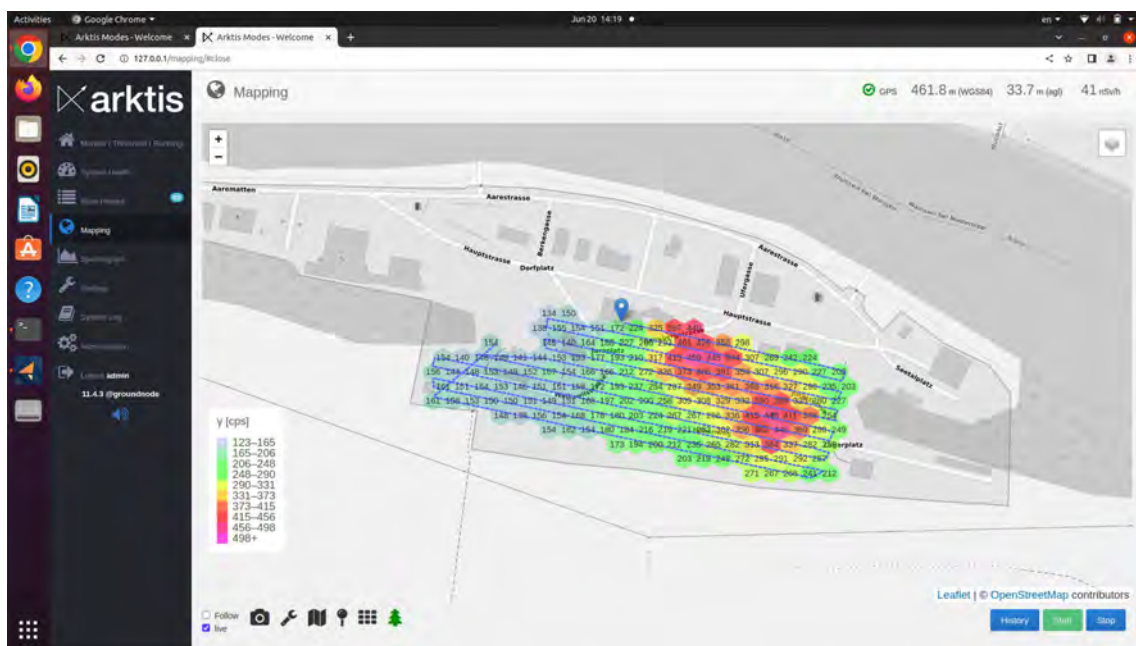


Figure 13: Total count rate over the source search area measured by drone team Arktis.



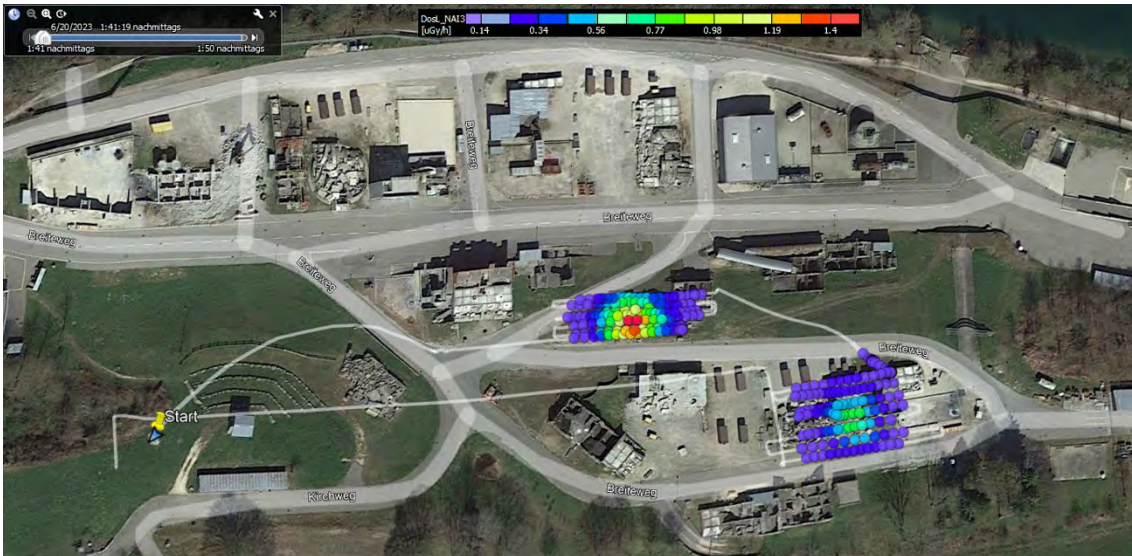


Figure 14: Dose rate over the potential source locations measured by drone team Spiez.

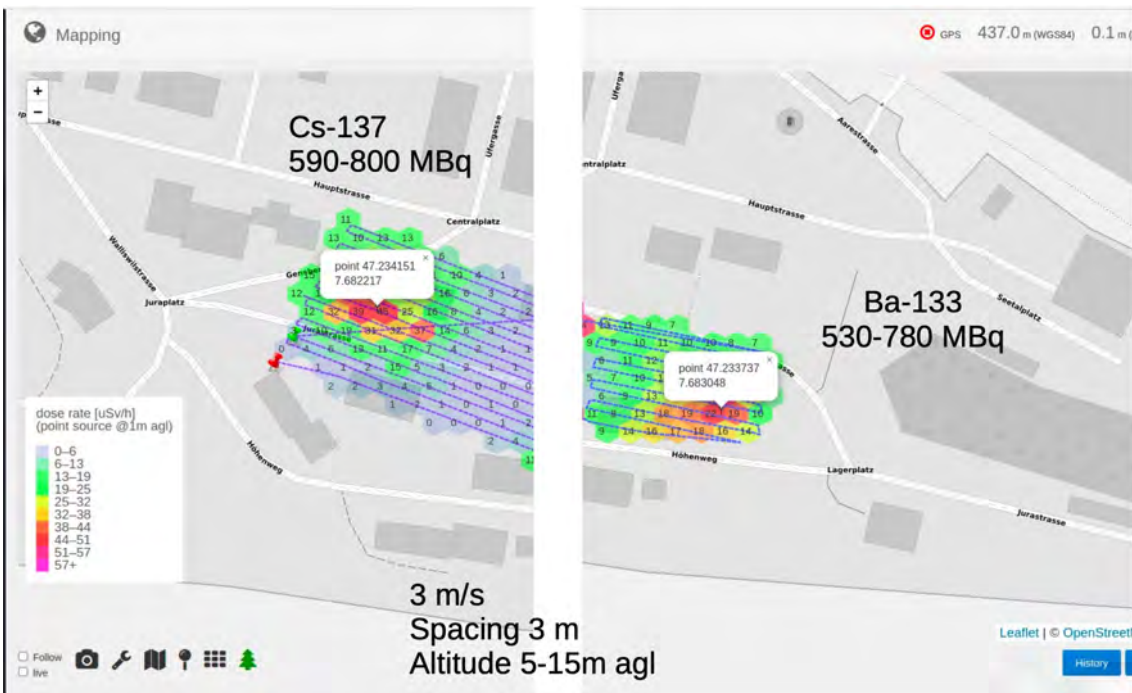


Figure 15: Dose rate over the potential source locations measured by drone team Arktis.

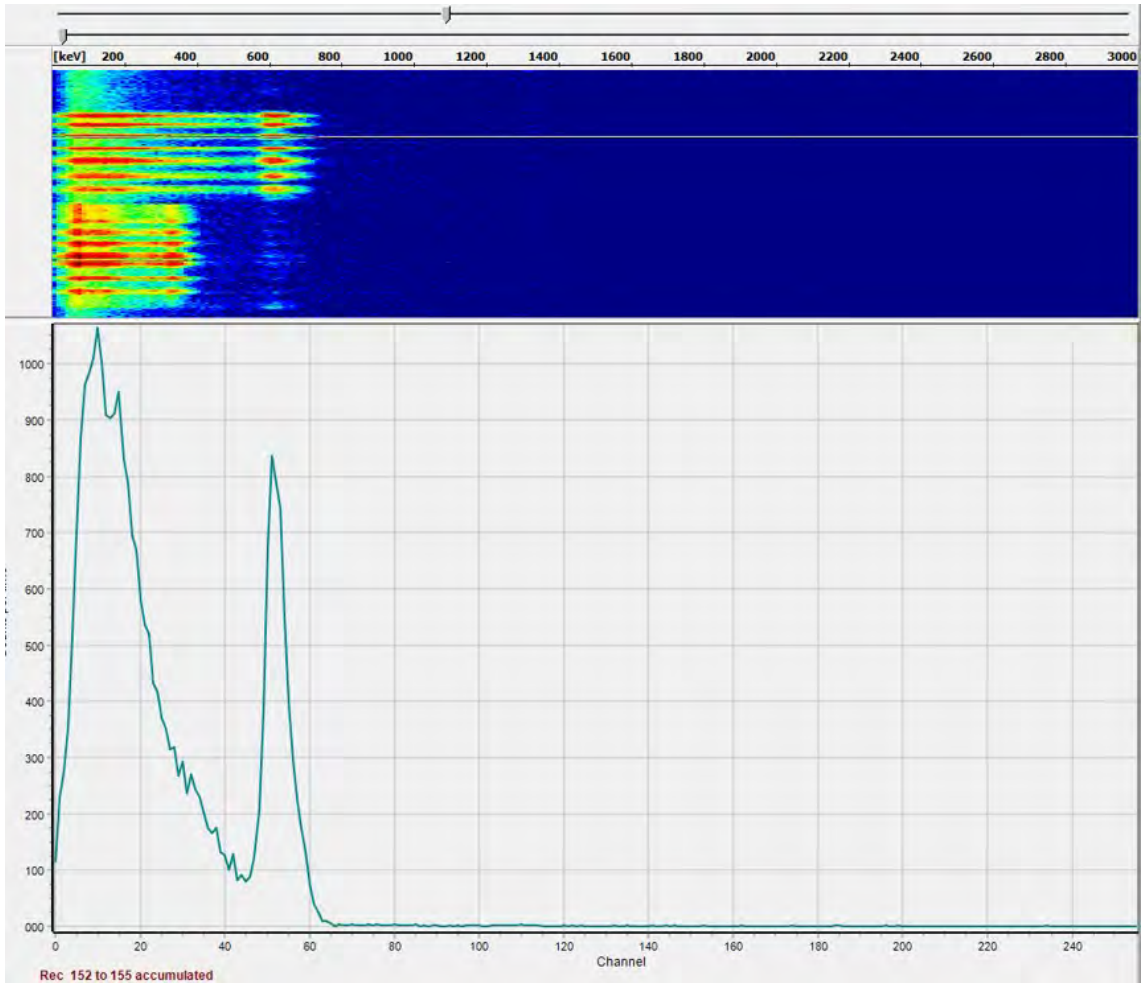


Figure 16: Gamma ray spectrum measured over the  $^{137}\text{Cs}$  source with the Speiz drone.

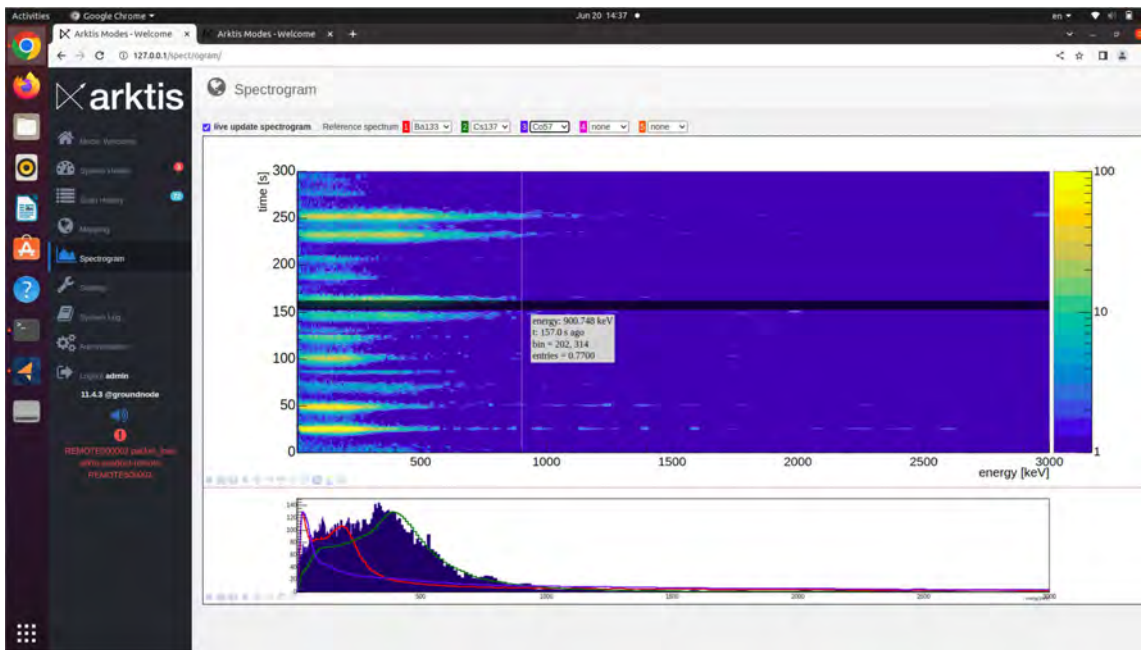


Figure 17: Gamma ray spectrum measured over the  $^{137}\text{Cs}$  source with the Arktis drone.

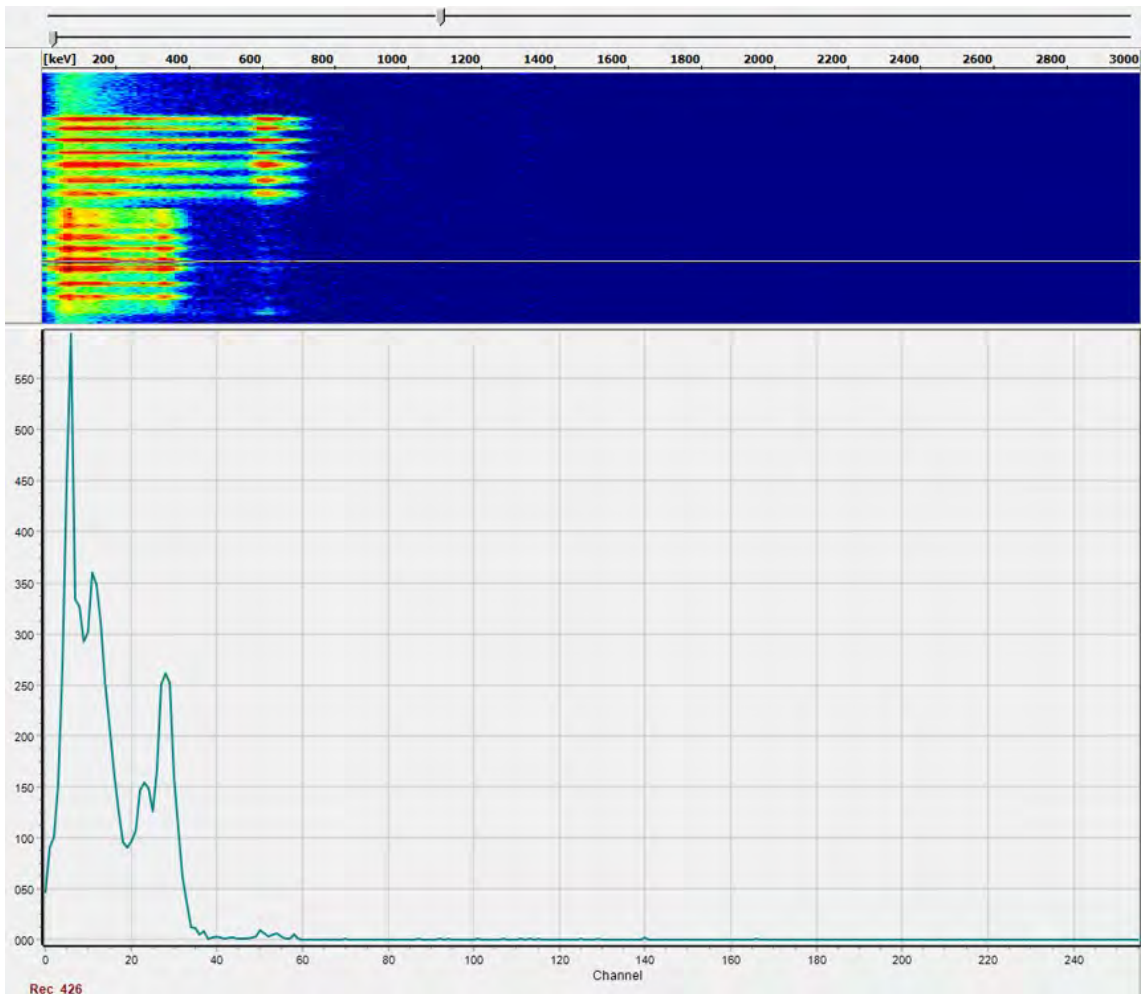


Figure 18: Gamma ray spectrum measured over the  $^{133}\text{Ba}$  source with the Spiez drone.

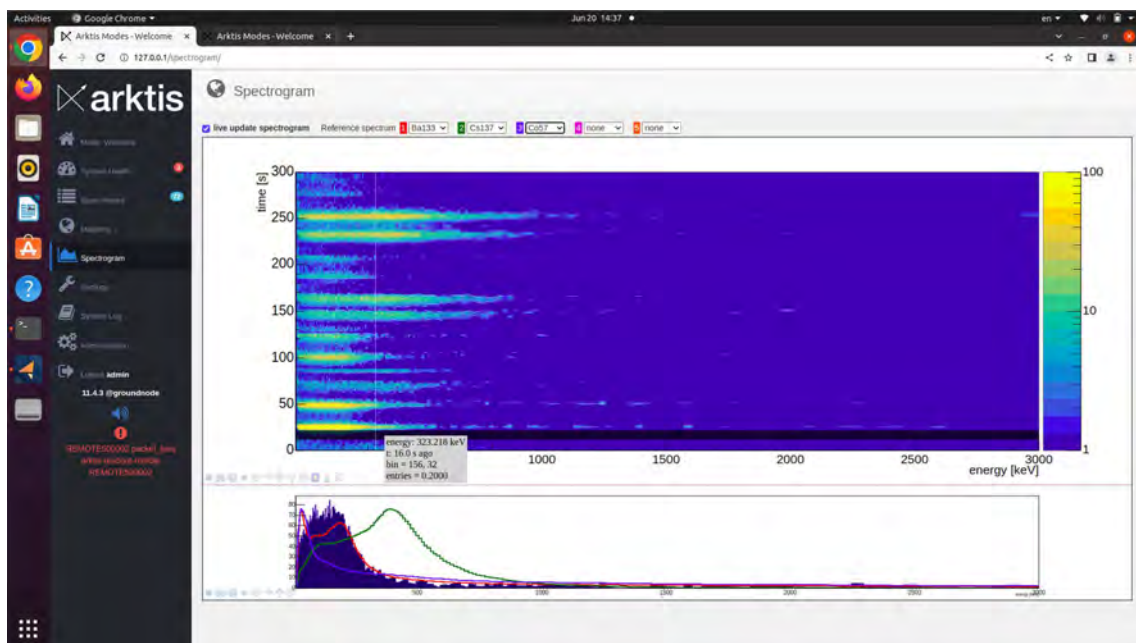


Figure 19: Gamma ray spectrum measured over the  $^{133}\text{Ba}$  source with the Arktis drone.

### 2.1.2 Spiez

ARM23m included a source search exercise with three radionuclide sources of the radionuclides  $^{137}\text{Cs}$  (41 GBq),  $^{60}\text{Co}$  (60 MBq) and  $^{133}\text{Ba}$  (426 MBq) placed on the premises of the NBC-EOD Centre of Competence in Spiez. The map of the dose rate (Figure 20) shows a clear signal over the location of the sources. The map of the MMGC-ratio (Figure 21) indicates the presence of man-made radionuclides. Zooming in on the map of the MMGC-ratio gridded with a finer cell size of 25 m (Figure 22) defines the area of interest for a ground based search, which very well overlaps with the actual exposure location of the sources (Figure 23). The photon spectrum over the source location (Figure 25) clearly shows the photo peak of  $^{137}\text{Cs}$  at 662 keV. The double photo peaks of  $^{60}\text{Co}$  at 1173 keV and 1332 keV are also visible. The signal from the  $^{133}\text{Ba}$  source, expected at 81 keV, 276 keV, 302 keV and 384 keV, is obscured by Compton scattered photons of the much stronger  $^{137}\text{Cs}$  source and emissions at 242 keV, 295 keV and 352 keV from the natural radon decay product  $^{214}\text{Pb}$ . The activities were determined during post-processing with AGS\_CH to be 33 GBq for the  $^{137}\text{Cs}$  source and 261 MBq for the  $^{60}\text{Co}$  source. The calculated  $^{137}\text{Cs}$  source activity shows a larger deviation to the placed source activity than observed during the source search in Wangen (Section 2.1). Follow-up clarifications attributed the cause for the observed activity underestimation of the  $^{137}\text{Cs}$  source to the fact that, during the measurement exercise, the source was set in position in its shielded container, only removing its lid (Figure 24). This produced a collimated field, resulting ultimately in an underestimation of the source's activity. The calculated activity of the  $^{60}\text{Co}$  source differs even further from the true value. The most likely cause of its overestimation lies with the fact that the nominal activity of the  $^{60}\text{Co}$  source was well below the detection limit of the system.

The proprietary software of the RLL system estimated the activity of the  $^{137}\text{Cs}$ -source to 27 GBq, an even lower value compared to AGS\_CH. Neither the  $^{60}\text{Co}$ - nor the  $^{133}\text{Ba}$ -sources were detected by the RLL software.

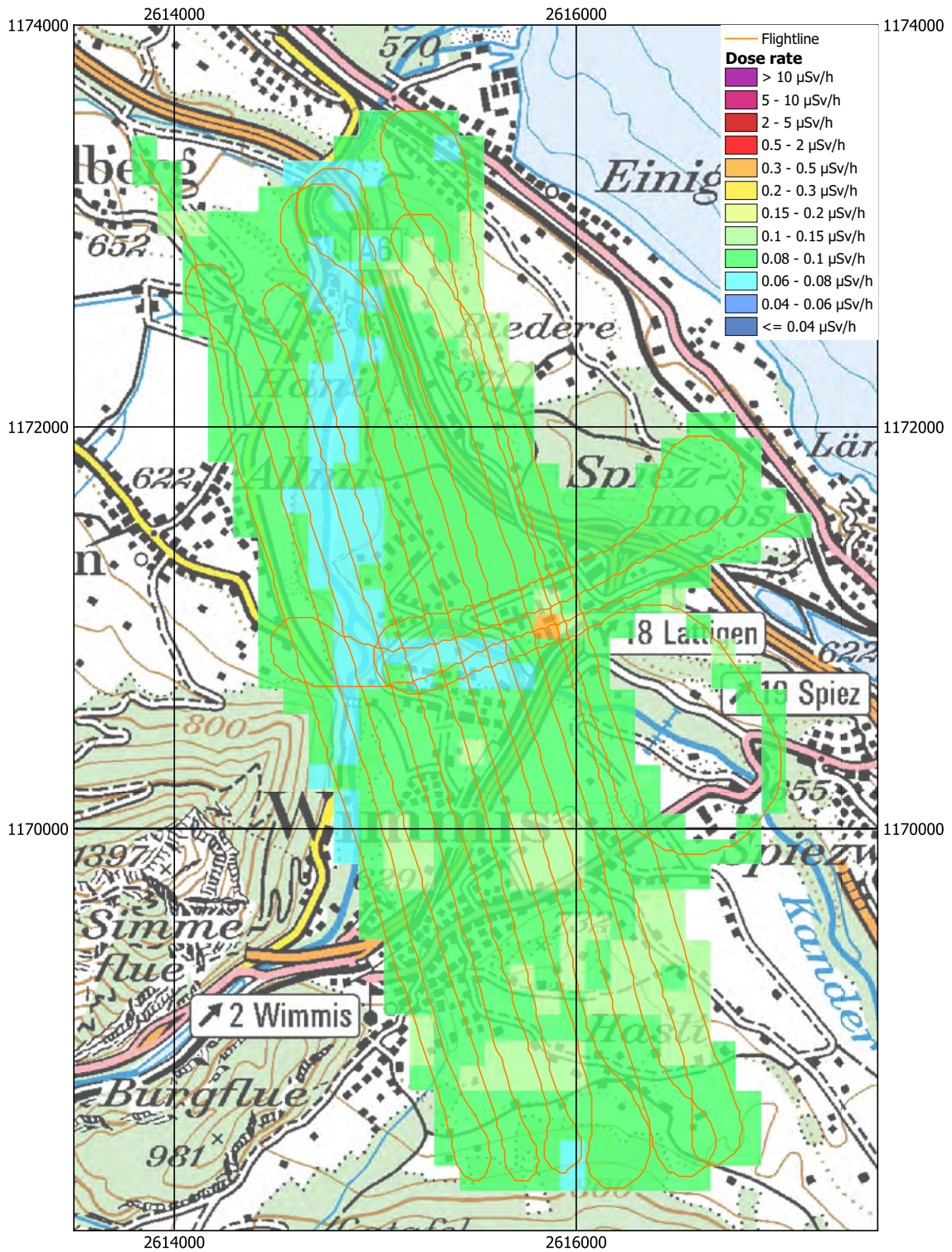


Figure 20: Dose rate of the source search exercise near Spiez. Geodaten@swisstopo.

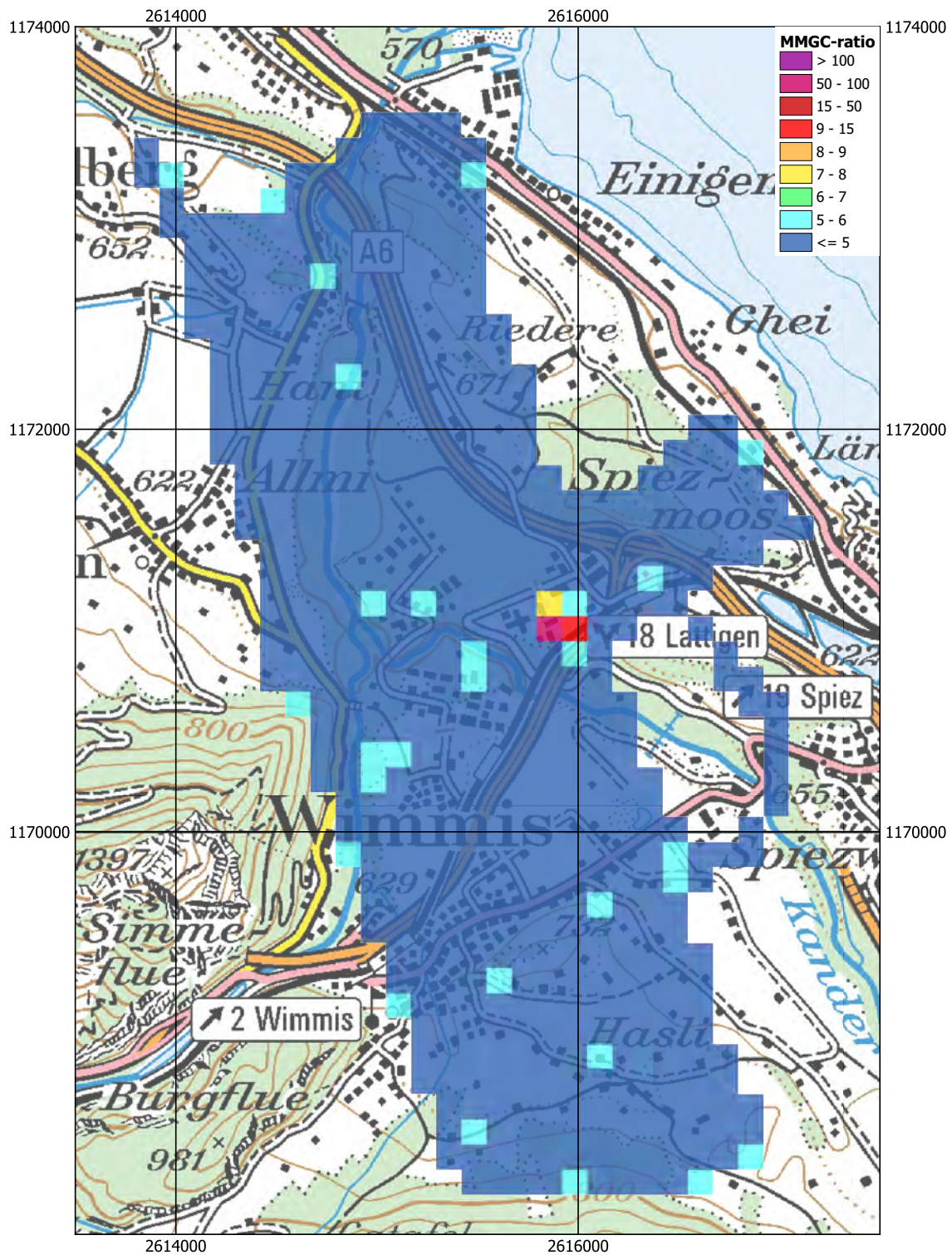


Figure 21: MMGC-ratio of the source search exercise near Spiez. Geodaten@swisstopo.

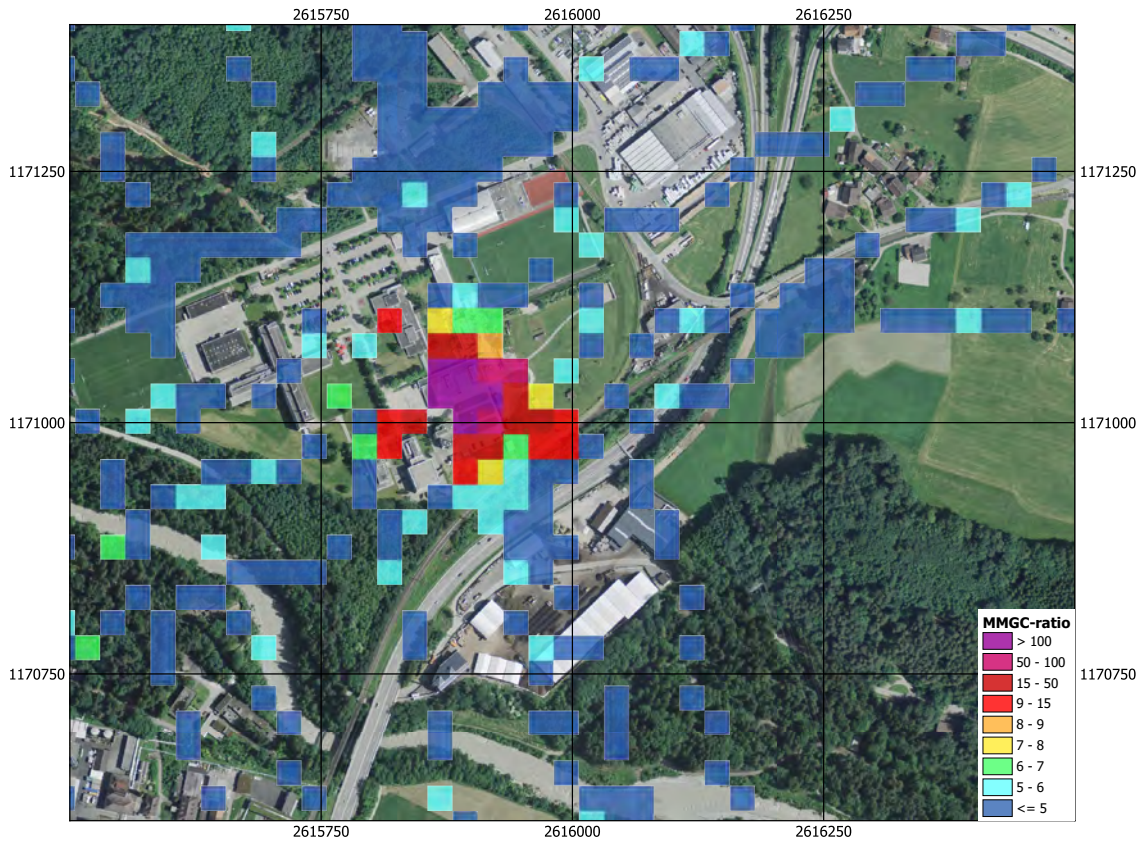


Figure 22: MMGC-ratio of the source search exercise near Spiez. Geodaten@swisstopo.

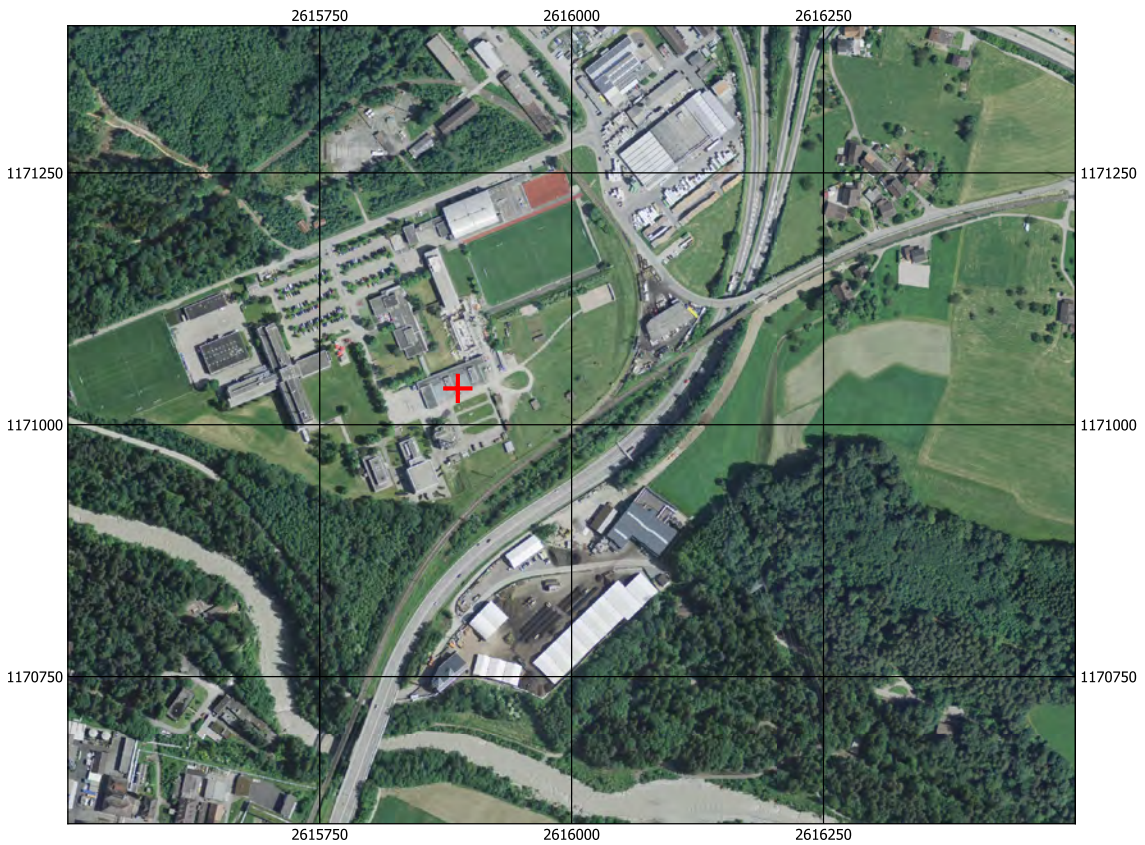


Figure 23: Exposure location of the source search exercise near Spiez. Geodaten@swisstopo.



Figure 24: Picture of the exposure location of the source search exercise near Spiez.

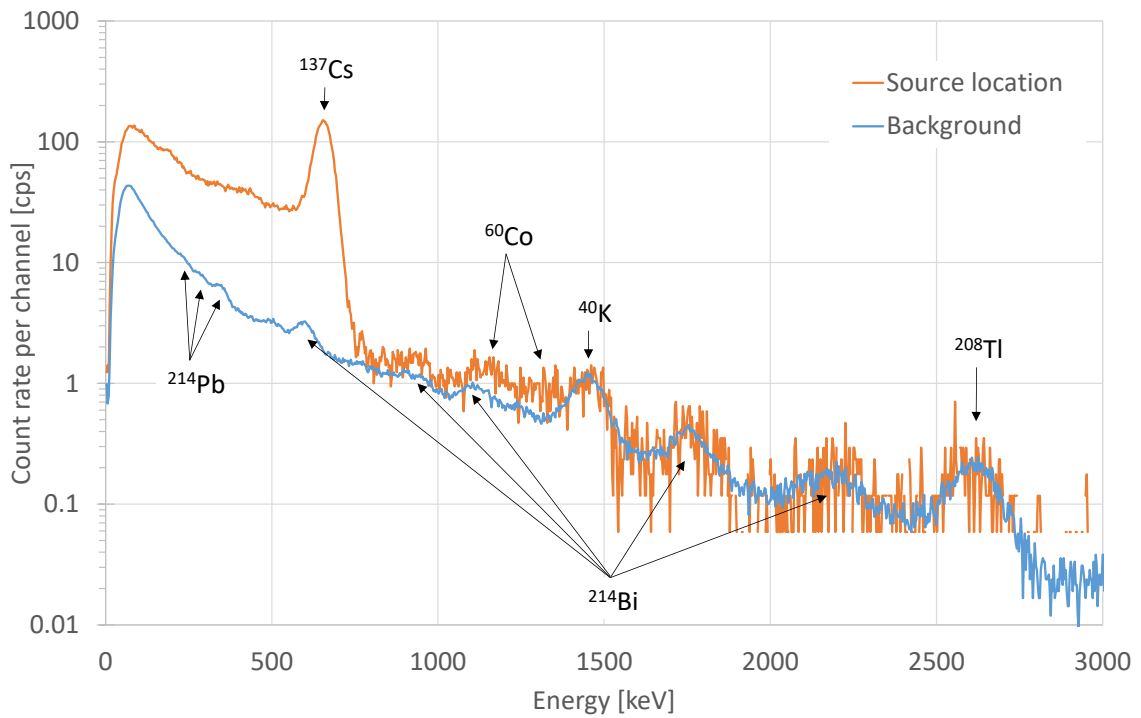


Figure 25: Gamma ray spectrum measured over the source location.



## 2.2 Recurrent measurements over Swiss nuclear installations

Following a request of the Swiss Nuclear Safety Inspectorate (ENSI), the vicinity of Swiss nuclear installations was measured with airborne gamma-spectrometry following a bi-annual schedule.

### 2.2.1 KKG

The environs of the nuclear power plant Gösgen (KKG) were inspected in 2023. A region to the south of the nuclear power plant was added to the survey to complement the background measurements over the safety zones around KKG.

The dose rate map (Figure 26) shows variations due to different concentrations of natural radionuclides and the attenuation of water layers. The pressurised water reactor of nuclear power plant Gösgen (KKG) does not appear in the measurements because no activation products of the primary cooling circuit leave the well shielded reactor building. The man-made gross-count (MMGC) ratio, an indicator for the presence of man-made radionuclides, does not show elevated values in the measurement areas (Figure 27). The activity concentration of the natural radionuclide  $^{232}\text{Th}$  (Figure 28) shows typical values for northern Switzerland.

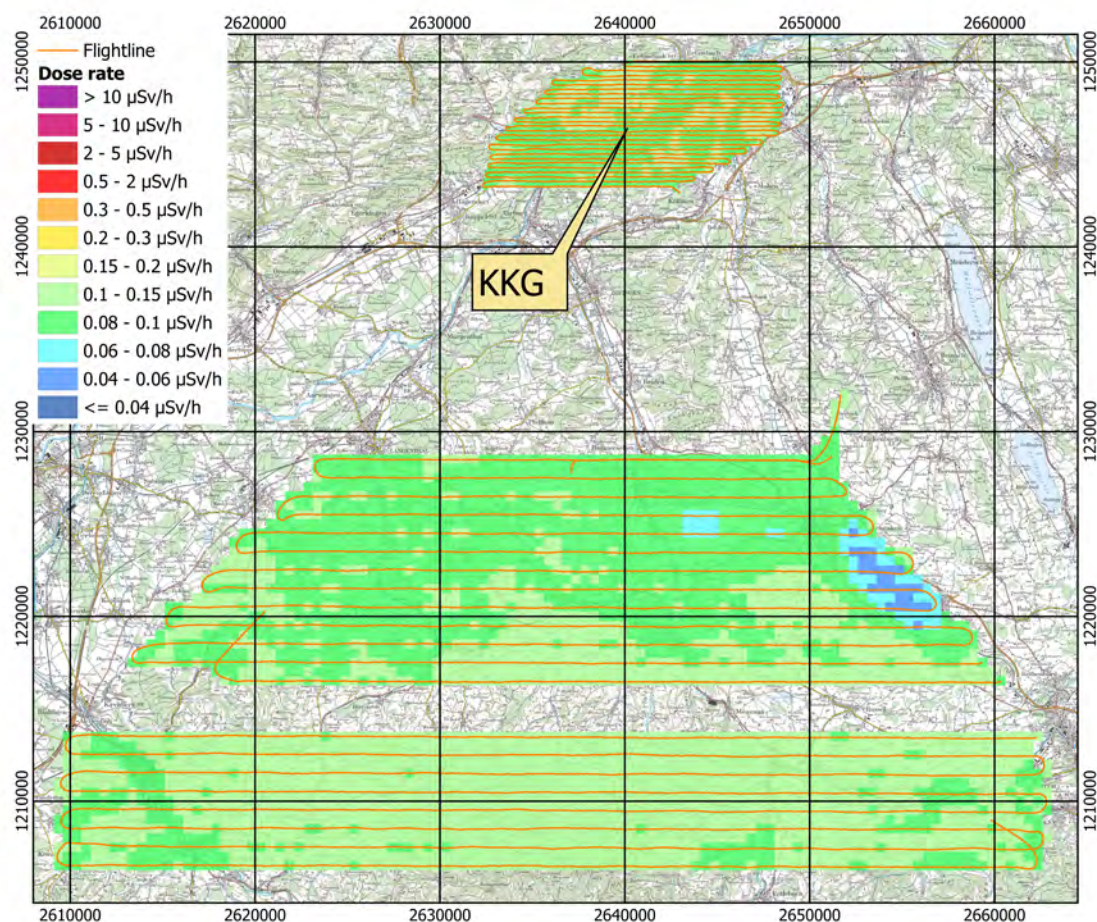


Figure 26: Dose rate in the vicinity and to the south of KKG. Geodaten©swisstopo.

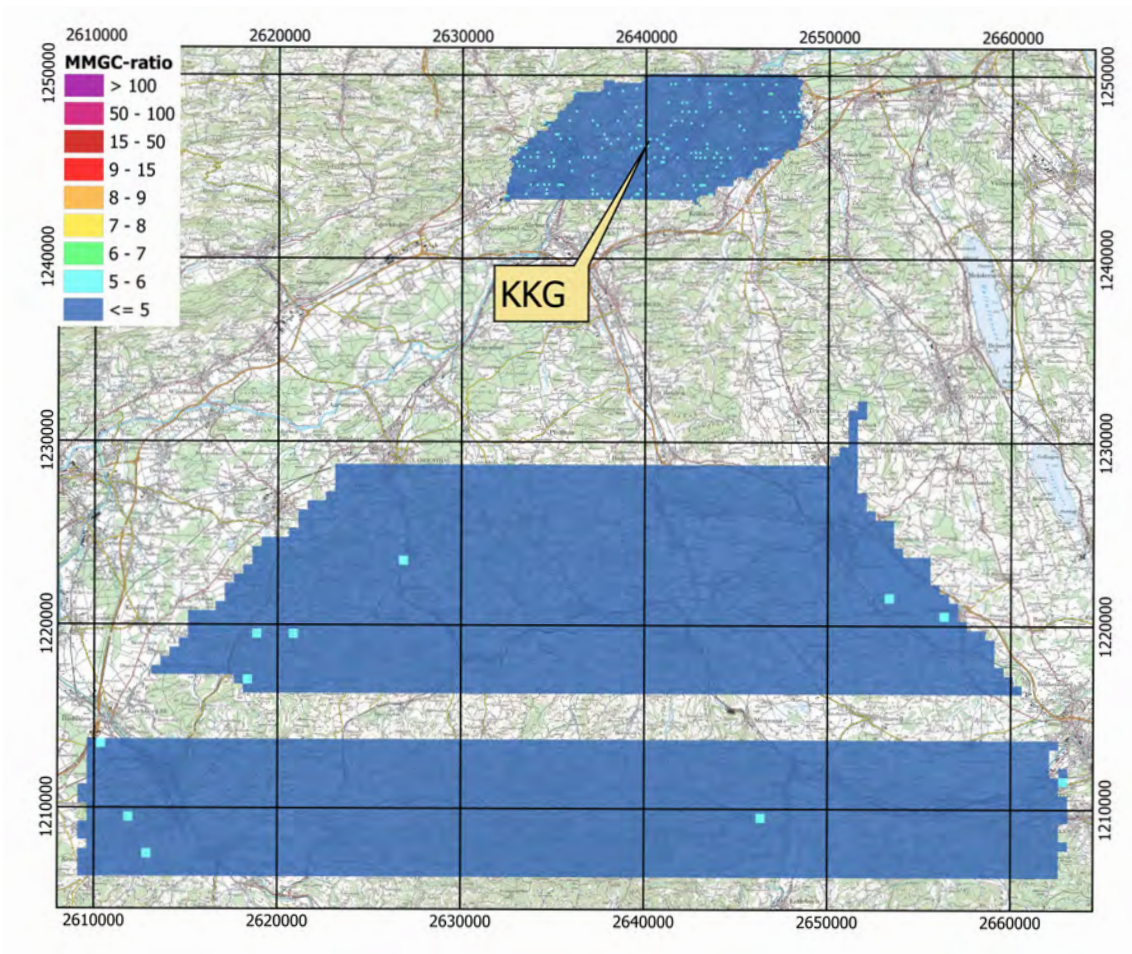


Figure 27: MMGC-ratio in the vicinity and to the south of KKG. Geodaten©swisstopo.

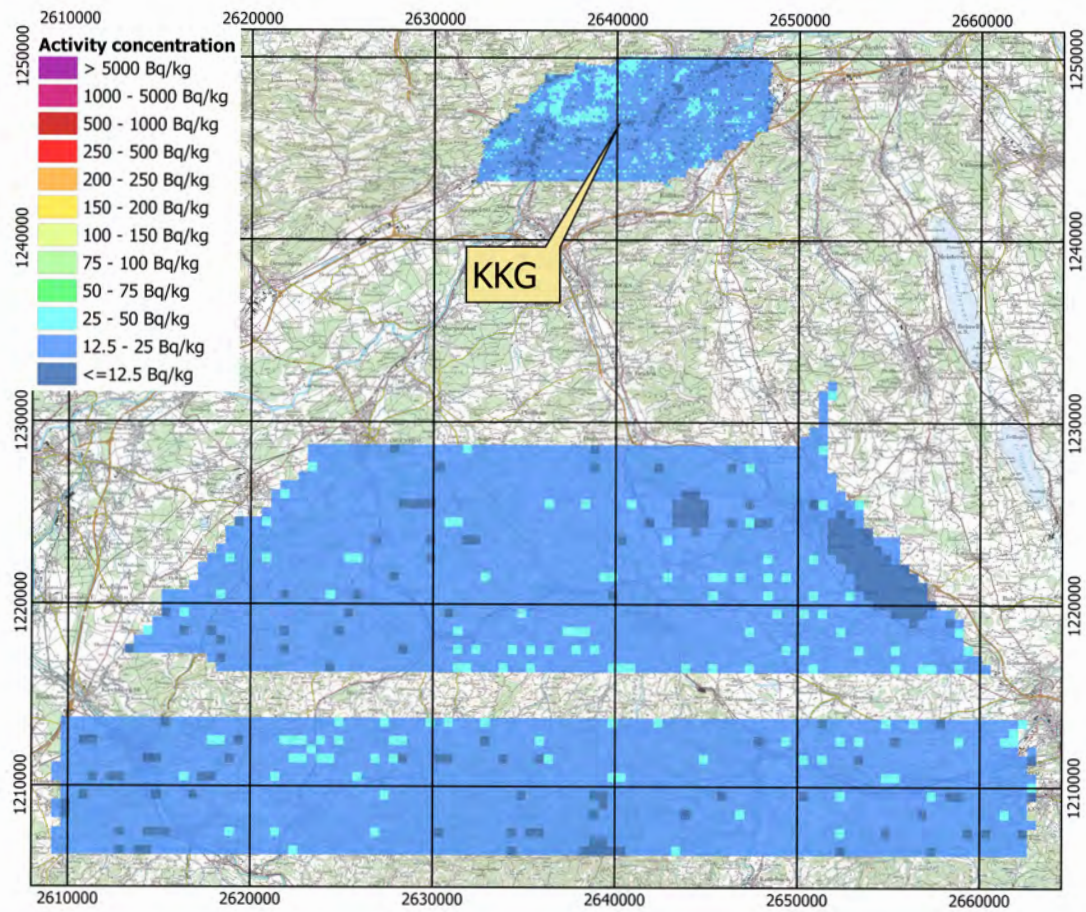


Figure 28:  $^{232}\text{Th}$  activity concentration in the vicinity and to the south of KKG.  
Geodaten@swisstopo.

## 2.2.2 KKM

The nuclear power plant Mühleberg (KKM) is in decommissioning since 2019. Due to the decommissioning process, activated material is removed from the shielded reactor building, processed and stored temporarily on the plant premises. The regulator (ENSI) is informed about the stored components and constantly monitors the compliance to legal dose rate limits. The radioactive components stored temporarily on the plant premises are clearly detected by the RLL system, as can be inferred from both dose-rate and MMGC maps (Figures 30 and 31). Besides the photo peaks of the natural radionuclides  $^{40}\text{K}$ ,  $^{214}\text{Bi}$  and  $^{208}\text{Tl}$ , the spectrum acquired over the plant premises (Figure 29) features additionally the distinctive photon signature emitted by the radionuclide  $^{60}\text{Co}$ , one of the most common activation products found in steel components of nuclear power plants.

The map of the natural radionuclide  $^{232}\text{Th}$  (Figure 32) displays typical activity concentrations for northern Switzerland.

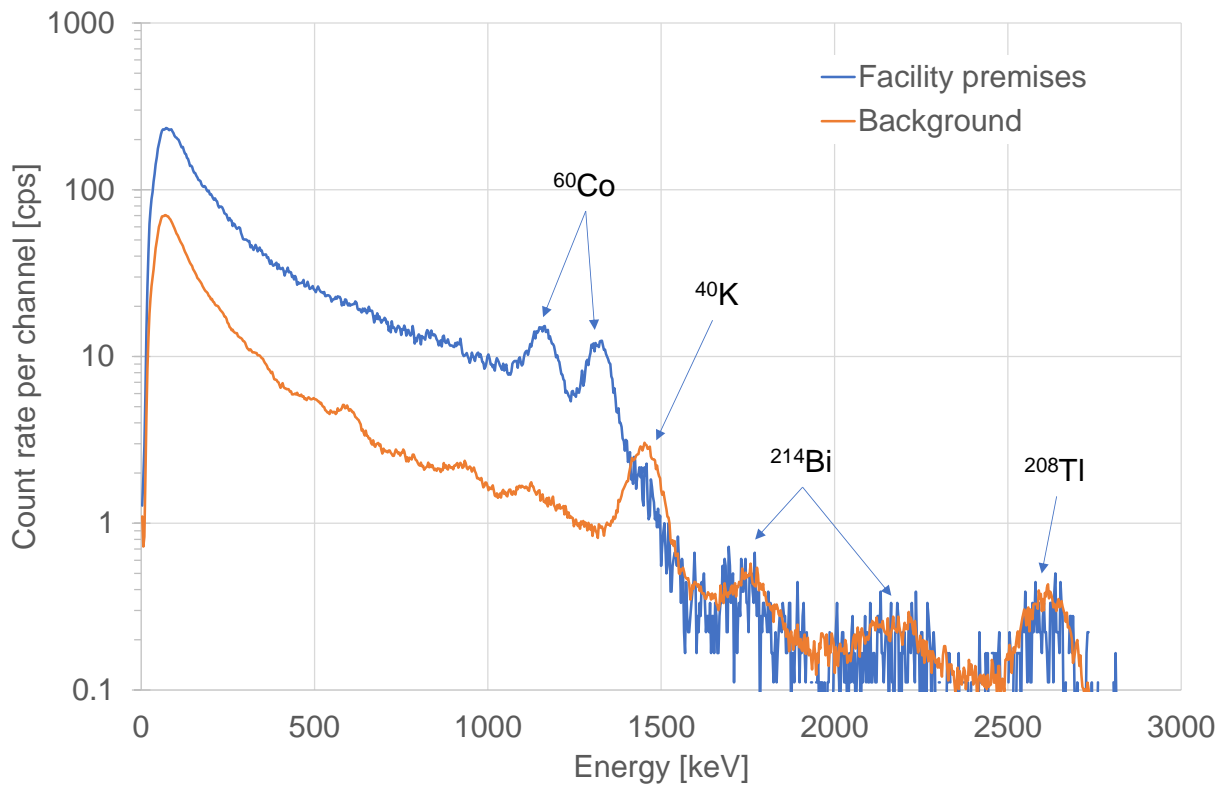


Figure 29: Photon spectrum over KKM premises compared to background.

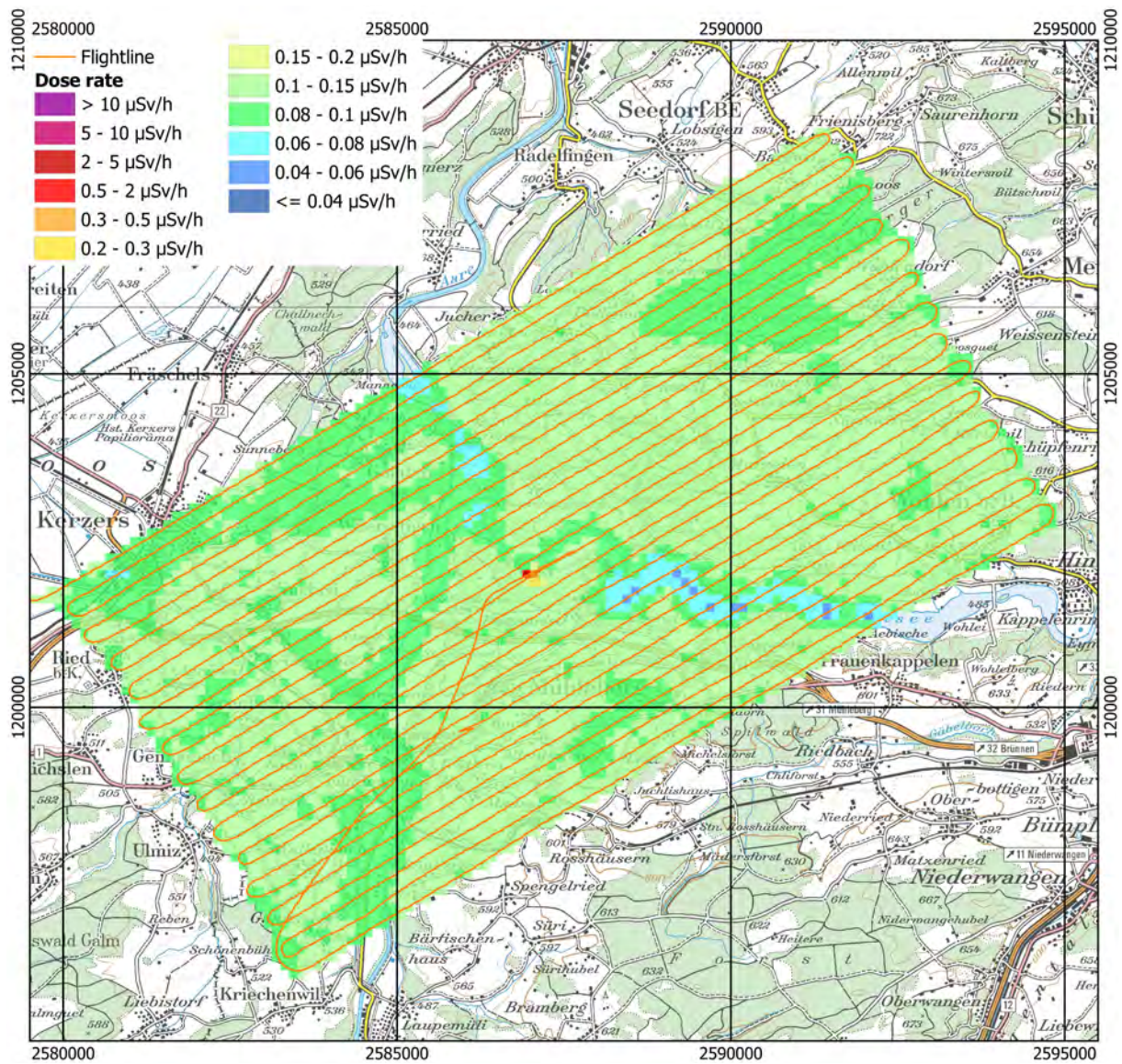


Figure 30: Dose rate in the vicinity of KKM. Geodaten©swisstopo.

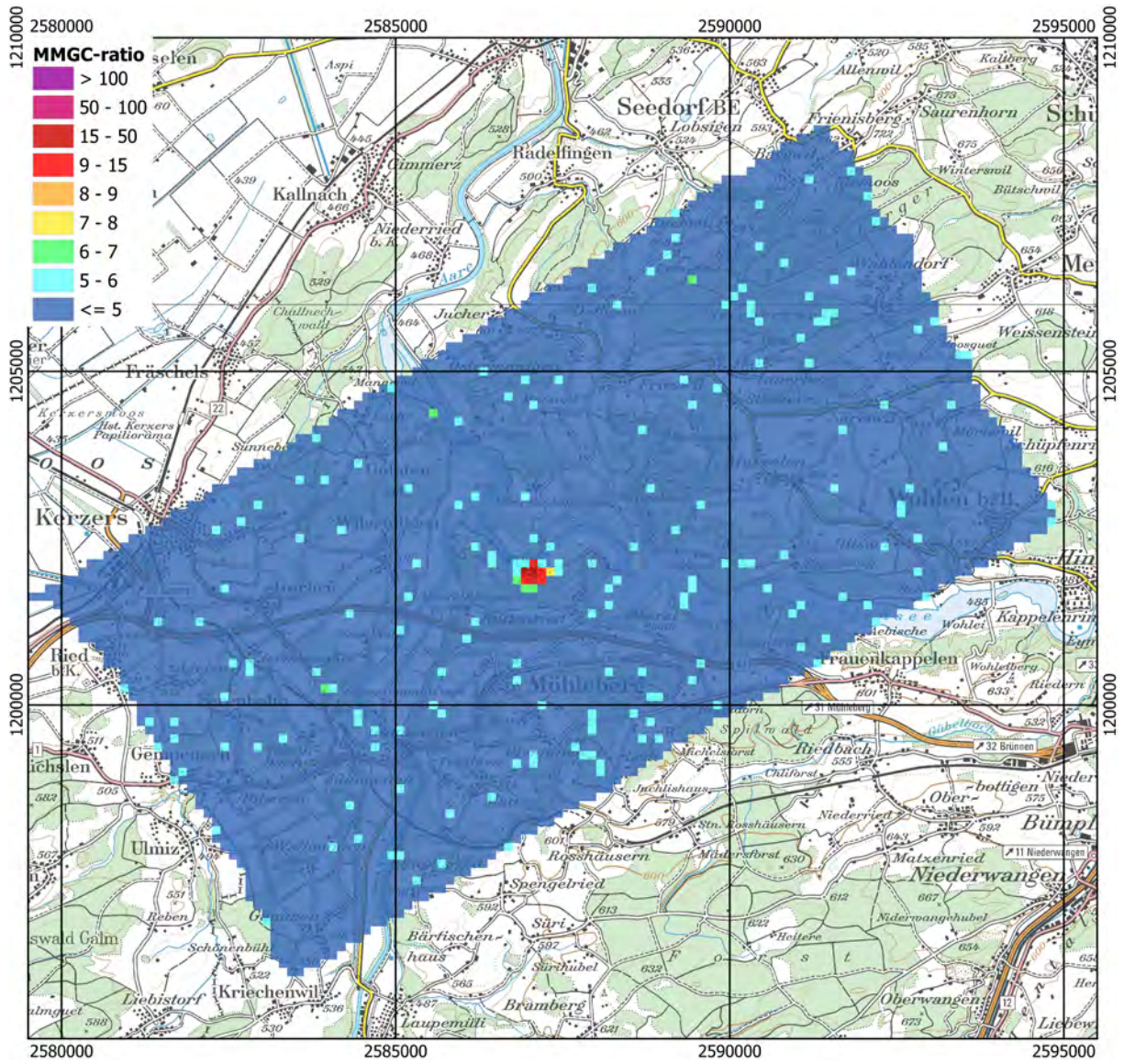


Figure 31: MMGC-ratio in the vicinity of KKM. Geodaten©swisstopo.

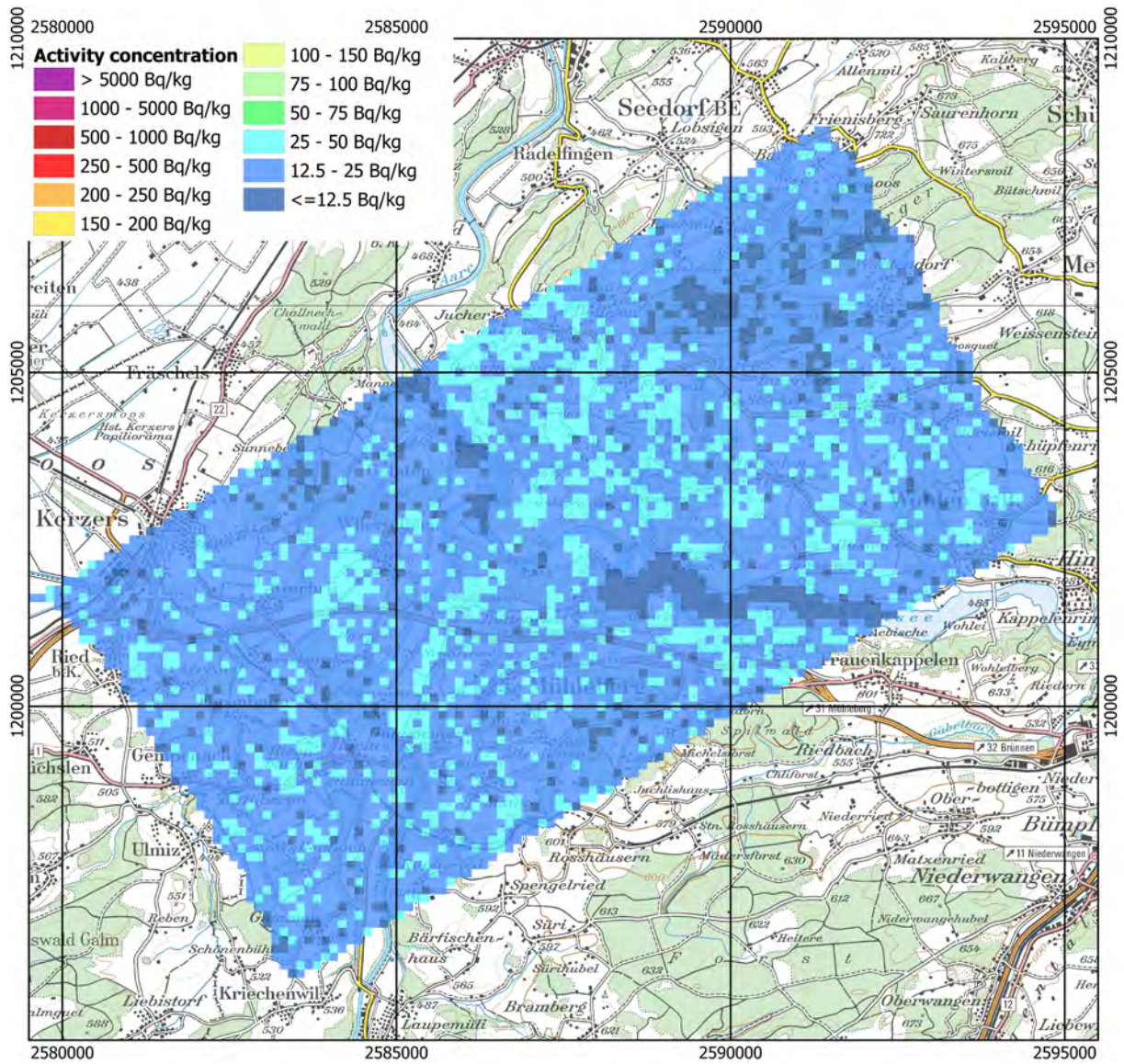


Figure 32:  $^{232}\text{Th}$  activity concentration in the vicinity of KKM. Geodaten©swisstopo.

## 2.3 Background measurements over Swiss cities and regions

The annual aeroradiometric exercises are used to measure the radiological background of Swiss cities and regions to obtain reference values in case of a radiological emergency.

### 2.3.1 Bercher

Bercher is located in the Gros-de-Vaud district to the south of Lake Neuchâtel. The only remarkable feature in the dose rate map (Figure 34) is the reduced dose rate over Lake Neuchâtel in the north of the measuring area due to absorption of terrestrial radiation in the water layer. The map of the Man-Made-Gross-Count (MMGC) ratio (Figure 35) yields no indication of man-made radionuclides in the measuring area. The map of the  $^{232}\text{Th}$  activity concentration (Figure 36) depicts typical values for Swiss rocks and soil.

The flights over the Bercher area were performed on September 11<sup>th</sup>, 13<sup>th</sup> and 14<sup>th</sup>. September 13<sup>th</sup> was locally a rainy day, which was used to study the influence of precipitation on the measuring signal and eight flight lines, already measured on September 11<sup>th</sup>, were repeated on September 13<sup>th</sup>. Figure 37 shows the terrestrial component of the dose rate measured on September 11<sup>th</sup> under dry conditions. Comparing with the identical map measured during rain on September 13<sup>th</sup>, a clear rise of terrestrial dose rate can be observed. The increase of the terrestrial dose rate is caused by the deposition of airborne radon progeny to the ground by rain drops (called rain-out or washout). A comparison of the average photon spectra over the area with the measurement repetition (Figure 33) shows no changes for the photo-peaks of  $^{40}\text{K}$  at 1460 keV and  $^{208}\text{Tl}$  at 2615 keV. The photo peak of  $^{208}\text{Tl}$  is used to determine the activity concentration of  $^{232}\text{Th}$ . An elevated count rate in the main photo peaks of the short-lived radon decay products  $^{214}\text{Pb}$  (242 keV, 295 keV and 352 keV) and  $^{214}\text{Bi}$  (609 keV, 786 keV, 934 keV, 1120 keV, 1238 keV, 1378 keV, 1408 keV, 1509 keV, 1730 keV, 1765 keV, 1847 keV, 2119 keV, 2204 keV, 2448 keV) can be observed in the average photon spectrum of rainy September 13<sup>th</sup>. The photon emission at 1765 keV of  $^{214}\text{Bi}$  is used for the determination of  $^{238}\text{U}$  activity concentration in soil and rock. Thus, the precipitated airborne  $^{214}\text{Bi}$  leads to an overestimation of the uranium activity concentration, as can be clearly identified comparing the maps of  $^{238}\text{U}$  activity concentration determined from the data measured on September 11<sup>th</sup> (Figure 39) and September 13<sup>th</sup> (Figure 40). This dependence of the  $^{238}\text{U}$  activity concentration calculated from the  $^{214}\text{Bi}$  emission at 1765 keV acquired flying during or shortly after precipitation events advises special diligence in the interpretation of the derived  $^{238}\text{U}$  activity concentration. The influence of this washout on ground-level dose rate is nonetheless well known, explaining why environmental dose rate monitoring probes are generally equipped with rain sensors, or integrated into meteorological measurement networks.



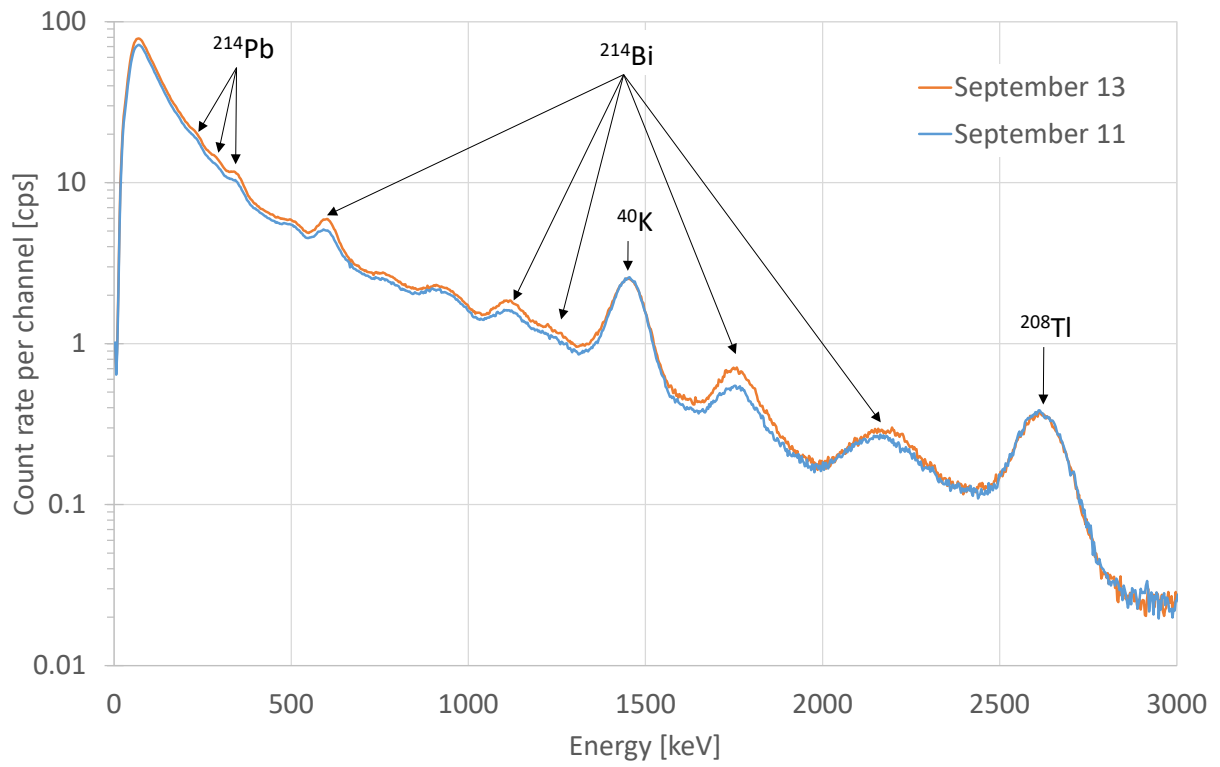


Figure 33: Photon spectra near Bercher measured with (13.9.) and without (11.9.) rain.

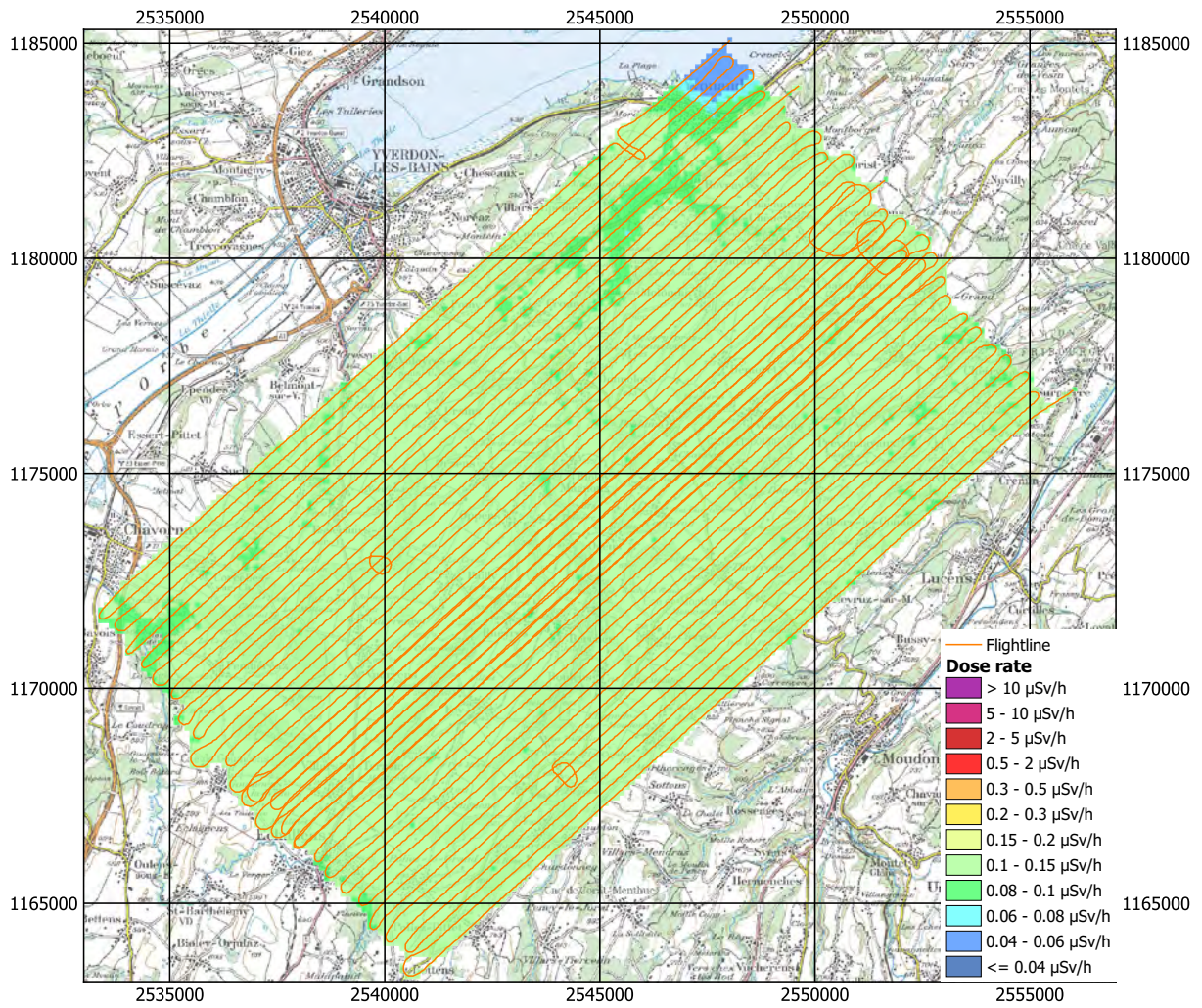


Figure 34: Dose rate near Bercher. Geodaten©swisstopo.

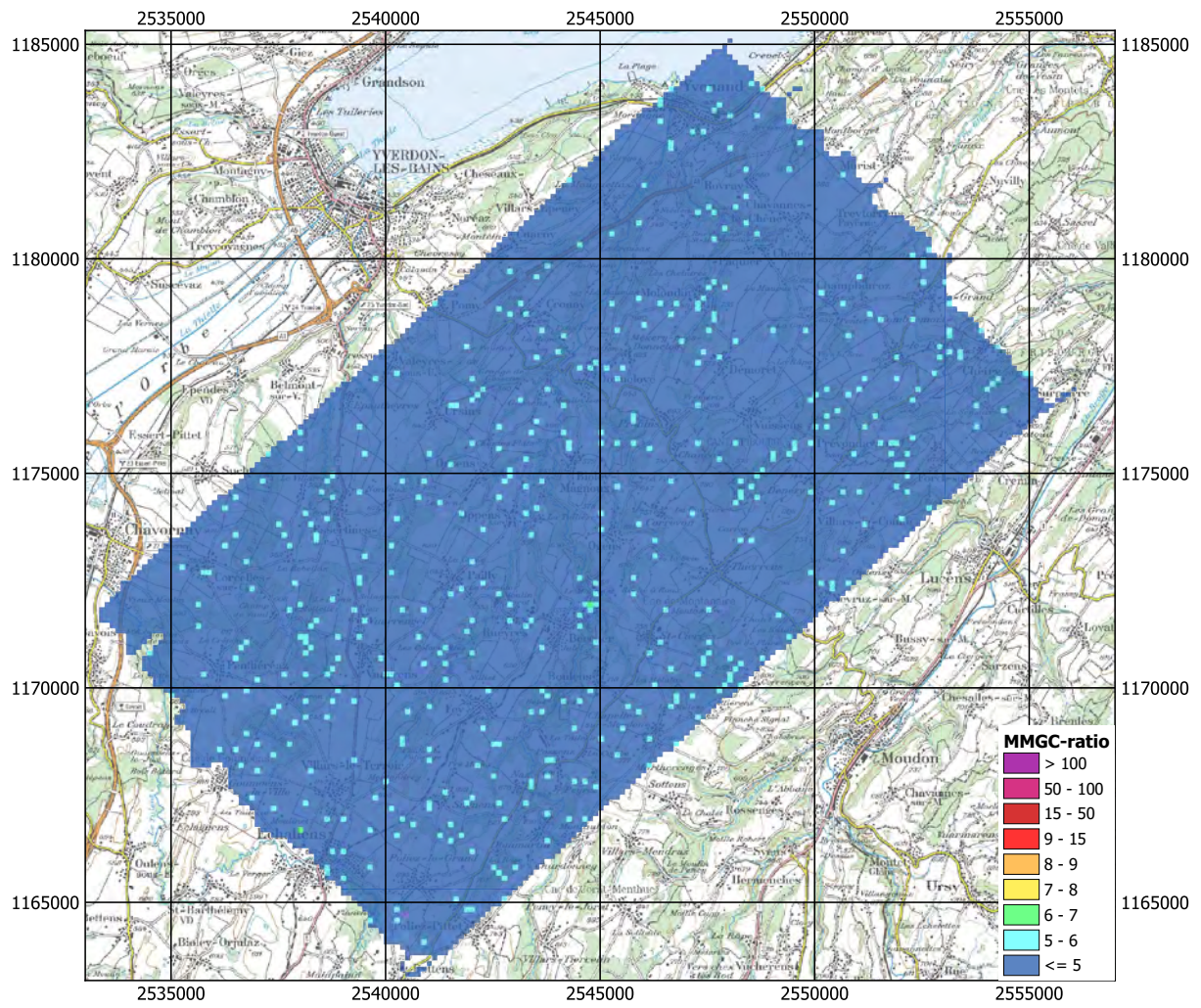


Figure 35: MMGC-ratio near Bercher. Geodaten©swisstopo.

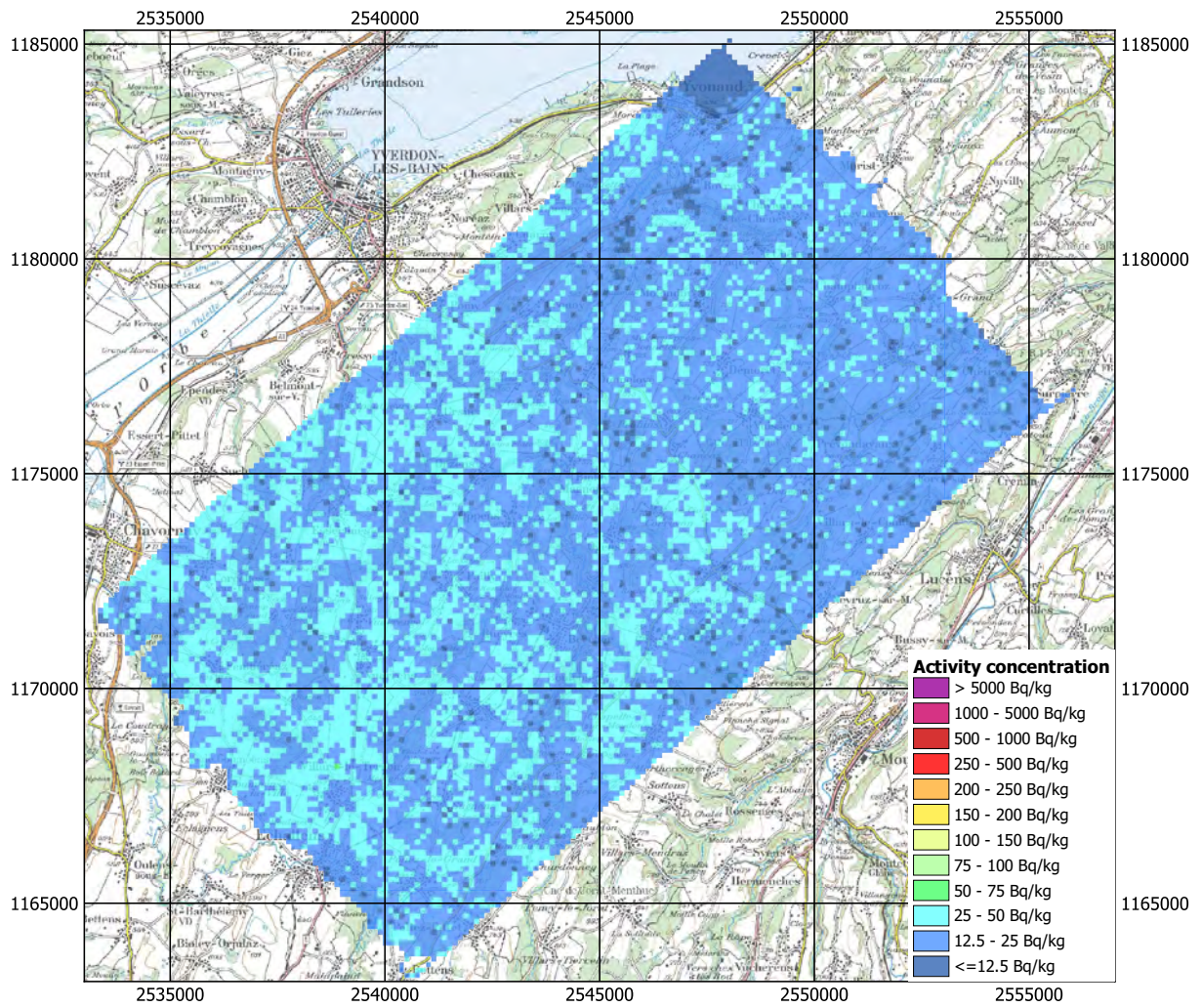


Figure 36:  $^{232}\text{Th}$  activity concentration near Bercher. Geodaten©swisstopo.

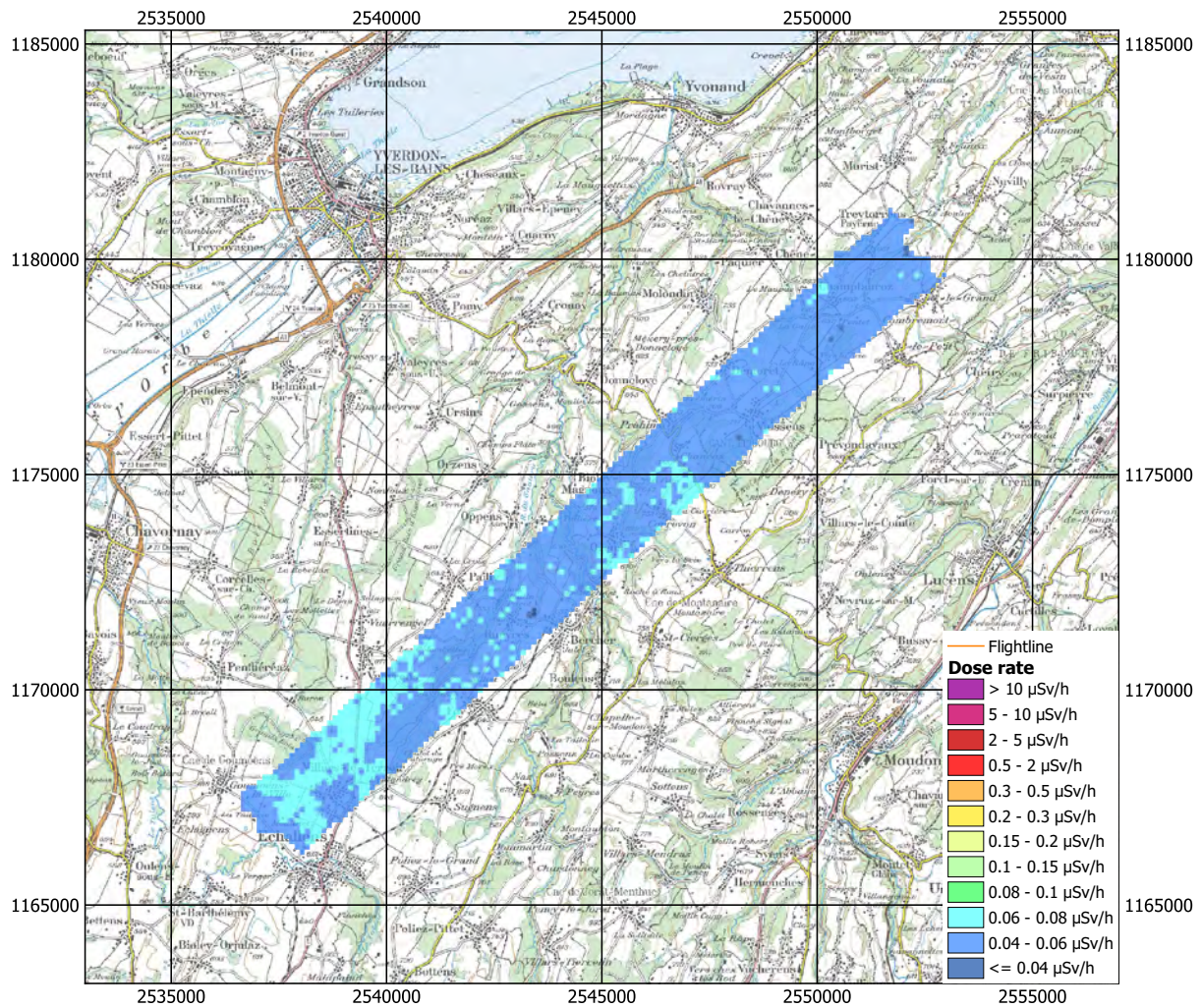


Figure 37: Terrestrial dose rate near Bercher measured on September 11<sup>th</sup>.  
Geodaten©swisstopo.

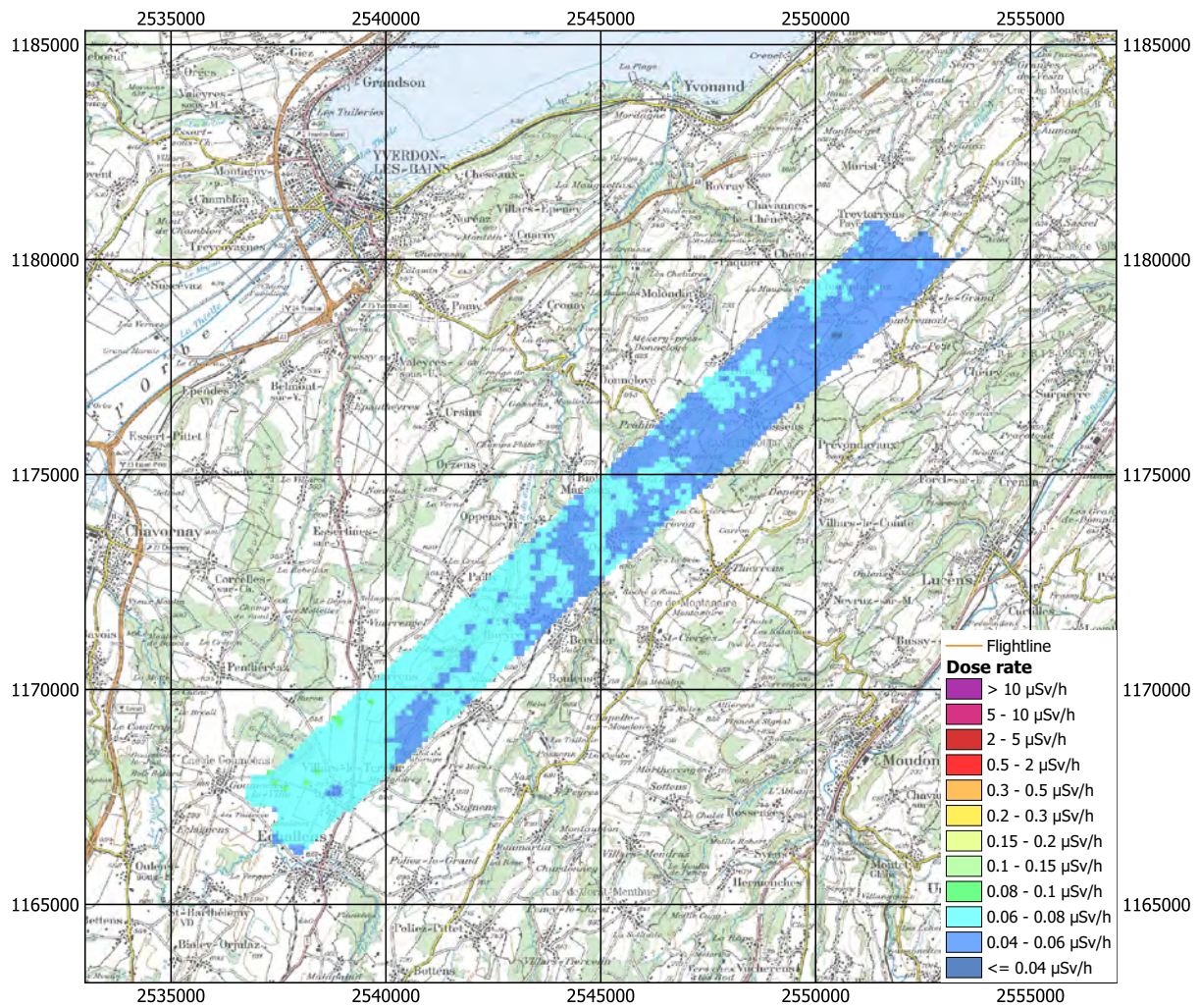


Figure 38: Terrestrial dose rate near Bercher measured on September 13<sup>th</sup>.  
Geodaten@swisstopo.

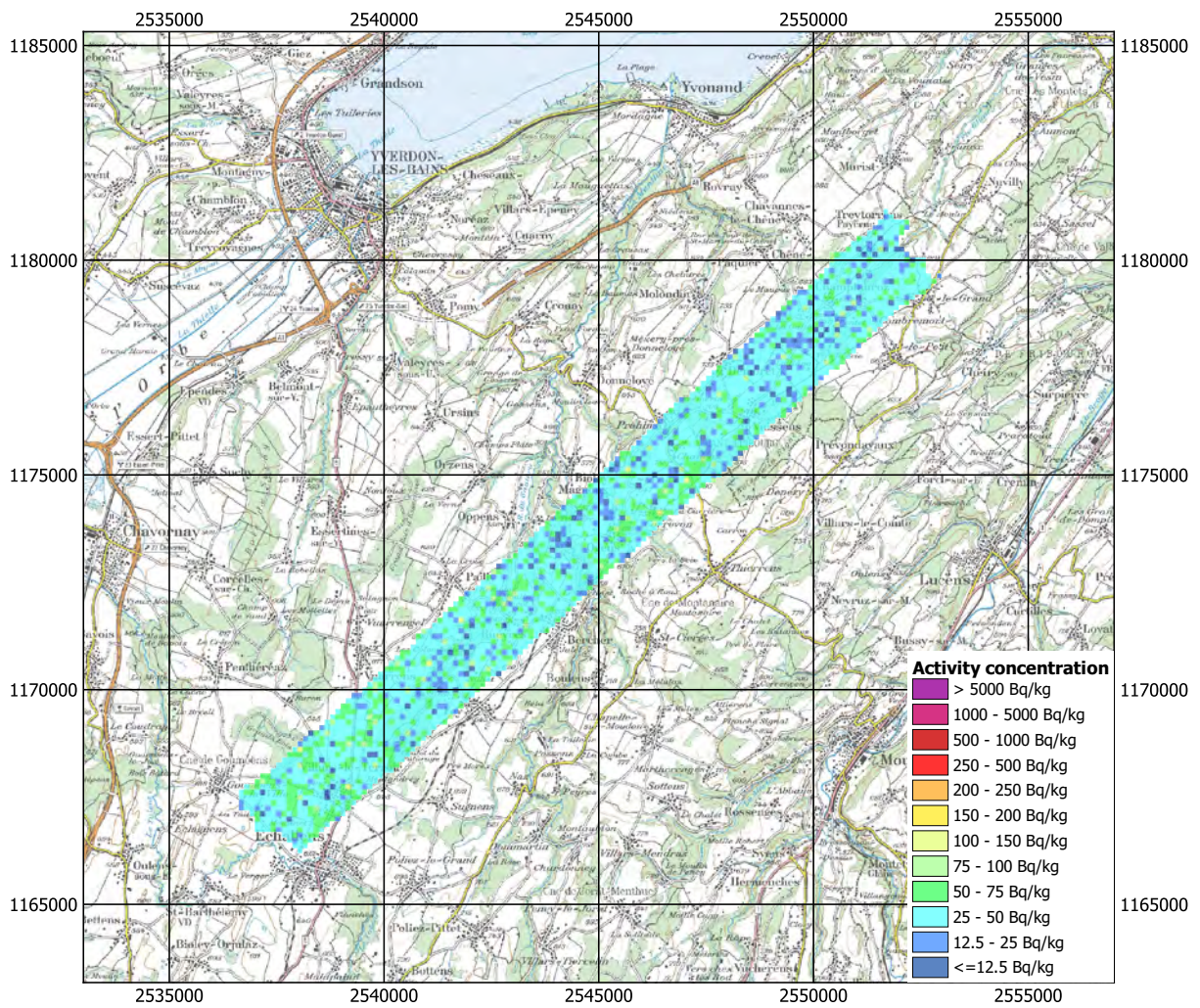


Figure 39:  $^{238}\text{U}$  activity concentration near Bercher measured on September 11<sup>th</sup>. Geodaten©swisstopo.

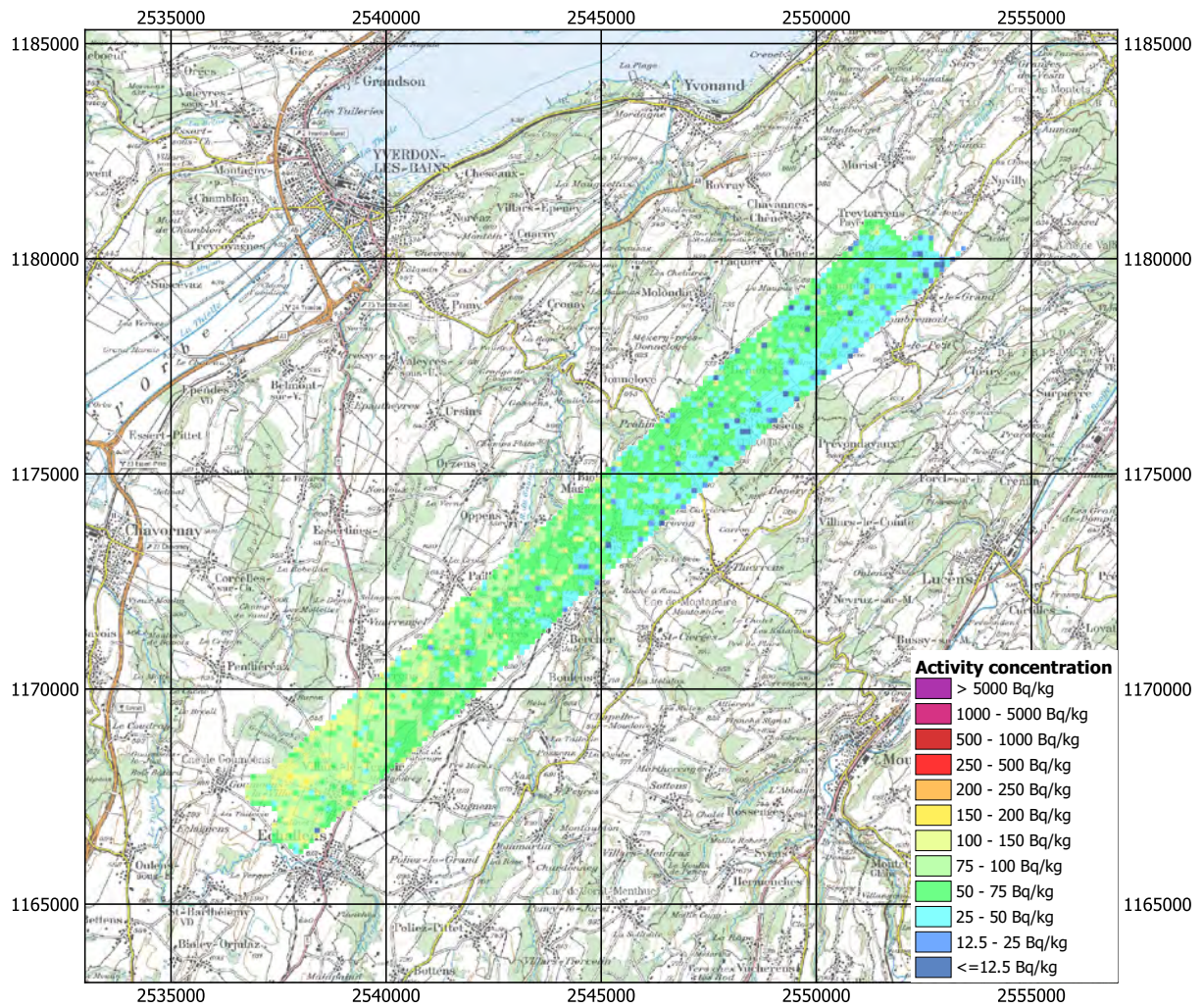


Figure 40:  $^{238}\text{U}$  activity concentration near Bercher measured on September 13<sup>th</sup>. Geodaten©swisstopo.



### 2.3.2 Chrüz

The Chrüz is a mountain located in the Canton of Graubünden with an elevation of 2195 m above sea level. The usual flight pattern covering an area with parallel flight lines would lead to frequent climbs and descents of the helicopter (Figure 41). During this exercise, the spiral flight pattern used by the German AGRS-teams, described in Butterweck et al. (2018), was adapted following terrain contour lines to reduce the frequency of flight altitude changes. In fact, following contour lines of the topography reduces the necessity for drastic flight altitude changes compared to the parallel line pattern normally used, but at the expense of being much more challenging for the pilots. The map of total dose rate (Figure 42) shows slightly higher values due to the increased cosmic dose rate associated with the elevated ground level of the area. Subtracting the altitude dependent cosmic dose rate yields the terrestrial component of the dose rate (Figure 43), which is largely uniform over the measured area. A spot with slightly elevated terrestrial dose rate can be observed over the westernmost loop of the flight lines. The map of the MMGC-ratio (Figure 44) does not give an indication of the presence of man-made radionuclides at this point. The increase of terrestrial dose rate is associated with elevated levels of the natural radionuclides  $^{40}\text{K}$  (Figure 46) and  $^{232}\text{Th}$  (Figure 45).

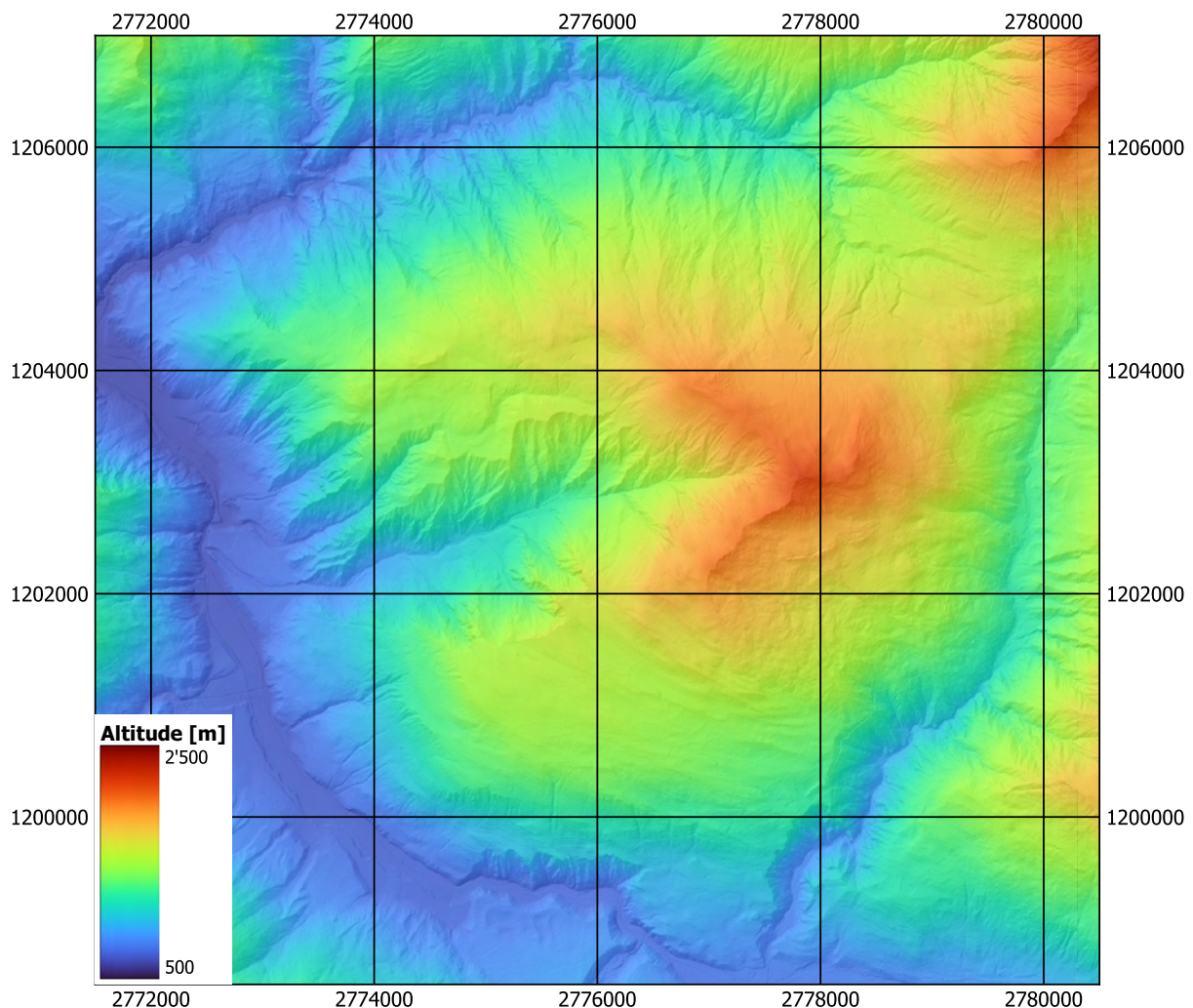


Figure 41: Color scale altitude map superposed over a relief of the Chrüz region.  
Geodaten©swisstopo.

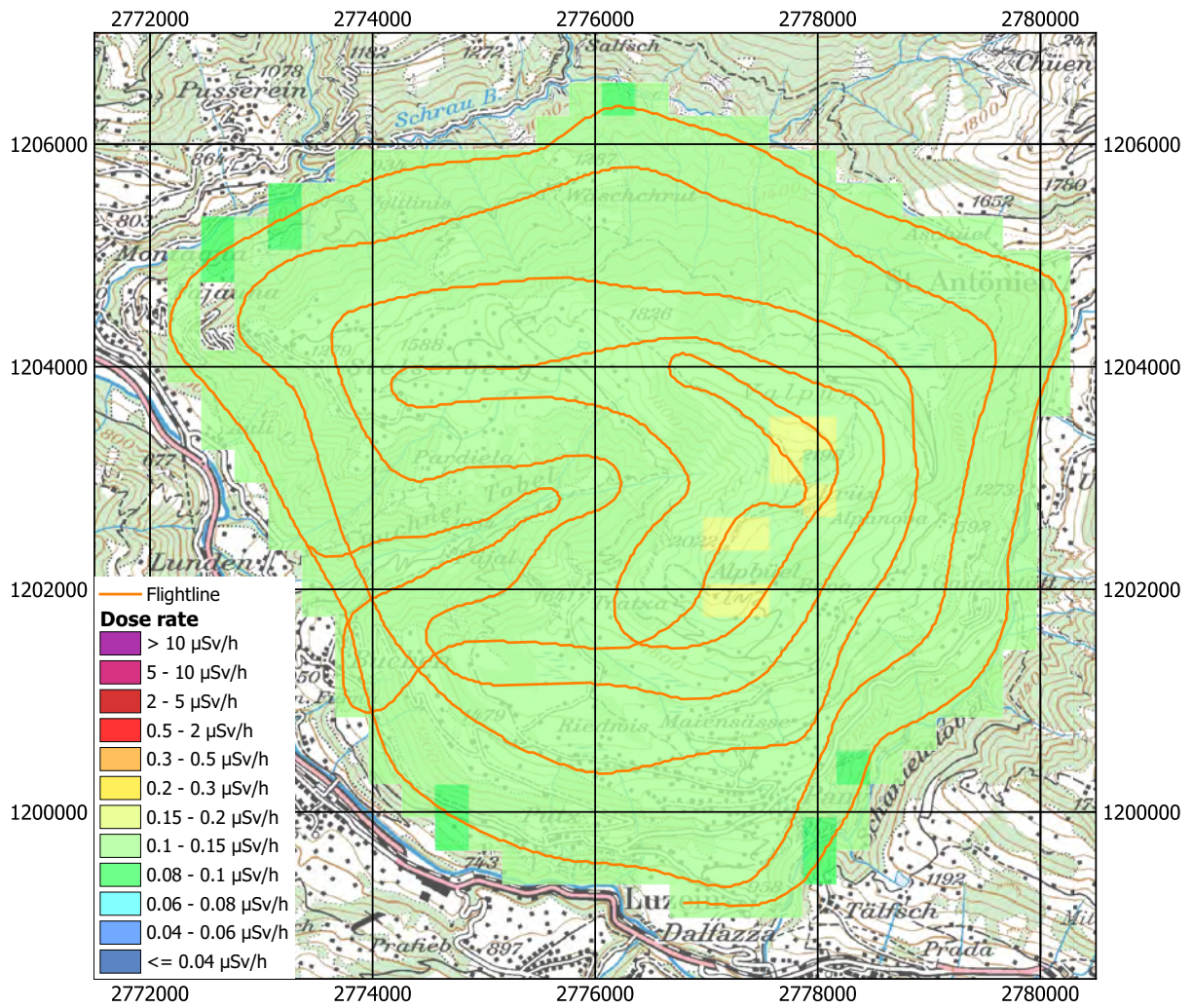


Figure 42: Dose rate near the Chrüz . Geodaten©swisstopo.

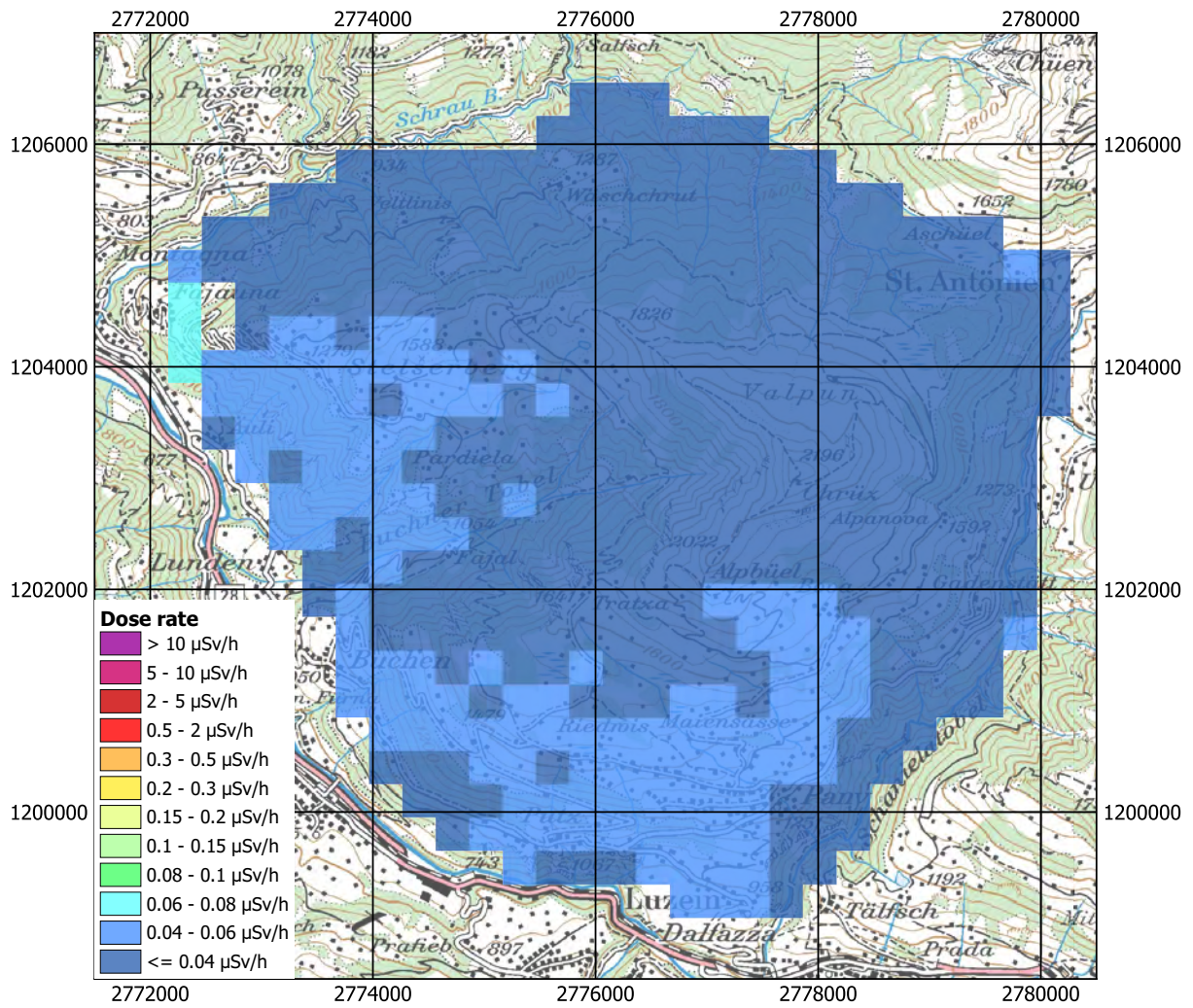


Figure 43: Terrestrial dose rate near the Chrüz . Geodaten©swisstopo.

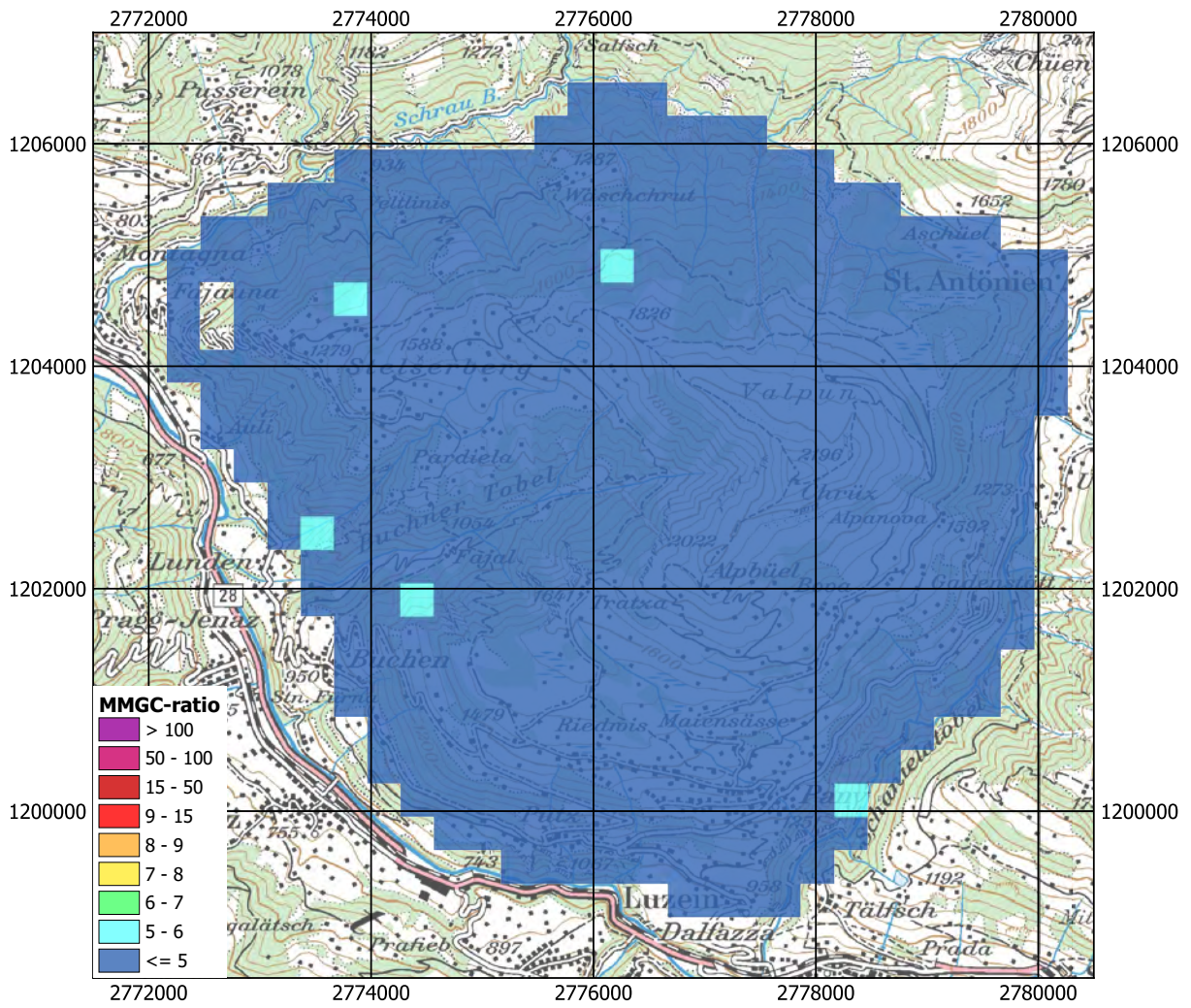


Figure 44: MMGC-ratio near the Chrüz. Geodaten©swisstopo.

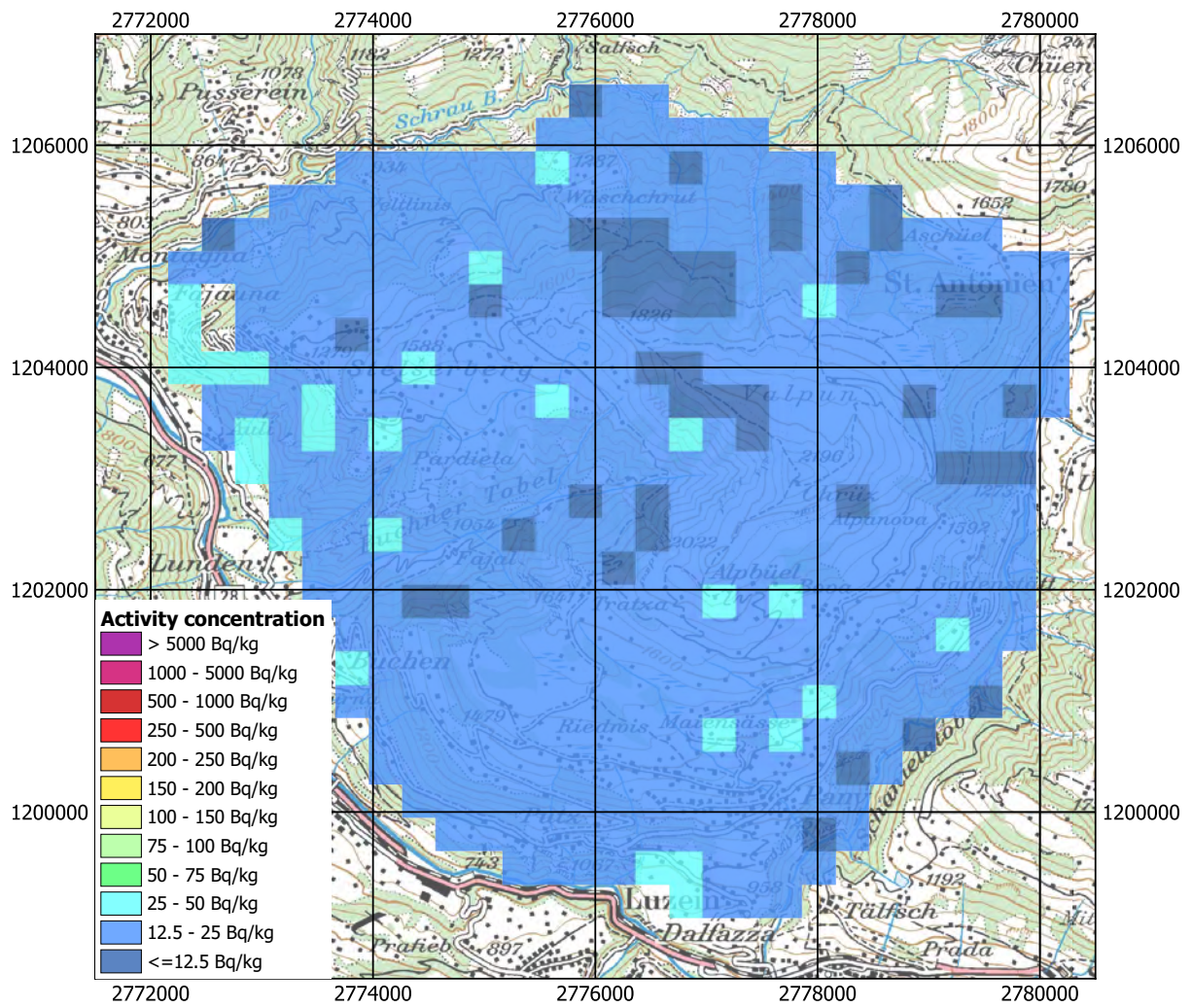


Figure 45:  $^{232}\text{Th}$  activity concentration near the Chrüz. Geodaten©swisstopo.

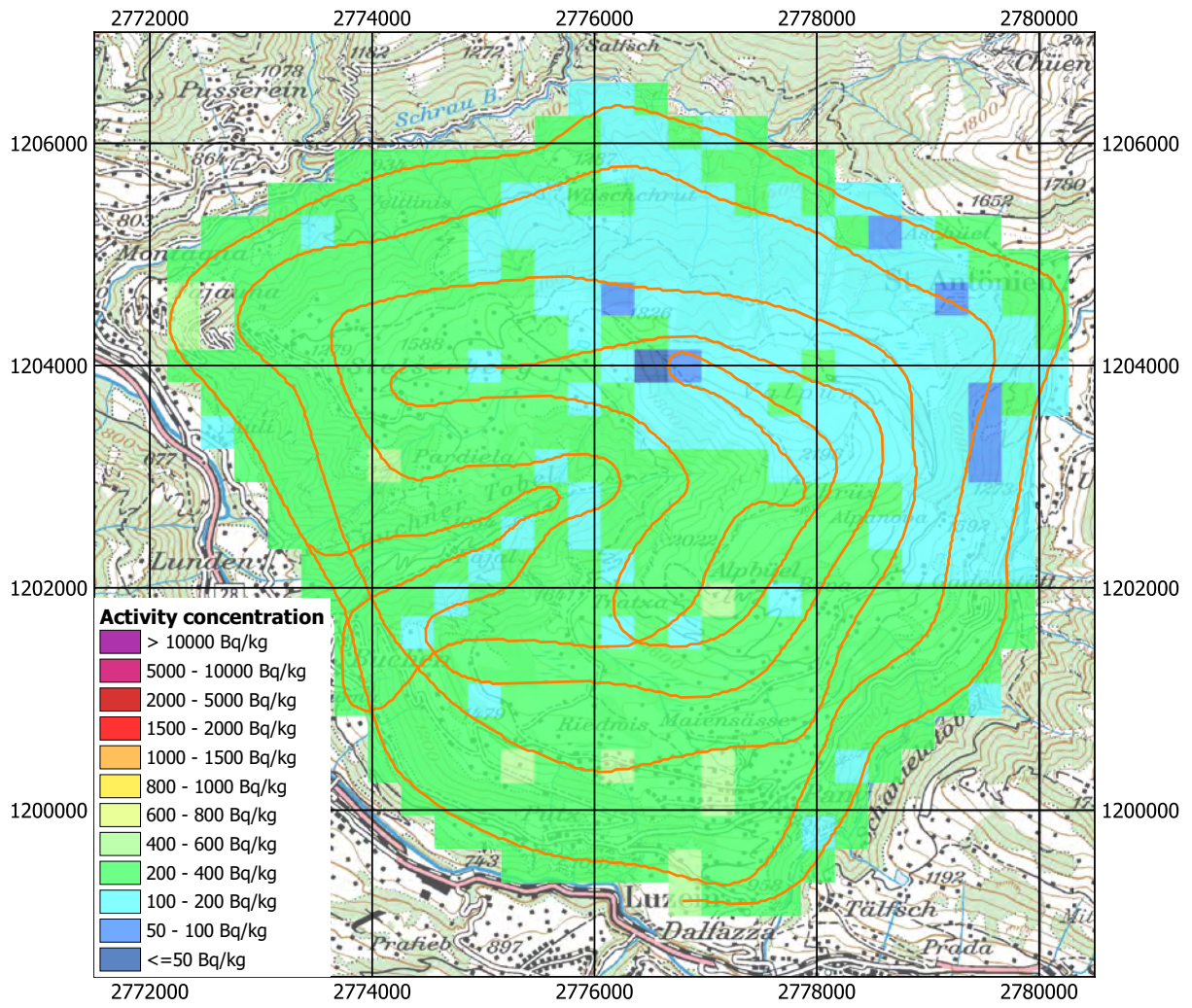


Figure 46:  $^{40}\text{K}$  activity concentration near the Chrüz. Geodaten©swisstopo.

### 2.3.3 Estavayer-le-Lac

The measurement area near Estavayer-le-Lac is located on the southern shore of Lake Neuchâtel. The dose rate map (Figure 47) and the map of the natural radionuclide  $^{232}\text{Th}$  (Figure 49) show clearly the attenuation of terrestrial photons passing through the water of the lake. The map of the MMGC-ratio (Figure 48) depicts some elevated values at the shore of the lake. This is a well-known artefact of the MMGC-ratio caused by unusual low readings of high energy photons from natural radionuclides due to the water attenuation.

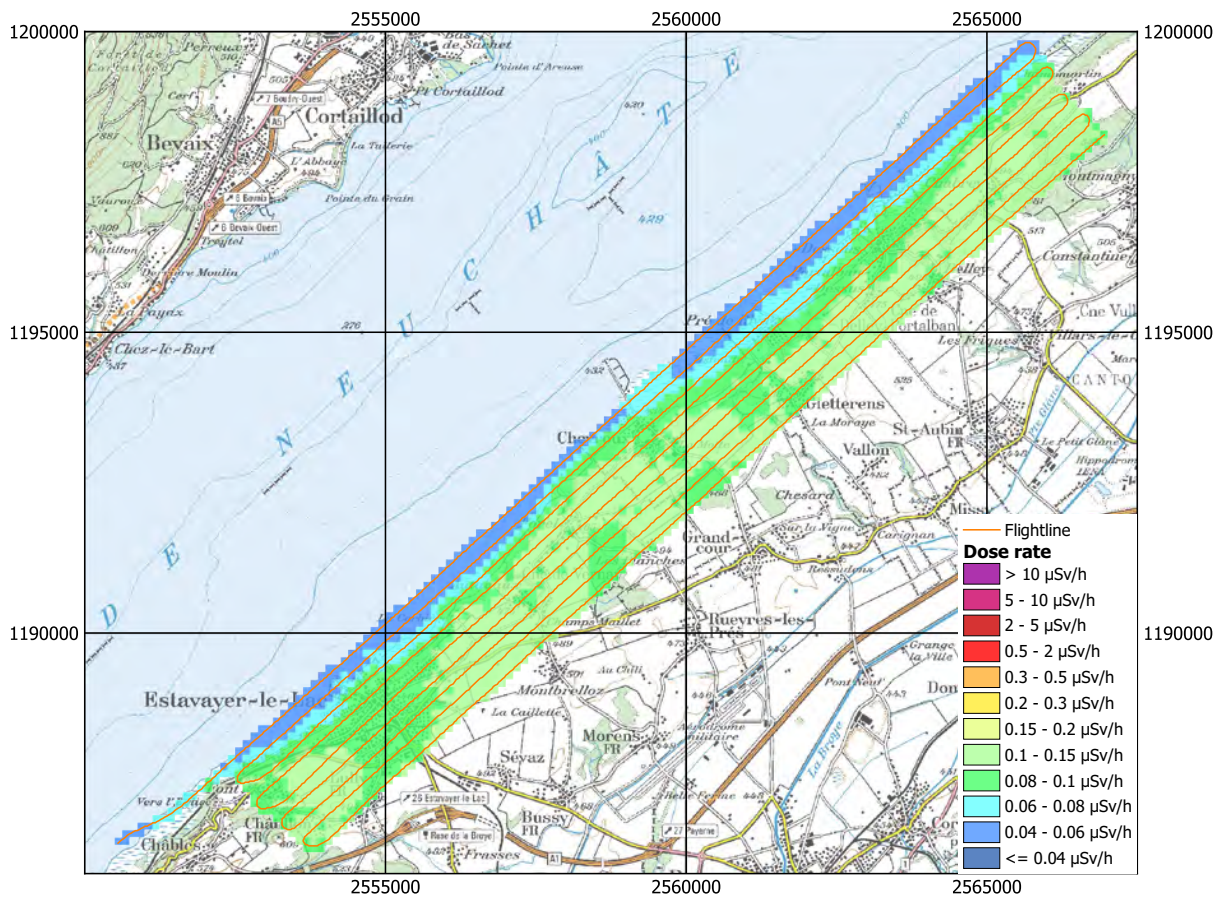


Figure 47: Dose rate near Estavayer-le-Lac. Geodaten©swisstopo.

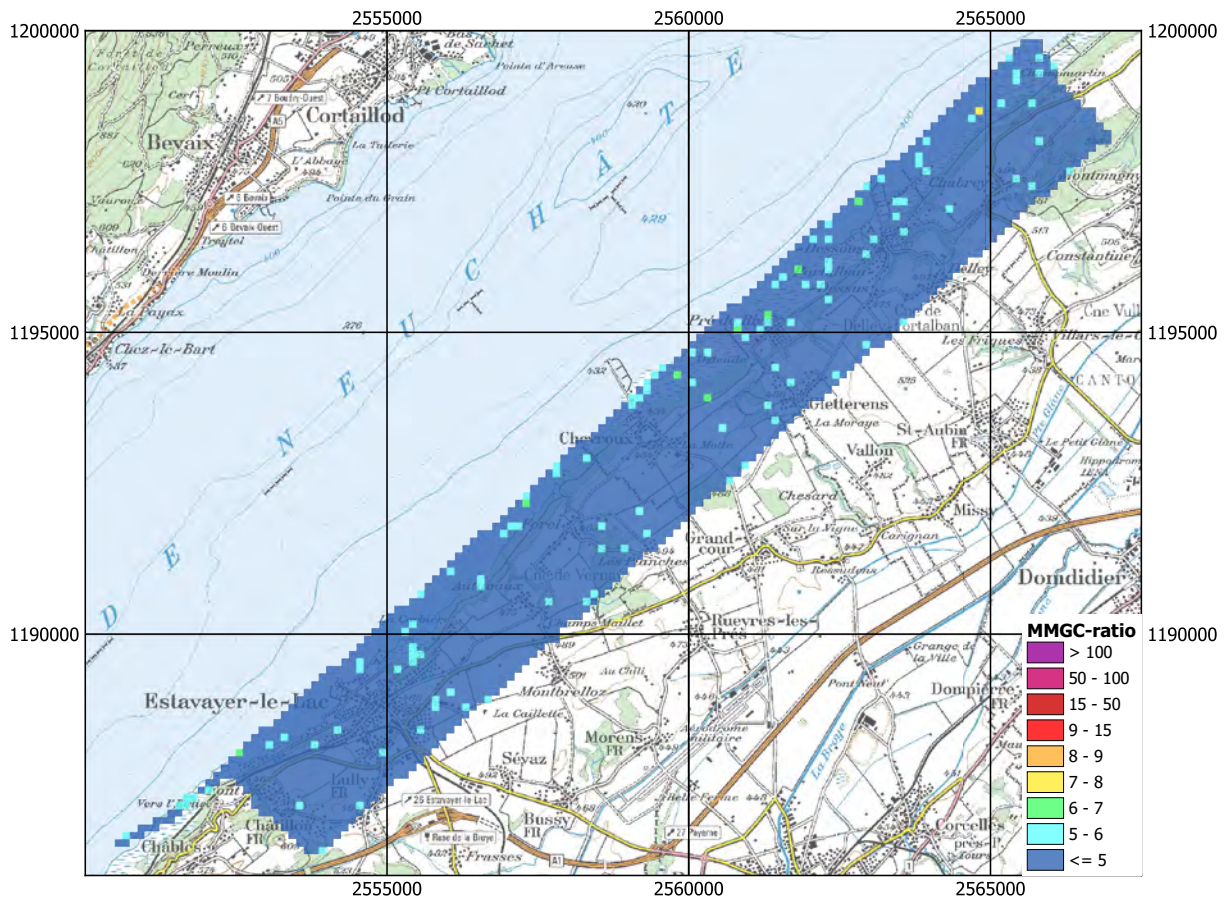


Figure 48: MMGC-ratio near Estavayer-le-Lac. Geodaten©swisstopo.



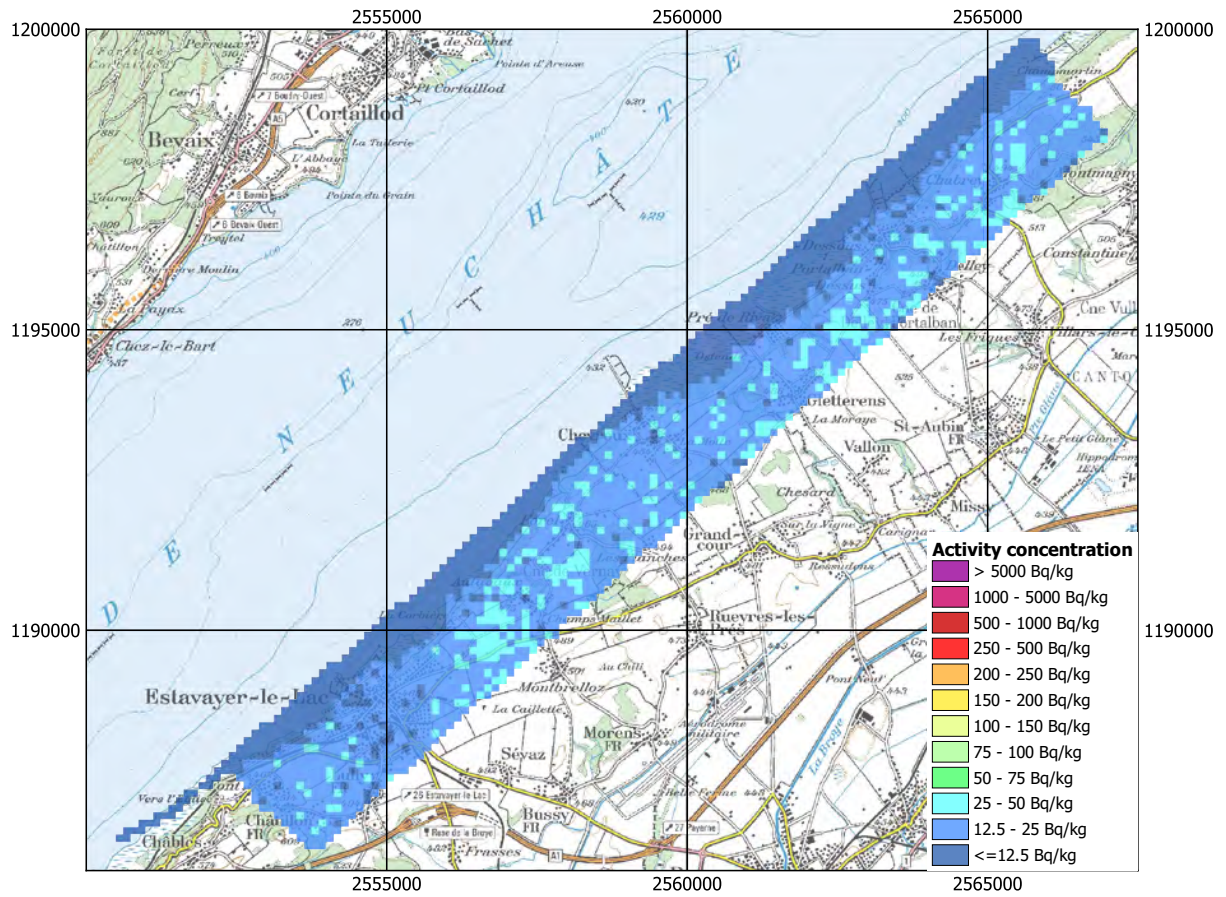


Figure 49:  $^{232}\text{Th}$  activity concentration near Estavayer-le-Lac. Geodaten©swisstopo.

### 2.3.4 Klosters

Klosters is located in the Canton of Graubünden in eastern Switzerland. All maps of the measurements (Figures 50, 51 and 52) display typical values for the natural radiation background. The dose rate, oscillating in the measured area between 0.1 and 0.2 [ $\mu\text{Sv/h}$ ], is attributable to higher exposure to cosmic radiation, associated with the elevated ground level of the area (1150 m above sea level).

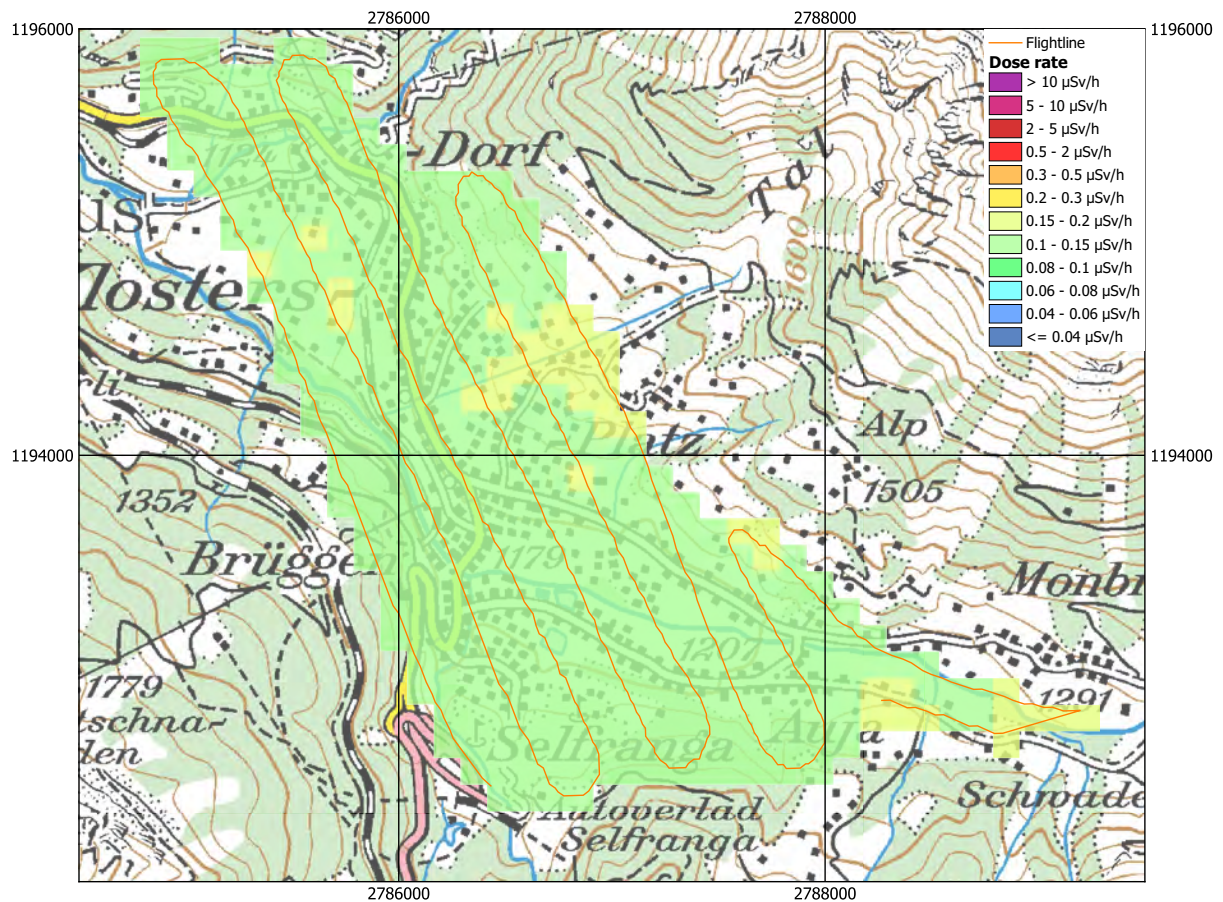


Figure 50: Dose rate near Klosters. Geodaten©swisstopo.

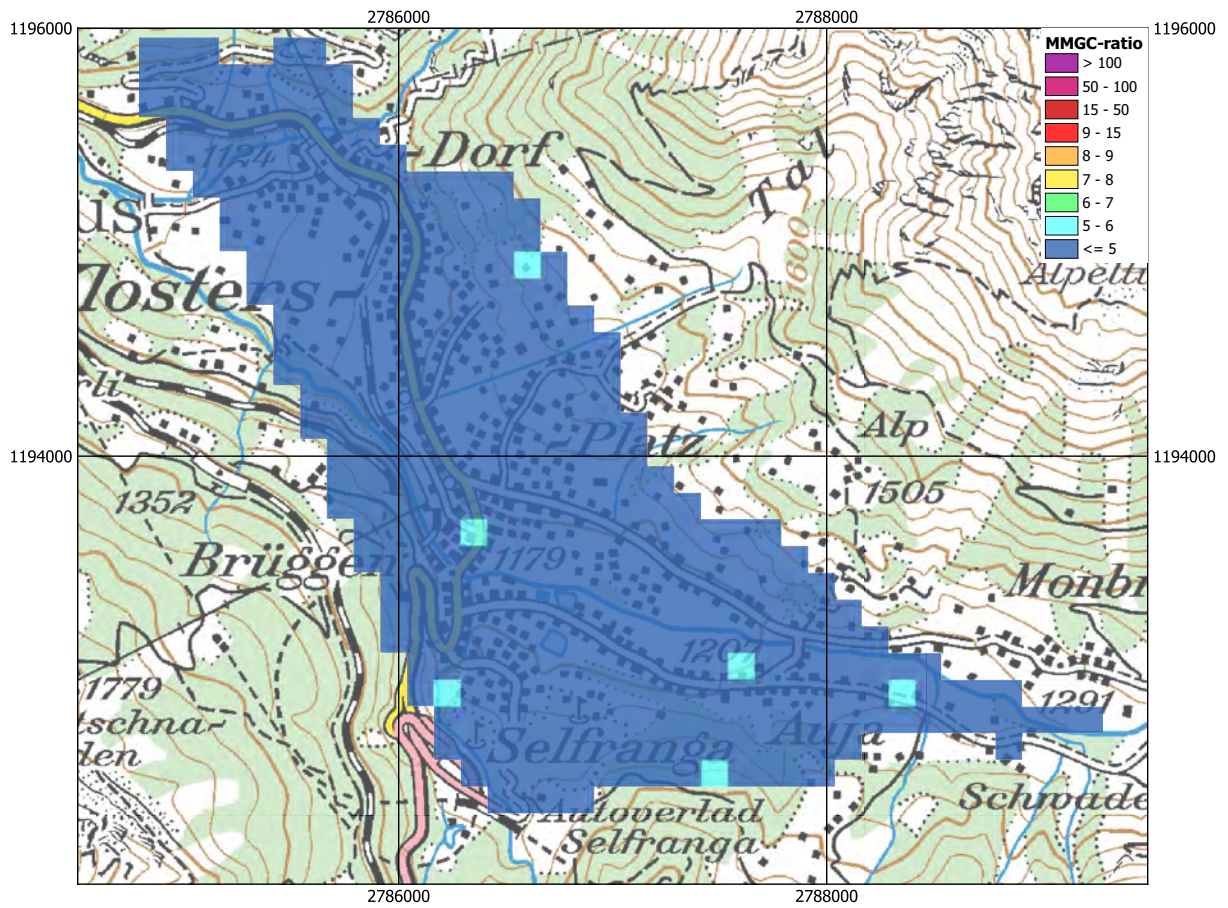


Figure 51: MMGC-ratio near Klosters. Geodaten©swisstopo.

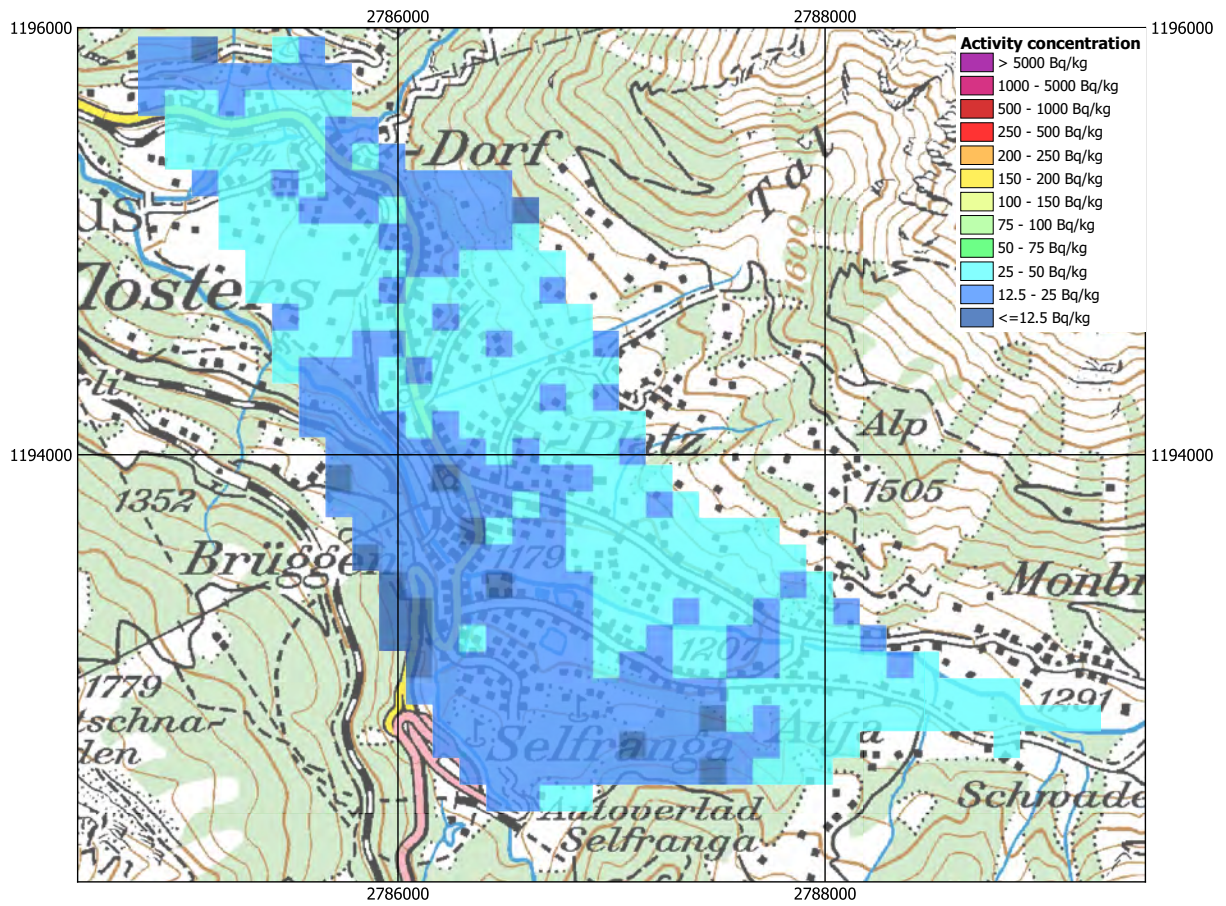


Figure 52:  $^{232}\text{Th}$  activity concentration near Klosters. Geodaten©swisstopo.

### **2.3.5 Landquart**

Landquart is located in the Canton of Graubünden in eastern Switzerland. As in the region around Klosters (Section 2.3.4), typical values for the natural radiation environment were measured around Landquart (53, 54 and 55).

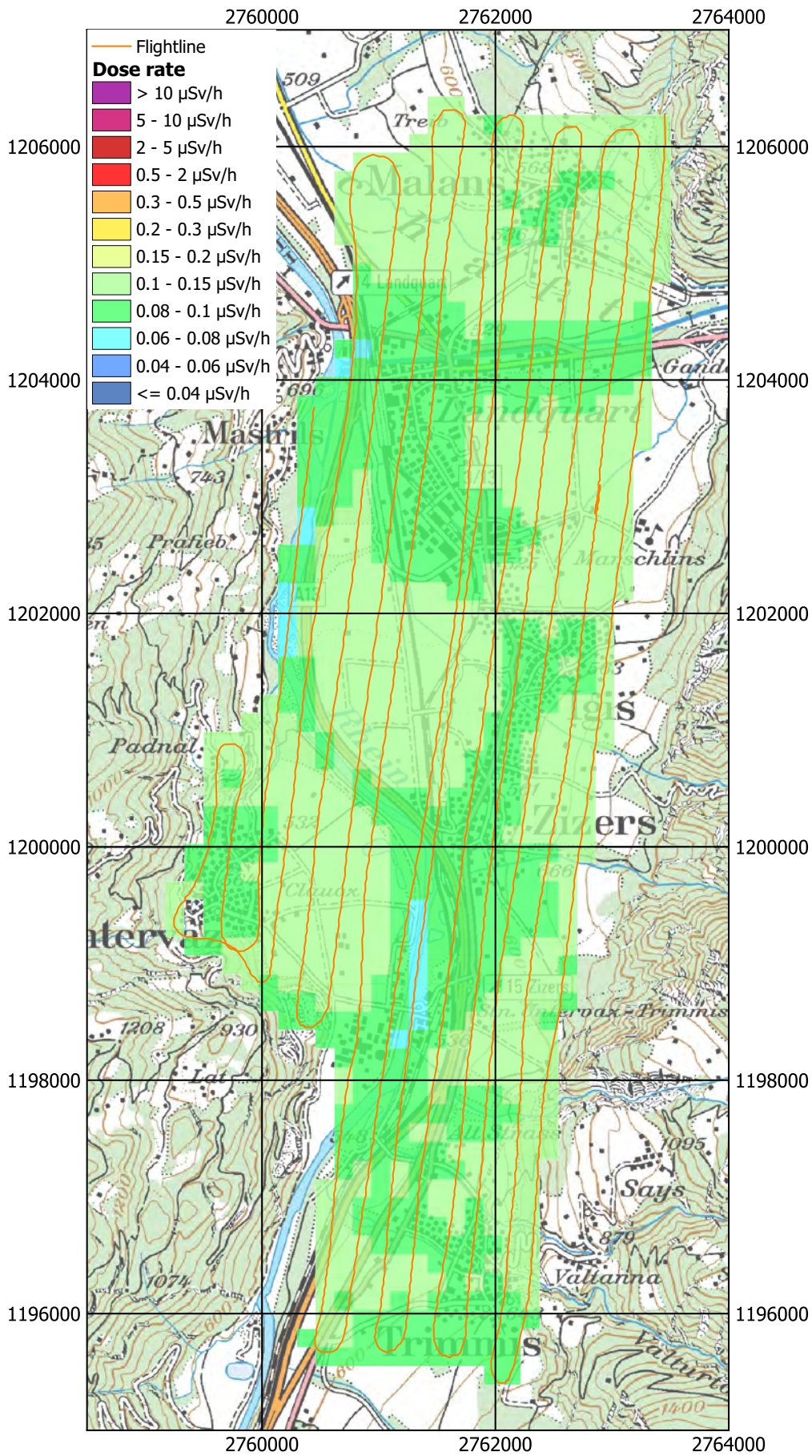


Figure 53: Dose rate near Landquart. Geodaten©swisstopo.

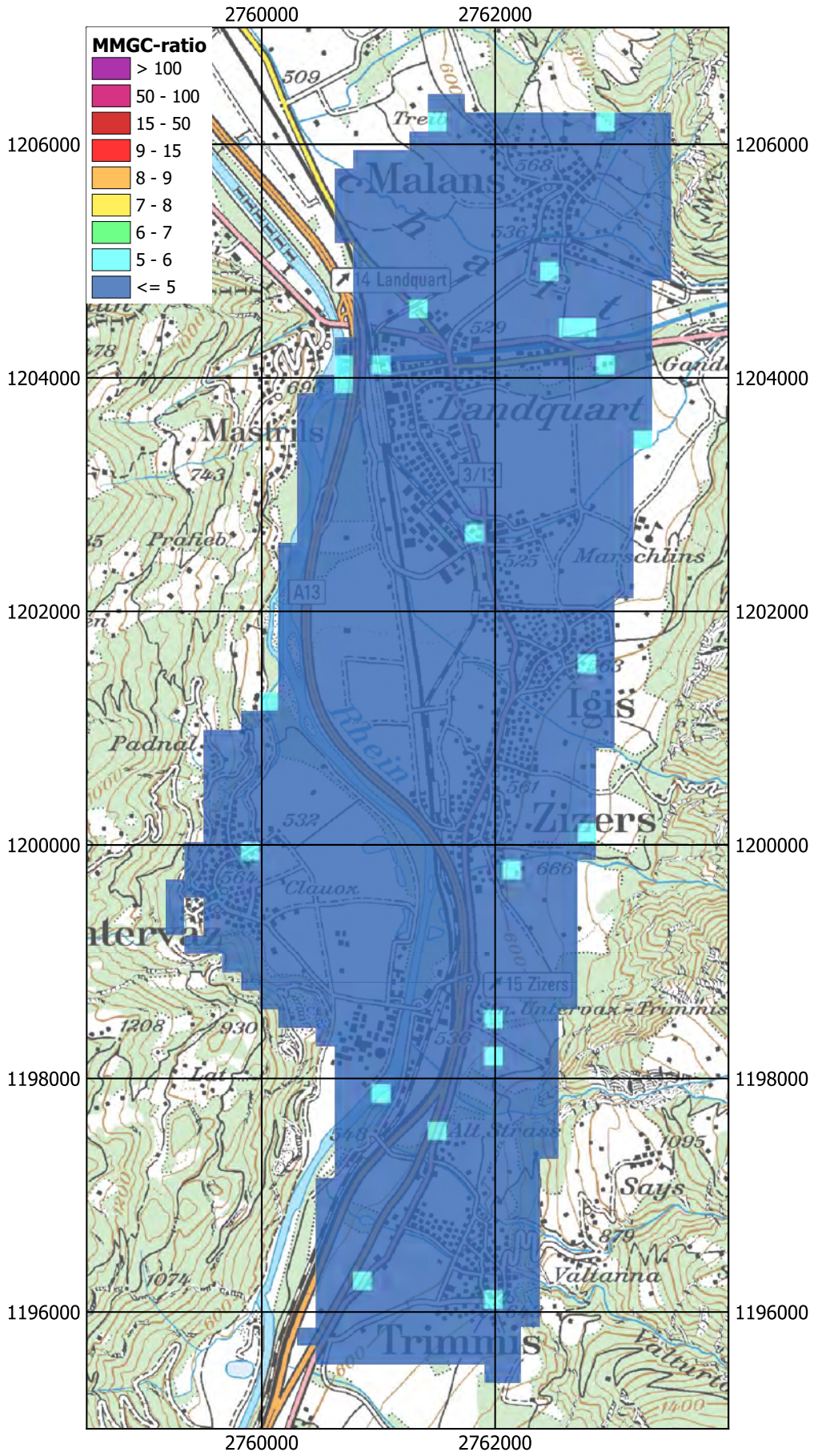


Figure 54: MMGC-ratio near Landquart. Geodaten©swisstopo.

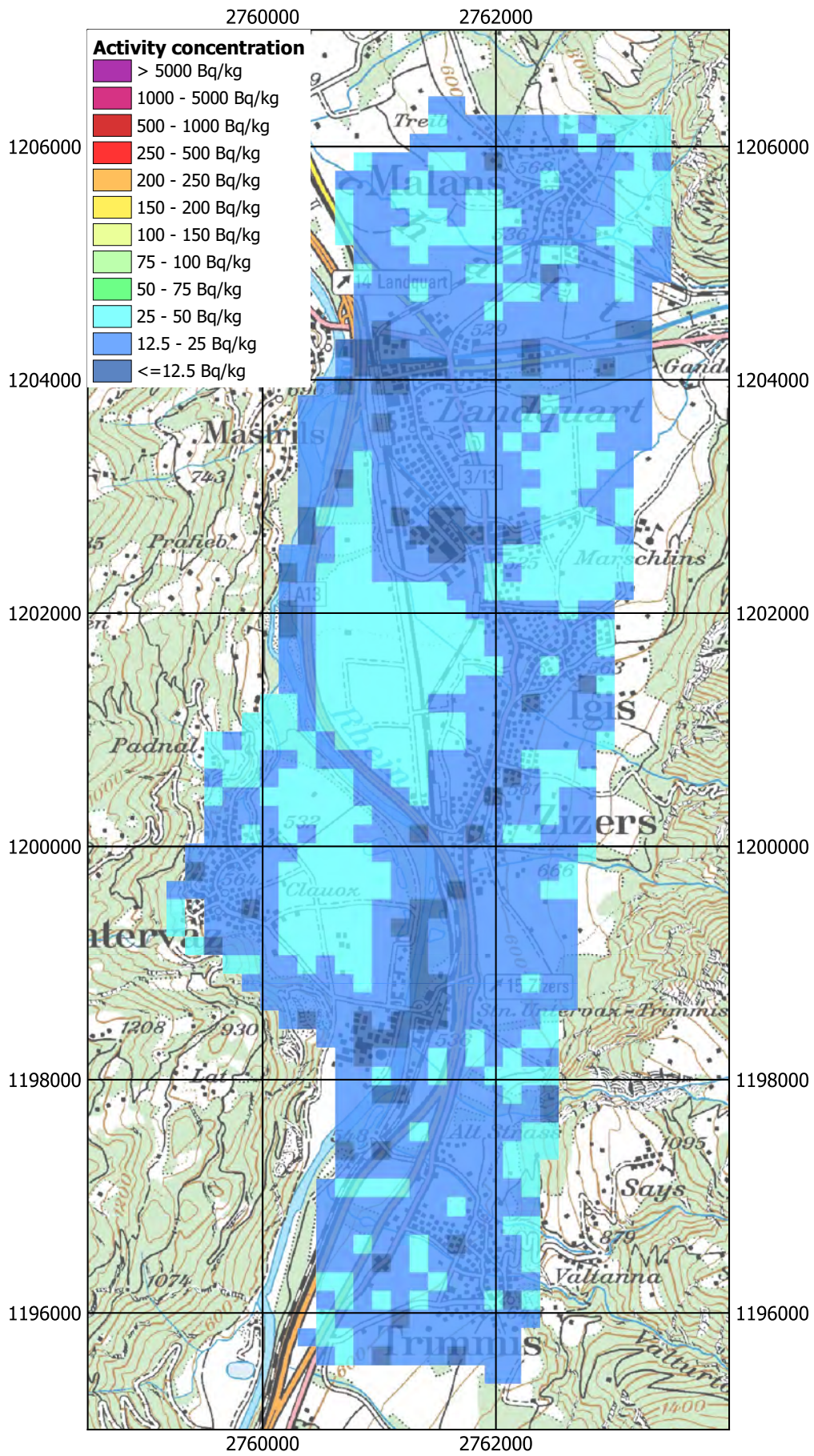
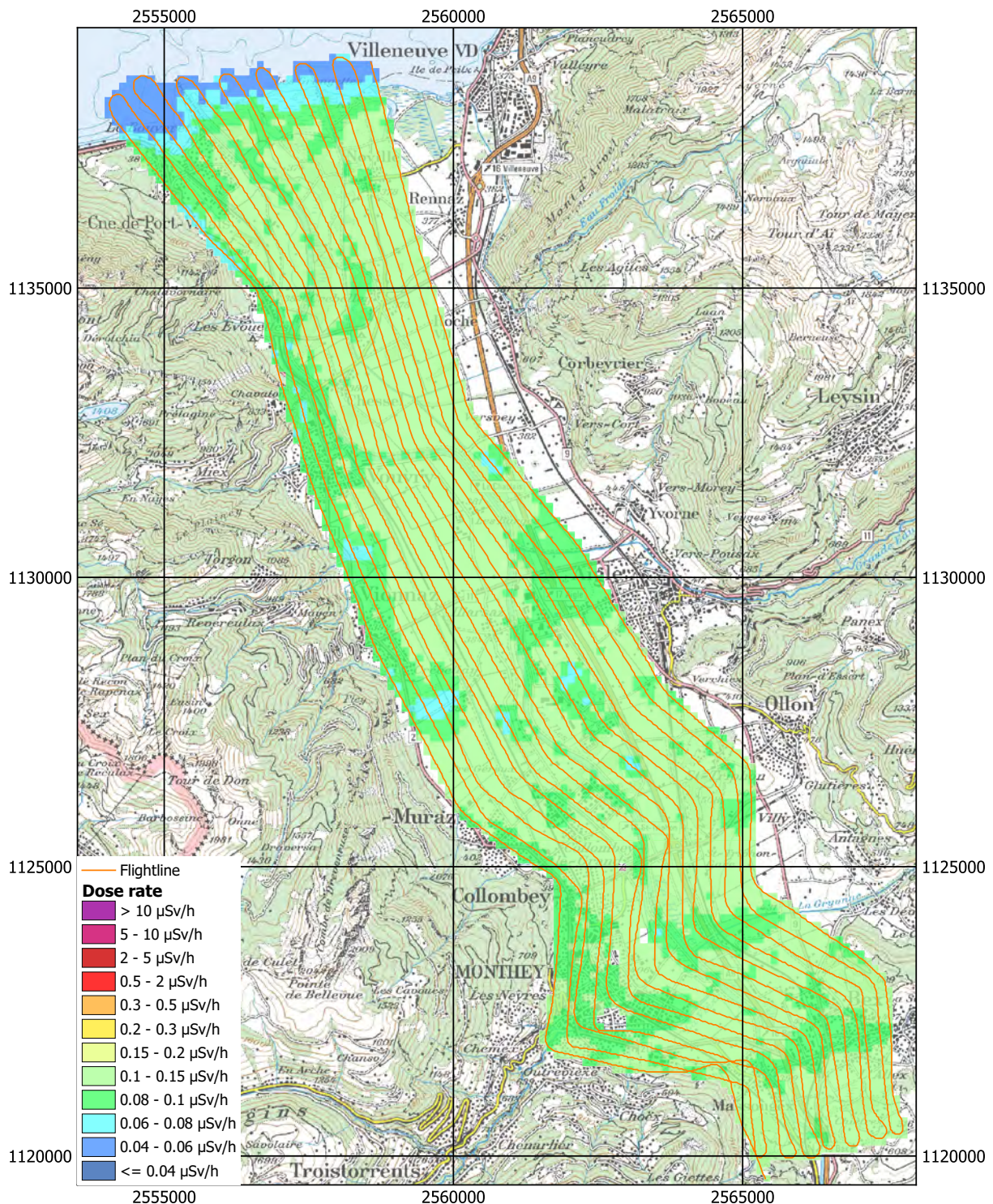


Figure 55:  $^{232}\text{Th}$  activity concentration near Landquart. Geodaten©swisstopo.



### 2.3.6 Monthey

Monthey is located to the south-east of Lake Geneva in the Canton Valais in southern Switzerland. The maps of dose rate (Figure 56) and the natural radionuclide  $^{232}\text{Th}$  (Figure 58) show typical background values and the attenuation of photons passing through the water layer of Lake Geneva. As observed already in the measurement region around Estavayer-le-Lac (Section 2.3.3), the MMGC-ratio (Figure 57) is prone to artefacts in the areas measuring these attenuated photon emissions.



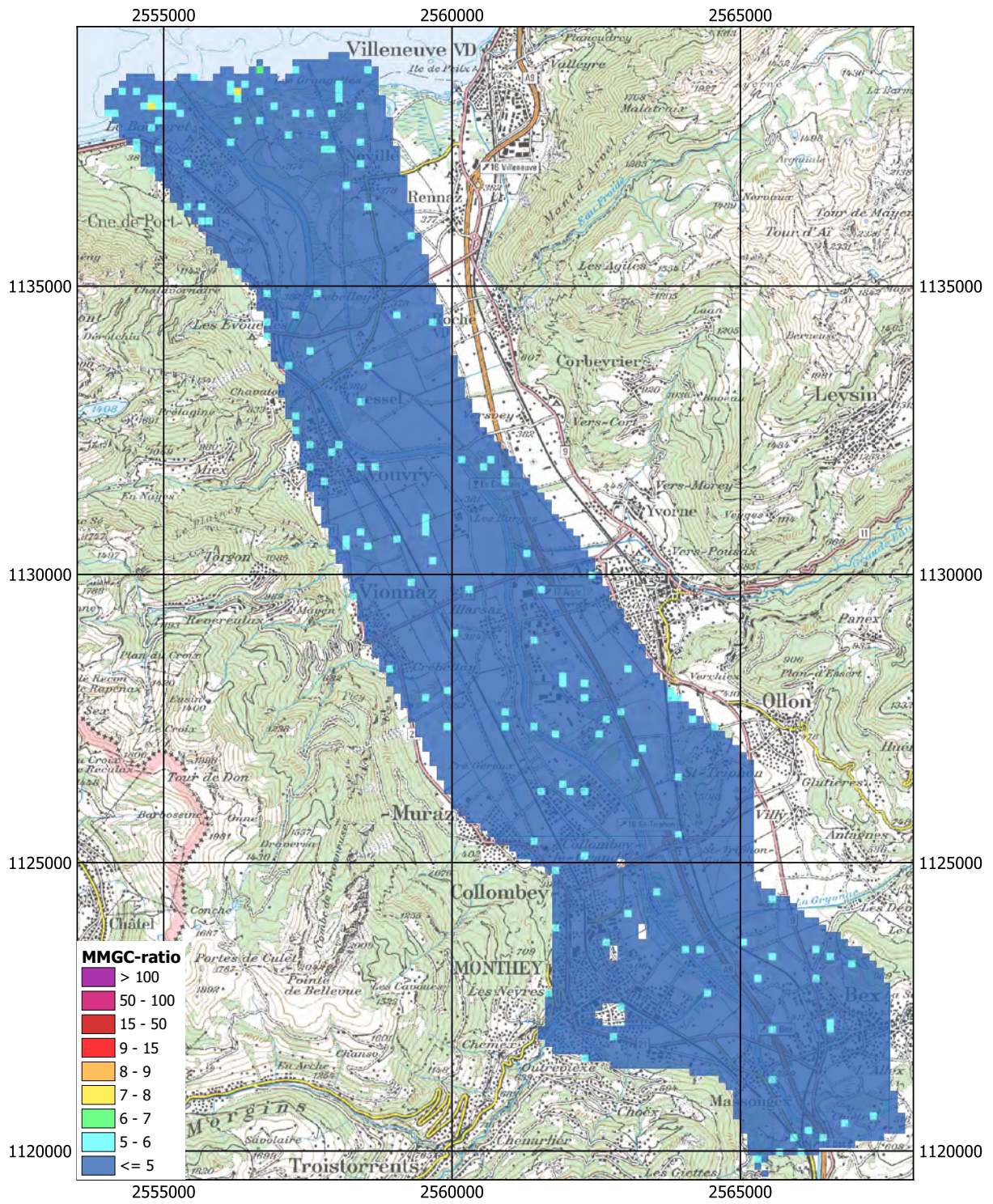


Figure 57: MMGC-ratio near Monthey. Geodaten©swisstopo.

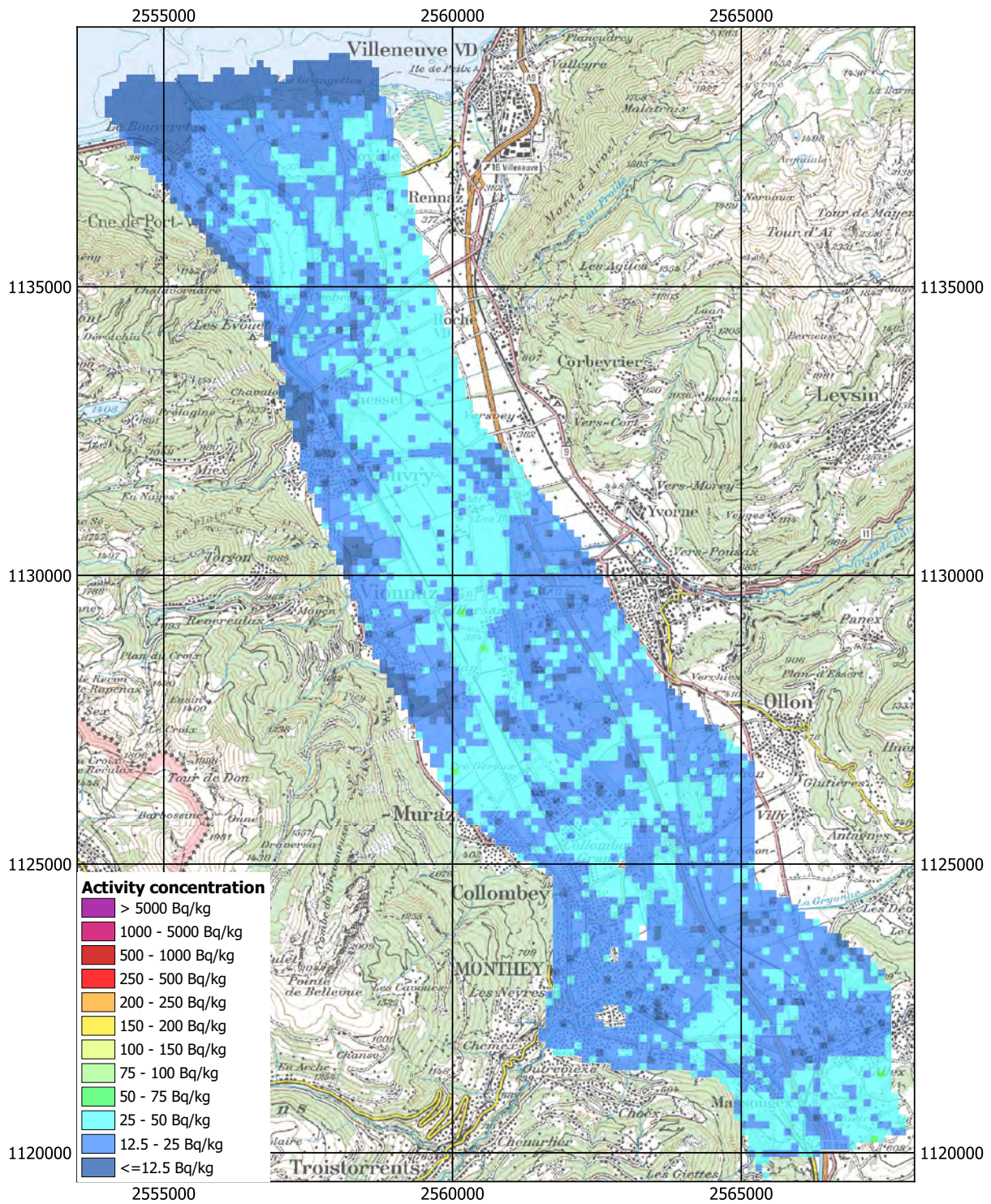


Figure 58:  $^{232}\text{Th}$  activity concentration near Monthey. Geodaten©swisstopo.

### 2.3.7 Noréaz

Noréaz is located to the south-east of Lake Neuchâtel in western Switzerland. All maps of the measured quantities (Figures 59, 60 and 61) display values expected for a natural radiation background.

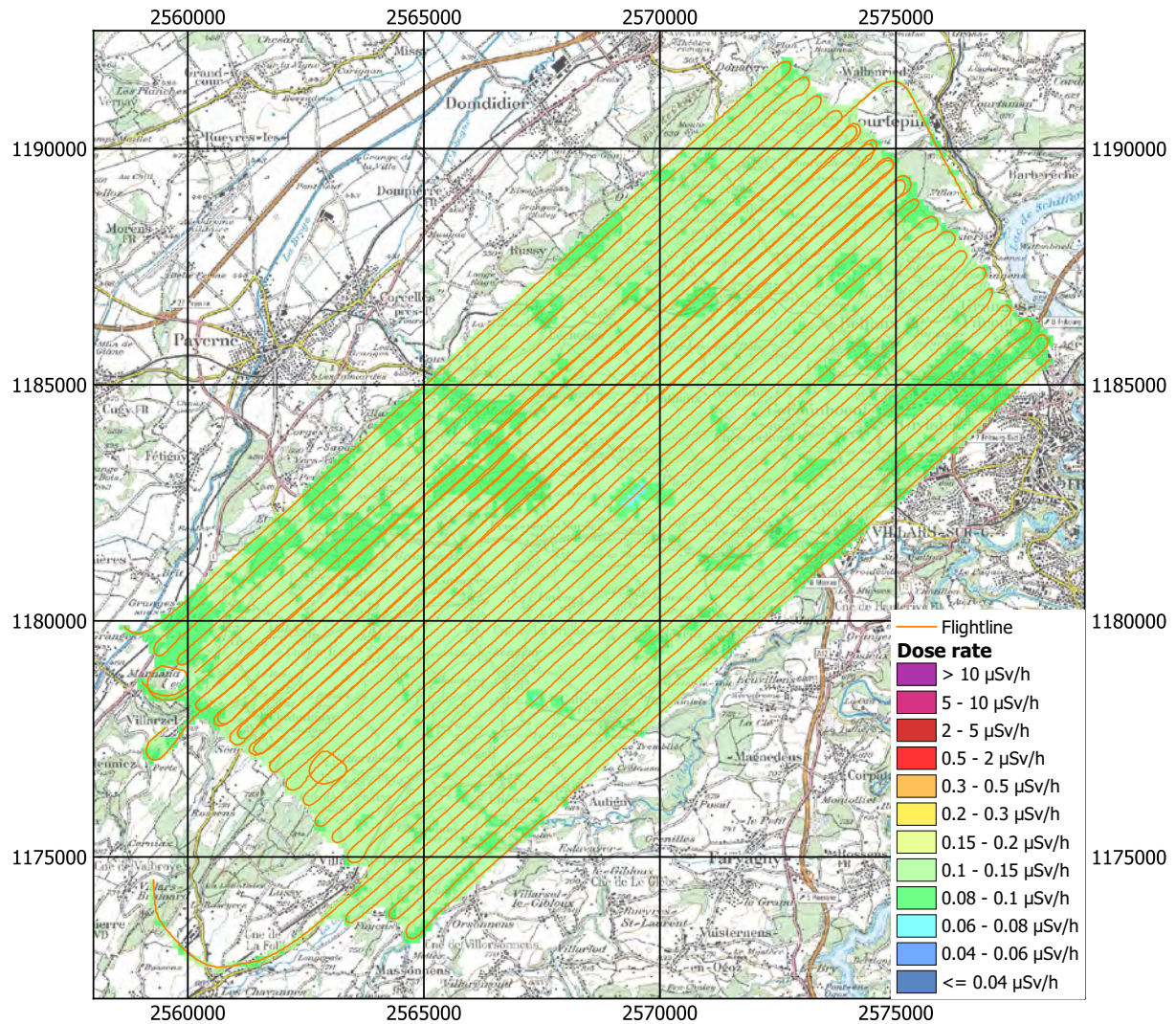


Figure 59: Dose rate near Noréaz. Geodaten©swisstopo.

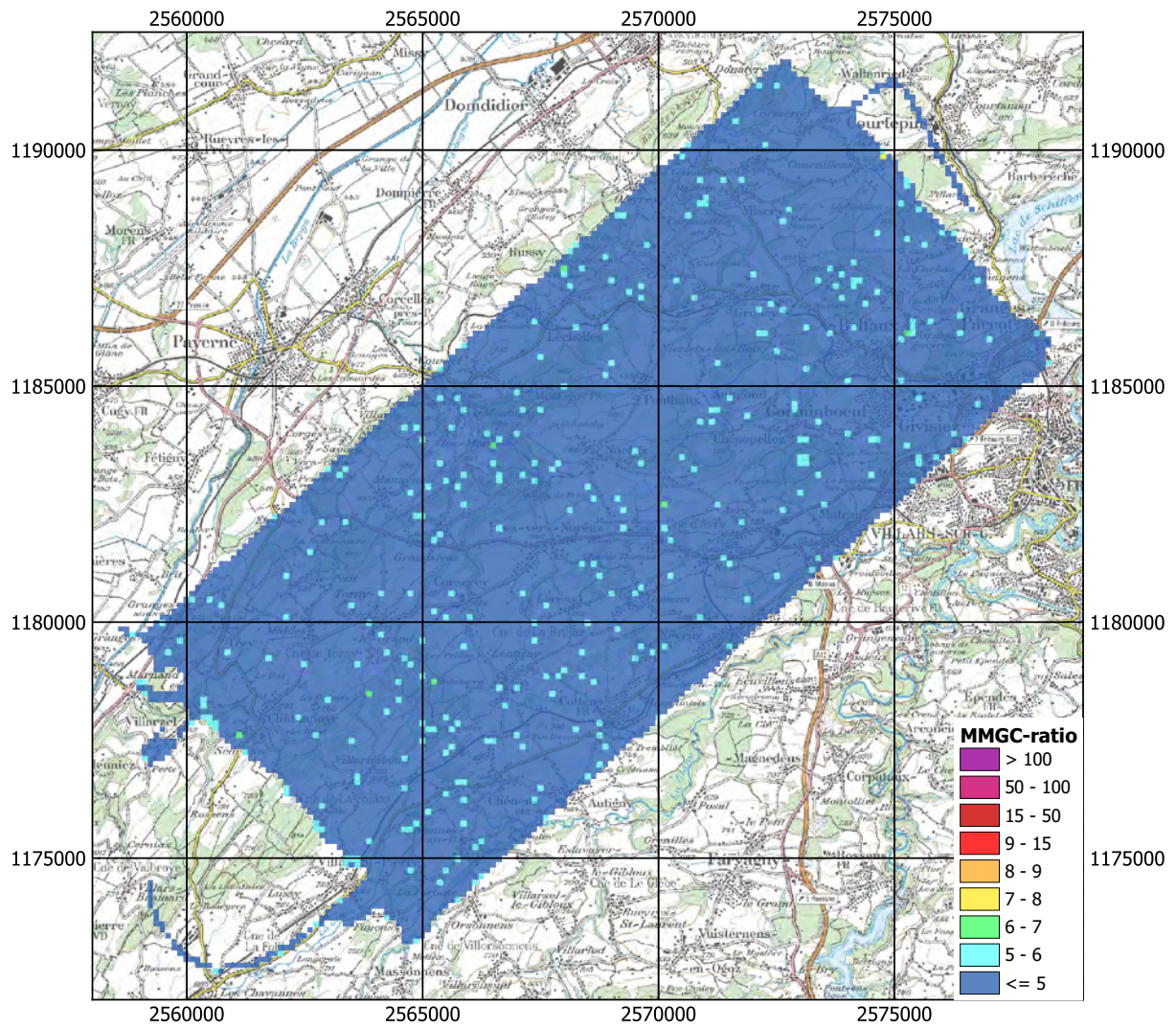


Figure 60: MMGC-ratio near Noréaz. Geodaten©swisstopo.

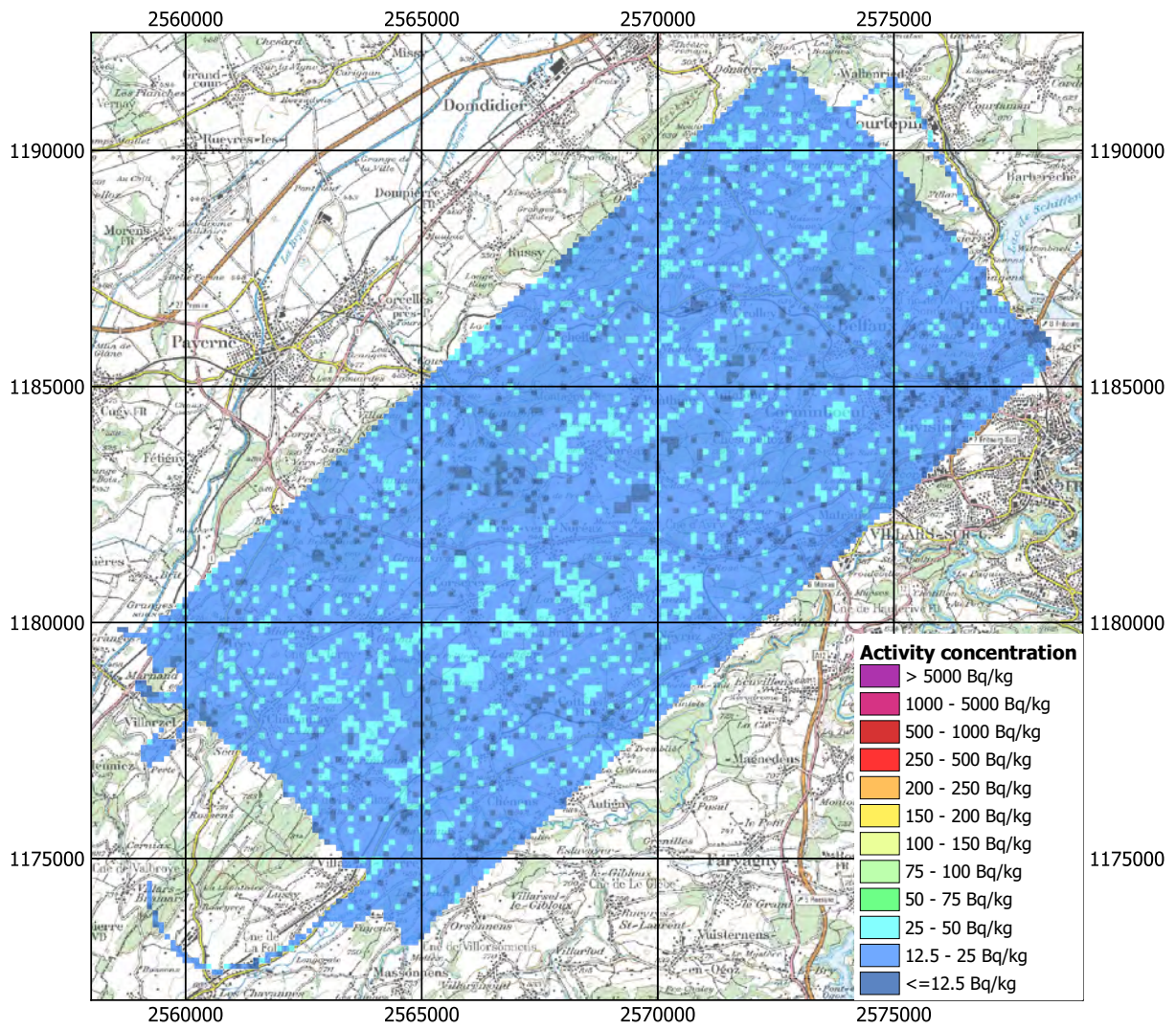


Figure 61:  $^{232}\text{Th}$  activity concentration near Noréaz. Geodaten©swisstopo.

### 2.3.8 Rapperswil

Rapperswil is located in the Canton of St. Gallen north of the Obersee, a part of Lake Zurich. As observed at the measuring areas at other Swiss lakes (Sections 2.3.1, 2.3.3 and 2.3.6), the attenuation of terrestrial photons by the water of the lake can be clearly seen in the maps of the dose rate (Figure 62) and the activity concentration of the natural radionuclide  $^{232}\text{Th}$  (Figure 64). Again, some artefacts over the water due to the low count rate of high energy photons emitted by natural terrestrial radionuclides can be observed in the map of the MMGC-ratio (Figure 63).

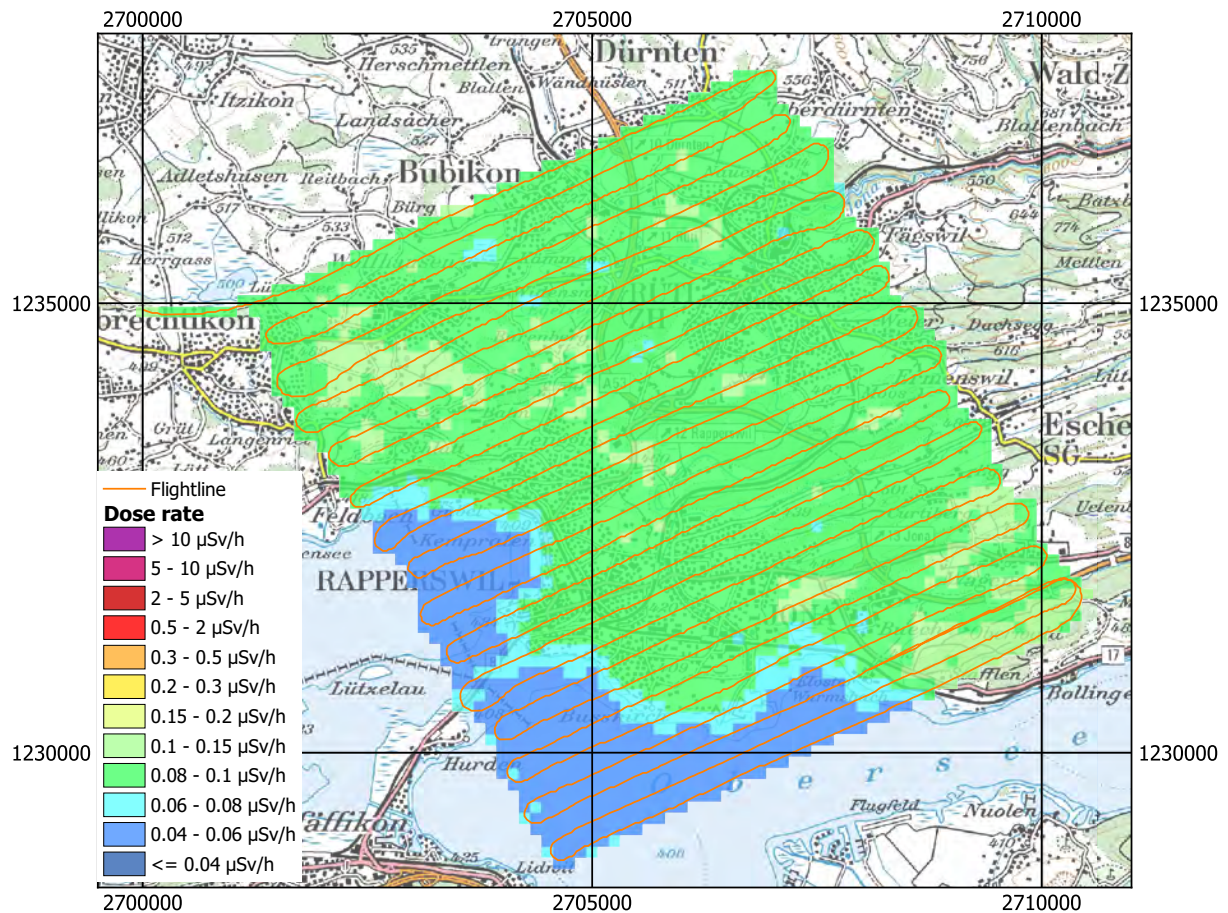


Figure 62: Dose rate near Rapperswil. Geodaten©swisstopo.

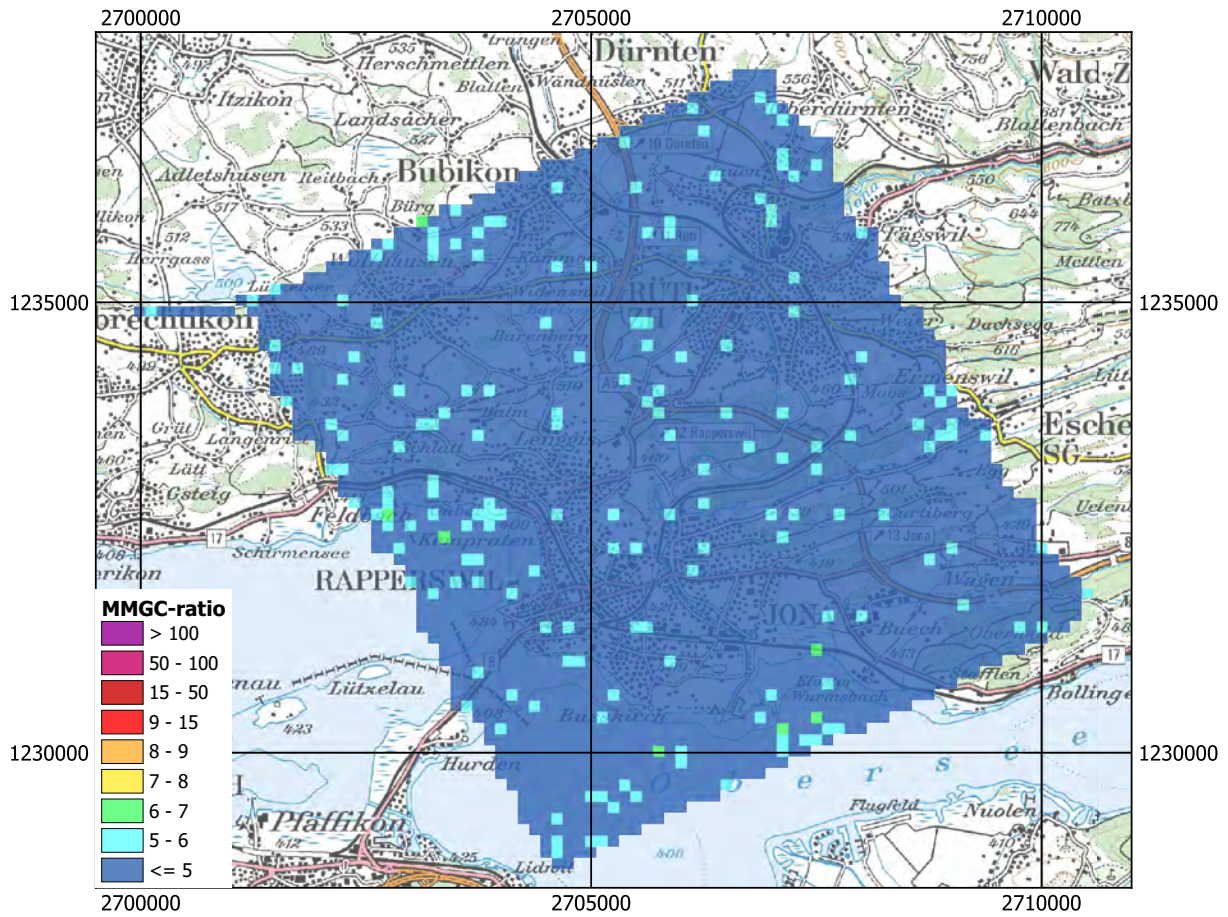


Figure 63: MMGC-ratio near Rapperswil. Geodaten©swisstopo.



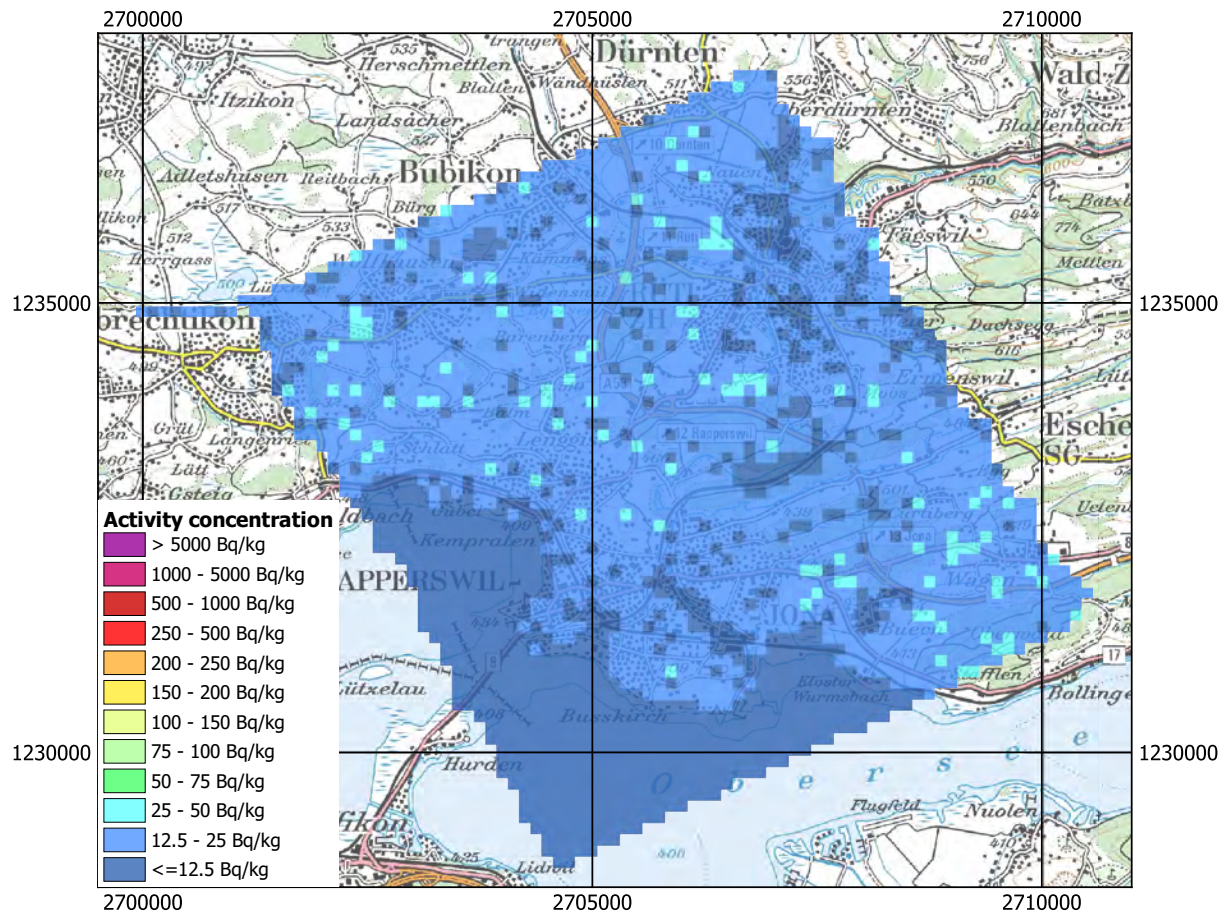


Figure 64:  $^{232}\text{Th}$  activity concentration near Rapperswil. Geodaten©swisstopo.

### 3 Conclusions

An altitude profile over Lake Constance confirmed the already observed influence of airborne radon progeny on the determination of cosmic and background correction.

Search exercises for radionuclide sources were performed in both parts of ARM23. The operational software of the RLL systems was able to detect the sources placed in military training areas. The Man-Made Gross-Count (MMGC) ratio demonstrated a good sensitivity for the identification of radionuclide sources. Nevertheless, a weak radionuclide source placed in the field of view of the helicopter (300 m x 300 m at a ground clearance of 100 m) together with a much stronger radionuclide source emitting higher energy photons was not detected due to Compton scattered photons. Measurements of two teams using drones equipped with radiation monitors demonstrated impressively that the low flying drones (ground clearance below 10 m) can be a valuable tool to identify sources and to further reduce the target area to be searched with ground teams.

Measurements performed on behalf of ENSI over some of the Swiss nuclear power plants, highlighted no deviation from the expected situation. At the site of the nuclear power plant Gösgen (KKG) with its pressurized water reactor, the activation products of the primary coolant loop are kept in the well shielded reactor building. Thus, no elevated readings in the vicinity of the power plant were observed. During the decommissioning of nuclear power plant Mühleberg (KKM) activated components are stored and processed on the plant premises. The dose rate produced by these components is limited and closely monitored by the Swiss Nuclear Safety Inspectorate (ENSI). Despite low, these dose rates from man-made radionuclides are easily detected and identified by the Swiss airborne gamma spectrometry system.

Background flights were performed over several Swiss regions. Besides attenuation effects of water bodies, variations of natural radionuclide content could be observed. A new flight strategy in alpine topography was tested near the Swiss mountain Chrüz. Following contour lines of the topography reduces the necessity for drastic flight altitude changes compared to the parallel line pattern normally used, but is much more challenging the pilots.

### 4 Literature

Bucher, B.: Methodische Weiterentwicklungen in der Aeroradiometrie. Dissertation Nr. 13973, ETH Zürich, 2001.

Schwarz, G. F.: Methodische Entwicklungen zur Aerogammaspektrometrie. Beiträge zur Geologie der Schweiz, Geophysik Nr. 23, Schweizerische Geophysikalische Kommission, 1991.

## 5 Previous reports

Schwarz, G. F., Klingel , E. E., Rybach, L.: Aeroradiometrische Messungen in der Umgebung der schweizerischen Kernanlagen. Bericht f r das Jahr 1989 zuhanden der Hauptabteilung f r die Sicherheit der Kernanlagen (HSK). Interner Bericht, Institut f r Geophysik, ETH Z rich, 1990.

Schwarz, G. F., Klingel , E. E., Rybach, L.: Aeroradiometrische Messungen in der Umgebung der schweizerischen Kernanlagen. Bericht f r das Jahr 1990 zuhanden der Hauptabteilung f r die Sicherheit der Kernanlagen (HSK). Interner Bericht, Institut f r Geophysik, ETH Z rich, 1991.

Schwarz, G. F., Klingel , E. E., Rybach, L.: Aeroradiometrische Messungen in der Umgebung der schweizerischen Kernanlagen. Bericht f r das Jahr 1991 zuhanden der Hauptabteilung f r die Sicherheit der Kernanlagen (HSK). Interner Bericht, Institut f r Geophysik, ETH Z rich, 1992.

Schwarz, G. F., Klingel , E. E., Rybach, L.: Aeroradiometrische Messungen in der Umgebung der schweizerischen Kernanlagen. Bericht f r das Jahr 1992 zuhanden der Hauptabteilung f r die Sicherheit der Kernanlagen (HSK). Interner Bericht, Institut f r Geophysik, ETH Z rich, 1993.

Schwarz, G. F., Klingel , E. E., Rybach, L.: Aeroradiometrische Messungen in der Umgebung der schweizerischen Kernanlagen. Bericht f r das Jahr 1993 zuhanden der Hauptabteilung f r die Sicherheit der Kernanlagen (HSK). Interner Bericht, Institut f r Geophysik, ETH Z rich, 1994.

Schwarz, G. F., Rybach, L.: Aeroradiometrische Messungen im Rahmen der  bung ARM94. Bericht f r das Jahr 1994 zuhanden der Fachgruppe Aeroradiometrie (FAR). Interner Bericht, Institut f r Geophysik, ETH Z rich, 1995.

Schwarz, G. F., Rybach, L.: Aeroradiometrische Messungen im Rahmen der  bung ARM95. Bericht f r das Jahr 1995 zuhanden der Fachgruppe Aeroradiometrie (FAR). Interner Bericht, Institut f r Geophysik, ETH Z rich, 1996.

Schwarz, G. F., Rybach, L., B rlocher, C.: Aeroradiometrische Messungen im Rahmen der  bung ARM96. Bericht f r das Jahr 1996 zuhanden der Fachgruppe Aeroradiometrie (FAR). Interner Bericht, Institut f r Geophysik, ETH Z rich, 1997.

Bucher, B., Rybach, L., Schwarz, G., B rlocher, C.: Aeroradiometrische Messungen im Rahmen der  bung ARM97. Bericht f r das Jahr 1997 zuhanden der Fachgruppe Aeroradiometrie (FAR). Interner Bericht, Institut f r Geophysik, ETH Z rich, 1998.

Bucher, B., Rybach, L., Schwarz, G., B rlocher, C.: Aeroradiometrische Messungen im Rahmen der  bung ARM98. Bericht f r das Jahr 1998 zuhanden der Fachgruppe Aeroradiometrie (FAR). Interner Bericht, Institut f r Geophysik, ETH Z rich, 1999.

Bucher, B., Rybach, L., Schwarz, G., B rlocher, C.: Aeroradiometrische Messungen im Rahmen der  bung ARM99. Bericht f r das Jahr 1999 zuhanden der Fachgruppe Aeroradiometrie (FAR). Interner Bericht, Institut f r Geophysik, ETH Z rich, 2000.

Bucher, B., Rybach, L., Schwarz, G., B rlocher, C.: Aeroradiometrische Messungen im Rahmen der  bung ARM00. Bericht f r das Jahr 2000 zuhanden der Fachgruppe Aeroradiometrie (FAR). Interner Bericht, Institut f r Geophysik, ETH Z rich, 2001.

Bucher, B., Rybach, L., Schwarz, G., Bärlocher, C.: Aeroradiometrische Messungen im Rahmen der Übung ARM01. Bericht für das Jahr 2001 zuhanden der Fachgruppe Aeroradiometrie (FAR). Interner Bericht, Paul Scherrer Institut, Villigen, Schweiz, 2002.

Bucher, B., Rybach, L., Schwarz, G., Bärlocher, C.: Aeroradiometrische Messungen im Rahmen der Übung ARM02. Bericht für das Jahr 2002 zuhanden der Fachgruppe Aeroradiometrie (FAR). Interner Bericht, Paul Scherrer Institut, Villigen, Schweiz, 2003.

Bucher, B., Rybach, L., Schwarz, G.: Aeroradiometrische Messungen im Rahmen der Übung ARM03. PSI-Bericht 04-14, ISSN 1019-0643, Paul Scherrer Institut, Villigen, Schweiz, 2004.

Bucher, B., Butterweck, G., Rybach, L., Schwarz, G.: Aeroradiometrische Messungen im Rahmen der Übung ARM04. PSI-Bericht 05-10, ISSN 1019-0643, Paul Scherrer Institut, Villigen, Schweiz, 2005.

DOI <https://doi.org/10.55402/psi:41689>

Bucher, B., Butterweck, G., Rybach, L., Schwarz, G.: Aeroradiometrische Messungen im Rahmen der Übung ARM05. PSI-Bericht 06-06, ISSN 1019-0643, Paul Scherrer Institut, Villigen, Schweiz, 2006.

DOI <https://doi.org/10.55402/psi:41685>

Bucher, B., Butterweck, G., Rybach, L., Schwarz, G.: Aeroradiometrische Messungen im Rahmen der Übung ARM06. PSI-Bericht 07-02, ISSN 1019-0643, Paul Scherrer Institut, Villigen, Schweiz, 2007.

DOI <https://doi.org/10.55402/psi:41681>

Bucher, B., Guillot, L., Strobl, C., Butterweck, G., Gutierrez, S., Thomas, M., Hohmann, C., Krol, I., Rybach, L., Schwarz, G.: International Intercomparison Exercise of Airborne Gamma-spectrometric Systems of Germany, France and Switzerland in the Framework of the Swiss Exercise ARM07. PSI-Bericht Nr. 09-07, ISSN 1019-0643, Paul Scherrer Institut, Villigen, Schweiz, 2009.

DOI <https://doi.org/10.55402/psi:35550>

Bucher, B., Butterweck, G., Rybach, L., Schwarz, G.: Aeroradiometrische Messungen im Rahmen der Übung ARM08. PSI-Bericht Nr. 09-02, ISSN 1019-0643, Paul Scherrer Institut, Villigen, Schweiz, 2009.

DOI <https://doi.org/10.55402/psi:35550>

Bucher, B., Butterweck, G., Rybach, L., Schwarz, G., Strobl, C.: Aeroradiometrische Messungen im Rahmen der Übung ARM09. PSI-Bericht Nr. 10-01, ISSN 1019-0643, Paul Scherrer Institut, Villigen, Schweiz, 2010.

DOI <https://doi.org/10.55402/psi:35541>

Bucher, B., Butterweck, G., Rybach, L., Schwarz, G., Mayer, S.: Aeroradiometrische Messungen im Rahmen der Übung ARM10. PSI-Bericht Nr. 11-02, ISSN 1019-0643, Paul Scherrer Institut, Villigen, Schweiz, 2011.

DOI <https://doi.org/10.55402/psi:35201>

Bucher, B., Butterweck, G., Rybach, L., Schwarz, G., Mayer, S.: Aeroradiometric Measurements in the Framework of the Swiss Exercise ARM11. PSI-Report No. 12-04, ISSN 1019-0643, Paul Scherrer Institut, Villigen, Switzerland, 2012.

DOI <https://doi.org/10.55402/psi:35137>

Butterweck, G., Bucher, B., Rybach, L., Schwarz, G., Hödlmoser, H., Mayer, S., Danzi, C. Scharding, G.: Aeroradiometric Measurements in the Framework of the Swiss Exercise ARM12. PSI-Report No. 13-01, ISSN 1019-0643, Paul Scherrer Institut, Villigen, Switzerland, 2013.

DOI <https://doi.org/10.55402/psi:35134>

Butterweck, G., Bucher, B., Rybach, L., Schwarz, G., Hohmann, E., Mayer, S., Danzi, C. Scharding, G.: Aeroradiometric Measurements in the Framework of the Swiss Exercise ARM13. PSI-Report No. 15-01, ISSN 1019-0643, Paul Scherrer Institut, Villigen, Switzerland, 2015.

DOI <https://doi.org/10.55402/psi:35064>

Butterweck, G., Bucher, B., Rybach, L., Schwarz, G., Hohmann, E., Mayer, S., Danzi, C. Scharding, G.: Aeroradiometric Measurements in the Framework of the Swiss Exercises ARM14 and FTX14. PSI-Report No. 15-02, ISSN 1019-0643, Paul Scherrer Institut, Villigen, Switzerland, 2015.

DOI <https://doi.org/10.55402/psi:35062>

Butterweck, G., Bucher, B., Rybach, L., Schwarz, G., Hofstetter-Boillat, B., Hohmann, E., Mayer, S., Danzi, C. Scharding, G.: Aeroradiometric Measurements in the Framework of the Swiss Exercises ARM15, GNU15 and the International Exercise AGC15. PSI-Report No. 15-04, ISSN 1019-0643, Paul Scherrer Institut, Villigen, Switzerland, 2015.

DOI <https://doi.org/10.55402/psi:35047>

Butterweck, G., Bucher, B., Rybach, L., Poretti, C., Maillard, S., Schwarz, G., Hofstetter-Boillat, B., Hohmann, E., Mayer, S., Scharding, G.: Aeroradiometric Measurements in the Framework of the Swiss Exercises ARM16 and LAURA. PSI-Report No. 17-01, ISSN 1019-0643, Paul Scherrer Institut, Villigen, Switzerland, 2017.

DOI <https://doi.org/10.55402/psi:34988>

Butterweck, G., Bucher, B., Gryc, L., Debayle, C., Strobl, C., Maillard, S., Thomas, M., Helbig, A., Krol, I., Chuzel, S., Couvez, C., Ohera, M., Rybach, L., Poretti, C., Hofstetter-Boillat, B., Mayer, S., Scharding, G.: International Intercomparison Exercise of Airborne Gamma-Spectrometric Systems of the Czech Republic, France, Germany and Switzerland in the Framework of the Swiss Exercise ARM17. PSI-Report No. 18-04, ISSN 1019-0643, Paul Scherrer Institut, Villigen, Switzerland, 2018.

DOI <https://doi.org/10.55402/psi:34959>,

Butterweck, G., Bucher, B., Rybach, L., Poretti, C., Maillard, S., Schindler, M., Hofstetter-Boillat, B., Mayer, S., Scharding, G.: Aeroradiometric Measurements in the Framework of the Swiss Exercises ARM18 and the International Exercise CONTEX 2018. PSI-Report No. 19-01, ISSN 1019-0643, Paul Scherrer Institut, Villigen, Switzerland, 2019.

DOI <https://doi.org/10.55402/psi:34957>,

Butterweck, G., Bucher, B., Rybach, L., Poretti, C., Maillard, S., Schindler, M., Hofstetter-Boillat, B., Mayer, S., Scharding, G.: Aeroradiometric Measurements in the Framework of the Swiss Exercise ARM19. PSI-Report No. 20-01, ISSN 1019-0643, Paul Scherrer Institut, Villigen, Switzerland, 2020.

DOI <https://doi.org/10.55402/psi:44919>

Butterweck, G., Bucher, B., Breitenmoser, D., Rybach, L., Poretti, C., Maillard, S., Kasprzak, M., Ferreri, G., Gurtner, A., Astner, M., Hauenstein, F., Straub, M., Bucher, M., Harm, C., Scharding, G., Mayer, S.: Aeroradiometric Measurements in the Framework of the Swiss Exercise ARM20. PSI-Report No. 21-01, ISSN 1019-0643, Paul Scherrer Institut, Villigen, Switzerland, 2021.

DOI <https://doi.org/10.13140/RG.2.2.15326.51526>

Butterweck, G., Bucher, B., Breitenmoser, D., Rybach, L., Poretti, C., Maillard, S., Hess, A., Kasprzak, M., Scharding, G., Mayer, S.: Aeroradiometric Measurements in the Framework of the Swiss Exercise ARM21. PSI-Report No. 22-02, ISSN 1019-0643, Paul Scherrer Institut, Villigen, Switzerland, 2022.

DOI <https://doi.org/10.55402/psi:44921>

Butterweck, G., Stabilini, A., Bucher, B., Breitenmoser, D., Rybach, L., Poretti, C., Maillard, S., Hess, A., Kasprzak, M., Scharding, G., Mayer, S.: Aeroradiometric Measurements in the Framework of the Swiss Exercise ARM22. PSI-Report No. 23-01, ISSN 1019-0643, Paul Scherrer Institut, Villigen, Switzerland, 2023.

DOI <https://doi.org/10.55402/psi:51194>

The reports since 1989 can be found and downloaded from the FAR website <https://far.ensi.ch>. under Publications; the reports 1989 - 2006 only in German.

## 6 Evaluation parameters

The parameters used for data evaluation are stored in the header section of each generated ERS 2.0 file. The header section used in the current exercise are listed below.

### 6.1 Detector RLL001

These evaluation parameters were used for the evaluation of exercise ARM23 measured with detector RLL001.

```
V 2.0
HSW AGS_CH_V0.0
/* Parameters used for data evaluation-----
/* No data value;MND -999
/* Energy calibration;ISE0 0;ISE1 3;ISE2 0
/* Energy windows-----
ISW Total;ISWE1_Total 401;ISWE2_Total 2997;ISWB_Total 124.1;ISWC_Total 5.78;ISWT_Total 0.006;ISWRA_Total 0;ISWRB_Total 0
ISW K-40;ISWE1_K-40 1369;ISWE2_K-40 1558;ISWB_K-40 8.1;ISWC_K-40 0.34;ISWT_K-40 0.008;ISWRA_K-40 0;ISWRB_K-40 0
ISW U-238;ISWE1_U-238 1664;ISWE2_U-238 1853;ISWB_U-238 5.8;ISWC_U-238 0.24;ISWT_U-238 0.0055;ISWRA_U-238 0;ISWRB_U-238 0
ISW Th-232;ISWE1_Th-232 2407;ISWE2_Th-232 2797;ISWB_Th-232 0.3;ISWC_Th-232 0.30;ISWT_Th-232 0.006;ISWRA_Th-232 0;ISWRB_Th-232 0
ISW Cs-137;ISWE1-Cs-137 600;ISWE2-Cs-137 720;ISWB-Cs-137 19.9;ISWC-Cs-137 0.63;ISWT-Cs-137 0.01;ISWRA-Cs-137 0;ISWRB-Cs-137 0
ISW Co-60;ISWE1_Co-60 1100;ISWE2_Co-60 1400;ISWB_Co-60 11.8;ISWC_Co-60 0.71;ISWT_Co-60 0.008;ISWRA_Co-60 0;ISWRB_Co-60 0
ISW MMGC1;ISWE1_MMGC1 400;ISWE2_MMGC1 1400;ISWB_MMGC1 0;ISWC_MMGC1 0;ISWT_MMGC1 0.006;ISWRA_MMGC1 0;ISWRB_MMGC1 0
ISW MMGC2;ISWE1_MMGC2 1400;ISWE2_MMGC2 2997;ISWB_MMGC2 0;ISWC_MMGC2 0;ISWT_MMGC2 0.0065;ISWRA_MMGC2 0;ISWRB_MMGC2 0
ISW LOW;ISWE1_LOW 100;ISWE2_LOW 400;ISWB_LOW 0;ISWC_LOW 0;ISWT_LOW 0.02;ISWRA_LOW 0;ISWRB_LOW 0
ISW MID;ISWE1_MID 720;ISWE2_MID 2997;ISWB_MID 0;ISWC_MID 0;ISWT_MID 0.015;ISWRA_MID 0;ISWRB_MID 0
ISW SDI;ISWE1_SDI 240;ISWE2_SDI 2997;ISWB_SDI 84.6;ISWC_SDI 4.32;ISWT_SDI 0.0053;ISWRA_SDI 0;ISWRB_SDI 0
/* Stripping factors-----
ISWS_U-238_K-40 0.931
ISWS_Th-232_K-40 0.478
ISWS_Co-60_K-40 0.067
ISWS_Th-232_U-238 0.362
ISWS_U-238_Th-232 0.049
ISWS_K-40-Cs-137 0.450
```

```

ISWS_U-238_Cs-137 3.161
ISWS_Th-232_Cs-137 1.654
ISWS_Co-60_Cs-137 0.154
ISWS_K-40_Co-60 0.758
ISWS_U-238_Co-60 2.370
ISWS_Th-232_Co-60 0.684
/* Conversion factors-----
ISWA_AW_K-40 5.58
ISWA_AW_U-238 3.57
ISWA_AW_Th-232 1.22
ISWA_AW_Cs-137 1.02
ISWA_AA_Cs-137 201
ISWA_AP_Cs-137 2511000
ISWA_AP_Co-60 1505000
ISD_SDI 5.65E-08
ISWD_K-40 0.000289
ISWD_U-238 0.00197
ISWD_Th-232 0.000971
ISWD_Cs-137 0.000191
/*
/* Corrections-----
/* Definition of additional Identifiers for corrected altitude and ground clearance,
/* an indicator for a new flight and the factor for calculation of synthetic cosmic counts
/* Corrected altitude im m;DEFINE&PZ_korr
/* Corrected ground clearance in m; DEFINE&PH_korr
/* Switch for data composed of several flights;DEFINE&New_Flight
/* Factor for calculation of synthetic cosmic counts;DEFINE&Factor_COS
/* Factor for the calculation of synthetic cosmic counts;&Factor_COS 14.35
/* Topographic correction;MTC Y
/* Radon correction;MRC N

```



Paul Scherrer Institut :: Forschungsstrasse 111 :: 5232 Villigen PSI :: Switzerland :: Tel. +41 56 310 21 11 :: [www.psi.ch](http://www.psi.ch)

